NUMERICAL SIMULATIONS OF WINGS IN UNSTEADY FLOWS

by

Reza Karkehabadi

Dissertation submitted to the faculty of the

Virginia Polytechnic Institute and State University

in partial fulfillment of the requirements for the degree of

DOCTOR OF PHILOSOPHY

in

Engineering Mechanics

APPROVED:

Prof. D. T. Mook, Chairman

Prof. W. C. Durham

Prof. S. L. Hendricks

Prof. A. H. Nayfeh

Prof. C. W. Smith

Prof. D. P. Telionis

June, 1995

Blacksburg, Virginia

NUMERICAL SIMULATIONS OF WINGS IN UNSTEADY FLOWS

by

Reza Karkehabadi

Committee Chairman: Prof. D. T. Mook

Engineering Science and Mechanics

(ABSTRACT)

The unsteady vortex-lattice method is used to calculate the pressure coefficients on thick and thin airfoils in steady and unsteady flowfields. The parameters which affect the results, such as time step and aspect ratio, are studied. The effects of Reynolds number and thickness of a wing in steady state and in oscillation are investigated. The present computed results for thick and thin wings are in close agreement with the experimental data. The numerical results obtained from a lifting-surface approximation are also in close agreement with the experimental data for a wing as thick as 18%. The lift and moment coefficients are affected by the thickness of a wing in oscillation and this effect is more noticeable for the moment coefficient. But to illustrate this it is necessary to go as high as 27% thickness.

A wing in steady flight near a wavy surface, such as in the case of a large transoceanic wingship, is simulated by a wing oscillating in heave near a flat surface. In accord with the wingship, small aspect ratios and slight camber are considered. The numerical simulation predicts that the mean aerodynamic loads on a wing executing a simple-harmonic heaving motion are higher than the corresponding loads on the same wing in steady flight at the mean height and the same angle of attack. The increases are about the same for all heights. Hence, these preliminary results suggest that it would be beneficial to fly near the waves; that doing so would improve the aerodynamic efficiency. Also included in the present results are numerical simulation of the wakes that show the strong influences of the ground and the oscillations on their behavior.

The unsteady vortex-lattice method is further used to investigate the effect of trailing vortices from a large leading wing on a trailing aircraft. The aerodynamic response of the trailing aircraft is examined by calculating the lift and drag forces and the pitch and roll

moments. Furthermore, the aerodynamic response and the behavior of the wakes of the crossing wings are investigated.

ACKNOWLEDGEMENTS

I would like to express my gratitude and appreciation to my mentor, Dr Dean T. Mook, for his advice and guidance throughout this work. Despite his many activities, he always managed to find time for my questions. I would also like to thank Dr. Nayfeh and Dr. Telionis for their valuable suggestions. I am indebted to Dr. Nayfeh, Dr. Hendricks, Dr. Smith, Dr. Durham, and Dr. Telionis for spending their valuable time in reading this manuscript. I am also grateful to Sally Shrader for her many clerical services. I am thankful to Duane Taylor's valuable assistance in the E.S.M computer lab. My appreciation is also expressed to the E.S.M department for their financial support.

To all my friends at Virginia Tech, especially Mike Smith, Frederick Just, and Yannick Fierling, thank you for your support, encouragement, and love.

My sincere appreciation and love to my family; to my brother, Masoud and Saeid, for their help and companionship; to my sister, Tahereh, for her moral support; to my father, Hossein, for always being a role model in my life; to my mother Ozra, for her love and moral support; and to my children Hossein and Ozra, for their patience and love. My deepest gratitude is expressed to the one who has given me unconditional support, my wife Sharon, for her love, encouragement and understanding through the years.

Contents

1 INTRODUCTION **1**

1.1 Motivation for the Present Work 1

1.1.1 Oscillating Wing In and Out of Ground Effect 2

1.1.2 The Effect of Reynolds Number and Thickness 2

1.1.3 Trailing Vortex Effects on Following Aircraft 3

1.2 Review of Literature 3

1.3 Objective 7

2 THE AERODYNAMIC MODEL **8**

2.1 Introduction 8

2.2 The Unsteady Vortex-Lattice Method 9

2.2.1 Constructing The Numerical Solution: Conditions to be Satisfied . . 10

2.2.2 Aerodynamic Load for Thick Bodies 11

2.3 Two-Dimensional Panel Method 14

2.4 Numerical Results and Comparisons 15

2.5 Conclusion 19

3 WING IN HEAVING OSCILLATORY MOTION **37**

3.1 Introduction 37

3.2 Description of the Simulation 38

3.3 The Mean Aerodynamic Load 38

3.4 Results 39
3.4.1 Oscillation With High Frequency 40
3.4.2 Oscillation With Low Frequency 40
3.4.3 The Effect of The Reduced Frequency 41
3.4.4 Calculated Wake 42
3.5 Conclusion 44

4 THICK-WING IN STEADY AND UNSTEADY FLOWFIELD 64
4.1 Introduction 64
4.2 Description of The Problem 65
4.3 Results 65
4.3.1 Effect of Reynolds Number 65
4.3.2 Thickness Effect 66
4.4 Conclusion 67

5 TRAILING VORTICES AND THEIR EFFECTS 77
5.1 Introduction 77
5.2 Description of The Problem 78
5.3 Numerical Results 79
5.4 Conclusion 84

6 CONCLUSION 113
6.1 Conclusion 113

List of Figures

2.1 Comparison of numerically predicted normal force and moment coefficients as functions of angle of attack with the experimental data. 20

2.2 Computed wakes for a rectangular wing of unit aspect ratio with 20 degrees angle of attack. 21

2.3 Comparison of numerically predicted lift, drag, and moment coefficients with the experimental data for a wing of F104-A type. 22

2.4 Comparison of numerically predicted lift, drag, and moment coefficients with experimental data for an F104-A in ground effect. The height above the ground is 0.28 span and is measured 3.3 inches behind the apex. 23

2.5 Comparison of numerically-calculated velocity as a function of position with the exact solution for a sphere of unit radius. 24

2.6 Comparison of numerically calculated velocity in the mid-span of a cylinder, L/D=5.5, with the exact solution of flow over a circle in a uniform-stream parallel to the x-axis. (a) open ends cylinder and (b) closed ends cylinder. . 25

2.7 Comparison of numerically calculated velocity in the mid-span of a cylinder with the exact solution of flow over a circle (a) L/D=11, (b) L/D=22, and (c) L/D=33. 26

2.8 Comparison of numerically predicted velocity with the experiment for a cone-cylinder with zero angle of attack. 27

2.9 Exact steady-state solution for flow over a Karman-Trefftz airfoil with 8 degrees angle of attack. 28

2.10 Pressure coefficient as a function of position using 2-D unsteady panel method, 72 elements, 8 degrees angle of attack, .000055 time step. The wing has traveled (a) .1 Chord and (b) .5 Chord. 29

2.11 The pressure coefficient as a function of position using the 2-D unsteady panel method, 50 elements, 8 degrees angle of attack, .00055 time step. The wing has traveled (a) .1 chord, (b) .5 chord, (c) 1 chord, and (d) 4 chords. . 30

2.12 Computed wakes for a Karman-Trefftz airfoil with 8 degrees angle of attack, after the wing has traveled .5 chord. 31

2.13 Computed wakes for a Karman-Trefftz airfoil with 8 degrees angle of attack, after the wing has traveled 4 chords. 32

2.14 Calculated pressure distributions for flow over a 3-D Karman-Trefftz airfoil, 8 degrees angle of attack. The wing has traveled one chord and the aspect ratio is 11.1. The unsteady vortex lattice method is used. 33

2.15 Calculated pressure distributions for flow over a Karman-Trefftz airfoil, 8 degrees angle of attack. 34

2.16 Computed wakes for a 3-D Karman-Trefftz airfoil with 8 degrees angle of attack. The aspect ratio is 5.5. 35

2.17 Computed wakes for a Karman-Trefftz airfoil with 8 degrees angle of attack. The aspect ratio is 5.5 and the wing has traveled 1 chord. 36

3.1 Lift and moment coefficients as functions of angle of attack for the NACA 0012 airfoil, $\alpha = 3° + 10° \sin \omega t$, and $k = \omega C/2V_\infty$=0.1. The moment is taken about quarter chord from the leading edge. 45

3.2 Lift, drag, moment, and vertical position of the wing with respect to the mean height above the ground as functions of the distance traveled, d, in terms of chords, C. The moment is taken about the quarter chord from the leading edge, and k=$\pi/2$. — in ground, - - out of ground 46

3.3 Lift, drag, moment, and vertical position of the wing with respect to the mean height above the ground as functions of the distance traveled, d, in terms of chords, C. The moment is taken about the quarter chord from the leading edge, and k=$\pi/16$. — in ground, - - out of ground 47

3.4 Lift, drag, moment, and vertical position of the wing with respect to the mean height above the ground as functions of the distance traveled, d, in terms of chords, C. The moment is taken about the quarter chord from the leading edge, and k=$\pi/32$. — in ground, - - out of ground 48

3.5 Lift, drag, moment, and vertical position of the wing with respect to the mean height above the ground as functions of the distance traveled, d, in terms of chords, C. The moment is taken about the quarter chord from the leading edge, and k=$\pi/64$. — in ground, - - out of ground 49

3.6 Lift, drag, moment, and vertical position of the wing with respect to the mean height above the ground as functions of the distance traveled in chords for a heaving wing in ground effect at three different frequencies. The angle of attack is 3 degrees. — k=$\pi/2$, - - k=$\pi/4$, -.- $k = \pi/8$ 50

3.7 Lift, drag, moment, and vertical position of the wing with respect to the mean height above the ground as functions of the distance traveled in chords for a heaving wing in ground effect at three different frequencies. The angle of attack is 3 degrees. — k=$\pi/16$, - - k=$\pi/32$, -.- $k = \pi/64$ 51

3.8 Lift, drag, moment, and vertical position of the wing with respect to the mean height above the ground as functions of the distance traveled in chords for a heaving wing out of ground effect at three different frequencies. The angle of attack is 3 degrees. — k=$\pi/2$, - - k=$\pi/4$, -.- $k = \pi/8$ 52

3.9 Lift, drag, moment, and vertical position of the wing with respect to the mean height above the ground as functions of the distance traveled in chords for a heaving wing out of ground effect at three different frequencies. The angle of attack is 3 degrees. — k=$\pi/16$, - - k=$\pi/32$, -.- $k = \pi/64$ 53

3.10 Comparison of mean values of lift, drag, and moment coefficients for different periods of oscillation with the steady-state result in ground effect. The mean angle of attack is 3 degrees and h=0.5 chord. 54

3.11 Comparison of mean values of lift, drag, and moment coefficients for different periods of oscillation with the steady-state result out of ground effect. The mean angle of attack is 3 degrees. 55

3.12 Comparison of the unsteady lift, drag, and moment coefficients with the steady-state result. The angle of attack is 3 degrees. 56

3.13 Comparison of the unsteady lift, drag, and moment coefficients with the steady-state result. the angle of attack is 3 degrees. 57

3.14 Computed wakes for the wing in ground effect where k=$\pi/2$, amplitude=0.25 chord. The dots represent the location of vorticity in the wake of the wing. The portion of the wake generated during the initial start up can be seen at the far right. 58

3.15 Computed wakes for the wing out of ground effect where k=$\pi/2$, amplitude=0.25 chord. The dots represent the location of vorticity in the wake of the wing. The portion of the wake generated during the initial start up can be seen at the far right. 59

3.16 Computed wakes for the wing in ground effect where k=$\pi/4$, amplitude=0.25 chord. The dots represent the location of vorticity in the wake of the wing. The portion of the wake generated during the initial start up can be seen at the far right. 60

3.17 Computed wakes for the wing out of ground effect where k=$\pi/4$, amplitude=0.25 chord. The dots represent the location of vorticity in the wake of the wing. The portion of the wake generated during the initial start up can be seen at the far right. 61

3.18 Computed wakes for the wing in ground effect k=$\pi/16$, amplitude=0.25 chord. The dots represent the location of vorticity in the wake of the wing. The portion of the wake generated during the initial start up can be seen at the far right. 62

3.19 Computed wakes for the wing out of ground effect k=$\pi/16$, amplitude=0.25 chord. The dots represent the location of vorticity in the wake of the wing. The portion of the wake generated during the initial start up can be seen at the far right. 63

4.1 Experimental and numerical lift and moment as functions of the angle of attack for the NACA 0009 airfoil. 68

4.2 Experimental and numerical lift and moment as functions of the angle of attack for the NACA 0009 airfoil. 69

4.3 Experimental and numerical lift and moment as functions of the angle of attack for the NACA 4409 airfoil. 70

4.4 Experimental and numerical lift and moment as functions of the angle of attack for the NACA 4409 airfoil. 71

4.5 Experimental and numerical lift and moment as functions of the angle of attack for symmetric NACA 00xx airfoil of different thicknesses. 72

4.6 Experimental and numerical lift and moment as functions of the angle of attack for symmetric NACA 44xx airfoil of different thicknesses. 73

4.7 Lift and moment as functions of the angle of attack for uncambered airfoils of different thicknesses. 74

4.8 Lift and moment as functions of the angle of attack for cambered airfoils of different thicknesses. 75

4.9 Calculated lift and moment coefficients as functions of the angle of attack for wings of different thicknesses, $\alpha = 3° + 10° \sin \omega t$, and k=.1. The moment is taken about quarter chord from the leading edge. 76

5.1 Calculated lift, drag, and moment coefficients as functions of the angle of attack for the wing of a Boeing 757. 85

5.2 Computed wake for the wing of the Boeing 757 with 7 degrees angle of attack. 86

5.3 Calculated lift, drag, and moment coefficients as functions of the angle of attack for the wing of the Cessna 750 Citation X. 87

5.4 Computed wake for the wing of the Cessna 750 citation X with 5 degrees angle of attack. 88

5.5 Lift, drag, and moment coefficients for the Cessna flying with 5 degrees angle of attack. 89

5.6 The calculated wake of the 757, the wing of the Cessna wing, and its calculated wake, where Y/C=0 and Z/C=0 90

5.7 The calculated wake of the 757, the wing of the Cessna, and its wake, where Y/C=0 and Z/C=-1.5. 91

5.8 The calculated wake of the 757, the wing of the Cessna, and its wake, where Y/C=0 and Z/C=1.5. 92

5.9 Lift, drag, roll, and pitch coefficients for the Cessna flying with 5 degrees angle of attack. 93

5.10 The calculated wake of the 757, the wing of the Cessna, and its calculated wake, where Y/C=-4 and Z/C=-2. 94

5.11 The wing of the Cessna and the velocity vectors in the Trefftz plane located four chord lengths behind the wing of the Cessna, where Y/C=-5 and Z/C=-2 95

5.12 Lift, drag, roll, and pitch coefficients for the Cessna flying with 5 degrees angle of attack. 96
5.13 The calculated wake of the 757, the wing of the Cessna, and its calculated wake, where Y/C=-4 and Z/C=2. 97
5.14 Lift, drag, roll, and pitch coefficients for the Cessna flying with 5 degrees angle of attack. 98
5.15 The calculated wake of the 757, the wing of the Cessna, and its wake, where Y/C=-3.2 and Z/C=1. 99
5.16 The calculated wake of the 757, the wing of the Cessna, and its wake, where Y/C=-3.2 and Z/C=2. 100
5.17 The wing of the Cessna and the velocity vectors in the Trefftz plane located four chord lengths behind the wing of the Cessna, where Y/C=-3.2 and Z/C=1.101
5.18 The wing of the Cessna and the velocity vectors in the Trefftz plane located four chord lengths behind the wing of the Cessna, where Y/C=-3.2 and Z/C=4.102
5.19 The wing of the Cessna and the velocity vectors in the Trefftz plane located four chord lengths behind the wing of the Cessna, where Y/C=-3.2 and Z/C=10. 103
5.20 Lift, drag, roll, and pitch coefficients for the Cessna flying with 5 degrees angle of attack. 104
5.21 The calculated wake of the 757, the wing of the Cessna, its wake, where Y/C=-3.2 and Z/C=-1. 105
5.22 The calculated wake of the 757, the wing of the Cessna, and its wake, where Y/C=-3.2 and Z/C=-4. 106
5.23 The wing of the Cessna and the velocity vectors in the Trefftz plane located four chord lengths behind the wing of the Cessna, where Y/C=-3.2 and Z/C=-1. 107

5.24 Lift, drag, roll, and pitch coefficient for the Cessna as it passes the wake of the 757. The angle between their paths is 45 degrees. The angle of attack of Cessna is 5 degrees and Z/C is 1.5. 108

5.25 The wings and calculated wakes of the Cessna and the 757, where the angle between their paths is 45 degrees and Z/C is 1.5. The angles of attacks are 5 degrees for the Cessna and 7 degrees for the 757. 109

5.26 The wings and calculated wakes of the Cessna and the 757, where the angle between their paths is 45 degrees and Z/C is 1.5. The angles of attacks are 5 degrees for the Cessna and 7 degrees for the 757. 110

5.27 Computed wake for the 757 in different heights below the Cessna's wing. The Angles of attack are 7 degrees for the 757 and 5 degrees for the Cessna. The vertical distance measured from the 757 to the Cessna (Z/C) from top to bottom are 0, -1.5, -3, -4, and -5. 111

5.28 Computed wake for the 757 in different heights below the Cessna's wing. The Angles of attack are 7 degrees for the 757 and 5 degrees for the Cessna. The vertical distance measured from the 757 to the Cessna (Z/C) from top to bottom are 0, 1.5, 3, 4, and 5. 112

Chapter 1

INTRODUCTION

1.1 Motivation for the Present Work

As testing of aircraft designs becomes more expensive, computational methods continue to become more prominent. An accurate prediction of the aerodynamic load is essential for modeling interactions between structure, flowfields, and control systems. To facilitate use of computational methods by designers, the technique needs to be developed and validated. In the present work, a previously developed method is refined, extended, and applied to the problems of interest.

Recent interest in modeling complete aircraft increases the desire for accurate means of estimating unsteady loads. Also time-dependent, three-dimensional flowfields are generally difficult to compute using the full Navier-Stokes equations, particularly if relative motion between solid bodies is involved. To obtain engineering solutions for these types of flowfields, simpler mathematical models must be used. The use of the unsteady vortex-lattice method is further evaluated here.

For an accurate structural analysis, it is valuable and may even be necessary to predict the pressure on the true geometry. Although the unsteady vortex lattice method (UVLM) has established credibility in predicting the lift and induced-drag forces, the method has

not been carefully studied for calculating the unsteady pressure coefficients on thick-lifting bodies.

1.1.1 Oscillating Wing In and Out of Ground Effect

Because there is a marked increase in the ratio of lift to drag that occurs when a wing flies near the ground, there is an interest in designing airplanes to operate near the ground. Some examples are the wingship proposed by Aerocon, Inc. and the so-called ekranoplans (some as large as a DC-9) designed, built, and flown in the former Soviet Union. An airplane can fly near the surface of the ocean from continent to continent; hence, one application of such craft is transoceanic flight. One of the fundamental questions that has not received much attention to date is how the ocean waves will affect the wing performance. In chapter 3 this question is addressed. A wing in an oscillatory heaving motion in ground-effect could be considered a first approximation to a wing flying low over a wavy surface. The effect of the reduced frequency and the behavior of the wake for a three-dimensional cambered wing oscillating in heave in ground effect is investigated.

The analysis of a wing in oscillation out of ground-effect is valuable also. Not only does it have direct applications, such as in aircraft maneuvers, but it also can be used to evaluate the unsteady ground effect by comparing the results of the analysis with those for the wing oscillating near the ground.

1.1.2 The Effect of Reynolds Number and Thickness

The influence of Reynolds number is also a question of interest. In the present work, the aerodynamic models are infinite-Reynolds-number approximations to the solutions of the complete Navier-Stokes equations. Invariably, aerodynamic models of the flowfield are based on the presumption that the line of separation is known. Thus, they are incapable of predicting stall. However, when the wakes are treated as rotational inviscid flowfields, the aerodynamic models can provide surprisingly accurate simulations of vorticity-dominated flowfields (e.g., see Elzebda et al., 1994).

Often, calculating the aerodynamic load on a wing is not the final goal, but a necessary step in solving the aerodynamic equations simultaneously with the equations of motion. Therefore, the size of the model becomes very important. One can often realize substantial reductions in computational time by using a lifting-surface approximation instead of a thick-wing model. The most important question is, when is such an approximation appropriate? In chapter 4, it is attempted to answer this question.

1.1.3 Trailing Vortex Effects on Following Aircraft

The vortex generated at the edge of the wing of an airplane is called the trailing vortex or the wing-tip vortex. This vortex is generated by the intrusion of the stream around the wing-tip from the high static pressure on the lower surface of the wing into the low static pressure on the upper surface. Trailing vortices are the counter-rotating cylindrical air masses that trail behind the wing-tips of every airplane. Other planes flying too close behind can get caught in the rotating swirl. The trailing vortex not only contributes to a decline in the lift coefficient of the wing, but also can lead to stability problems for smaller following aircraft. If a craft trails this whirling vortex too closely, it can be buffeted brutally. The accident involving the Cessna airplane at the Nagoya airport is one example of the trailing vortex effect (Ogawa, 1993). In chapter 5, the trailing vortex and its effect on a smaller plane is investigated.

1.2 Review of Literature

The vortex-lattice method has been widely used to model steady and unsteady aerodynamics for thin and thick, lifting and non-lifting bodies. Belotserkovskii (1977) obtained the steady normal force and pitch moment for a unit-aspect-ratio rectangular flat plate using the vortex-lattice method. Kandil et al. (1976) and Konstadinopoulos (1985) presented results for the same configuration as well as others. All found good agreement with the results of Belotserkovskii (1965). Belotserkovskii and Nisht (1974) presented a method for treating

swept-back wings in unsteady flows. This method is capable of determining the shape of the wakes emanating from the wing-tips and the trailing-edge, but it does not consider leading-edge separation. This method was extended to a delta wing by Maddox (1973), Mook and Maddox (1974), Kandil et al. (1976), Konstadinopoulos (1985), and Elzebda (1987).

The potential flow around closed nonlifting bodies was calculated by Asfar et al. (1979) using a combination of the vortex-lattice and a source panel method. The bodies which were analyzed include a sphere, an ellipsoid of revolution, an ogive-cylinder, and a cone-cylinder. Their results are in good agreement with experimental data and analytical solutions. Their results showed that the vortex-lattice method yields results that are as good, or better, than those obtained from the various combinations including sources alone.

Kandil (1974) used the vortex-lattice method to calculate the steady-state aerodynamic load on a thick-wing. Atta and Nayfeh (1978) used the unsteady vortex-lattice method to calculate the aerodynamic loads on a wing-body combination. The derivative of the velocity-potential in Bernoulli's equation for the fuselage was set to zero. The derivative of the velocity-potential for the thin-wing was included. Katz and Maskew (1988) used a panel method together with a time-dependent vortex wake to calculate the aerodynamic load on a complete aircraft configuration. The calculation of the velocity-potential term for a thin-wing was explained by Konstadinopoulos et al. (1981); however, the procedure to calculate this term for a thick-body was not explained or discussed. Thick wings in low Reynolds number are used in wells self-rectifying airturbine for wave-energy conversion (Raghunathan 1982, 1983). The performance of a thick symmetrical airfoil at low Reynolds number over a range of incidence was studied experimentally by Raghunathan and Harrison (1988).

In the computation of the velocity from the Biot-Savart law, the field point where the velocity is to be calculated may be close to a vortex segment; consequently, an unreasonably high velocity is generated by that segment. Thus, every vortex-lattice algorithm must contain a provision to ignore the effect of a vortex segment when it is less than a specified

distance from the field point. The critical distance is called the cutoff length and it can affect the results. Elzebda (1987) calculated the cutoff length by trial and error.

The unsteady analysis using the vortex-lattice method was presented by Thrasher et al. (1977) and Atta et al. (1977). The time histories of the normal-force and pitching-moment coefficients for a rectangular wing of a unit-aspect-ratio were presented by Thasher (1979).

Konstadinopoulos et al. (1985) developed a numerical method for simulating one degree of freedom wing rock. Elzebda (1987) expanded the method to include two degrees of freedom wing rock.

Mracek and Mook (1991) used a vortex-panel method to calculate the aerodynamic load on flat rectangular and delta wings. They also used the method to predict wing rock by integrating equations of motion and fluid equations simultaneously. They used controls to suppress wing rock. Luton and Mook (1993) used the vortex-lattice method to predict unsteady aeroelastic behavior by solving the equations of motion for both the structure and the fluid simultaneously.

Steven (1985) studied the landing performance of an aircraft. The flow during take-off and landing is unsteady even if the aircraft is moving with constant velocity. The phenomenon of ground effect is also observed in ship motion near a canal wall or near a second ship. Exact solutions for three-dimensional wings are most likely impossible to obtain (Licher, 1956). Since experimental work is a difficult and expensive task for wings in ground effect (Tuck, 1978), a numerical technique is valuable. In studies of the steady and unsteady ground effect, Nuhait (1989), applied the vortex-lattice method to a tapered wing of F-104A. His normal and drag forces are in good agreement with the experimental data obtained by Chang (1985). However, the pitching moment did not compare well with the experimental data for the wing in and out of ground effect. He used the method of images to enforce the no-penetration condition at the ground. Chen and Schweikhard (1985) investigated the ground effect on a two-dimensional flat plate by using the method of images. They solved the unsteady ground-effect problem for a two-dimensional flat plate. In their work they assumed the wake to be straight along the flight path. They found that the mean

lift due to the unsteady ground effect is greater than that due to the steady ground effect for intermediate heights above the ground. Plotkin (1981) calculated the effect of the thickness on the lift coefficient for an airfoil in ground effect. Simulation of an aircraft during landing and take-off requires the unsteady ground effect. Nuhait and Zedan (1993) investigated the ground effect for a two-dimensional airfoil in unsteady flow using the vortex-lattice method. Chang (1985) and Chang and Muirhead (1985) tested several thin flat delta wings in steady and unsteady ground effects. The wings on high-speed ground vehicles, such as racing cars, are another example of lifting surfaces in unsteady ground effect. Normally the wing used in racing cars has a negative incidence and an oscillatory heaving motion when the roadway is not perfectly smooth. Katz (1985) investigated the performance of automotive lifting surfaces in close proximity to ground. He considered a rectangular, uncambered wing and investigated the aerodynamic load on a wing oscillating in heave, in and out of ground effect. He also investigated the effect of aspect ratio. Ando et al. (1992) used lifting-surface techniques to analyze a thin two-dimensional airfoil flying over a wavy surface.

The behavior of vortex wakes was studied for a two-dimensional airfoil in oscillation out of ground effect by Katz and Weihs (1978), and more recently by Mook and Dong (1994).

Bloy et al. (1990, 1991, 1993) investigated the effect of the tanker downwash and sidewash on the receiver where relatively simple wake models were used. Since more vorticity is shed inboard on a tapered wing, the trailing vortex roll up takes place more slowly compared with a rectangular wing of the same aspect ratio. Bloy et al. (1993) presented the interference between tanker and receiver for a tapered tanker wing. Hoganson (1983) evaluated the longitudinal aerodynamic interference between the KC10 tanker and a B52 receiver. Hoganson did not consider the rolling-up process of the tanker's wing-tip vortices. Bloy and West (1993) presented results for a more realistic roll-up model of the wake. Iversen and Shmuel (1973) used wind-tunnel tests to investigate the change in lift force and rolling moment on an aircraft due to its penetration into the vortex trail of a leading aircraft. The aerodynamic load of the trailing aircraft for various angle of attack and different separation distances between them was investigated experimentally by Olwi and

Ghazi (1992). Richason and Katz (1994) investigated the aerodynamic loads for two wings following closely intersecting paths.

1.3 Objective

As a first step to the problem the general unsteady vortex-lattice method was validated for nonlifting bodies and then extended to lifting bodies with edge separation and was validated by comparing the results with the experimental data. The unsteady vortex-lattice method was also extended to include the ground effect and the results were compared with the experimental data. The method was extended further to calculate the unsteady pressure coefficient on the true geometry. The results were compared with a two-dimensional panel method whose credibility had already been established. The unsteady vortex-lattice method was further extended to calculate the aerodynamic load on an oscillatory wing. Some results were also compared with experimental data.

Extension, refinement, and establishing credibility for the unsteady vortex-lattice method was only a portion of the present work. The second phase of the present study is investigating:

1. The parameters which affect the predicted aerodynamic loads when the unsteady vortex-lattice method is used, such as time step and aspect ratio;
2. The effect of a wing oscillating in heave near a flat surface;
3. The effect of a wing oscillating in heave out of ground effect;
4. The behavior of the wake and the effect of the reduced frequency on a three-dimensional lifting surface oscillating in heave;
5. When a thick wing can be replaced by a lifting surface lying on the camber surface of the actual airfoil;
6. The effect of the Reynolds number on the aerodynamic loads;
7. The effect of trailing vortices from a large leading wing on a trailing aircraft; and
8. The aerodynamic loads of a wing crossing the wake of a larger wing.

Chapter 2

THE AERODYNAMIC MODEL

2.1 Introduction

An accurate prediction of the aerodynamic load is essential for structural and stability analysis of aircraft. Experimental measurements are valuable, but often limited to the final design since they are time-consuming, expensive, and not flexible. The solutions of flow problems by analytical techniques are limited to simple geometries. The application of numerical techniques allows the treatment of more realistic geometries. A method which is based on the surface distribution of singularity elements is preferable, since it requires less computational effort in comparison with the methods that numerically integrate the Euler or the Navier-Stokes equations.

The UVLM is a powerful technique for calculating the unsteady, incompressible, inviscid, three-dimensional flows around arbitrary geometries. In order to apply the UVLM to the problem of interest, the validity of the technique must be shown. It may be necessary to calculate the aerodynamic loads on a wing-body combination or a full configuration aircraft, consisting of lifting and nonlifting bodies. In this chapter the UVLM is applied to thin and thick wings and the results are compared to experimental and/or exact analytical data.

The aerodynamic loads on nonlifting bodies are obtained using the UVLM and compared

with the experimental data. The UVLM is also applied to thick-lifting bodies. The pressure coefficients on the wing are compared with the unsteady panel method. The effects of aspect-ratio and time step are investigated.

2.2 The Unsteady Vortex-Lattice Method

When a wing of arbitrary planform is set in motion, vorticity is generated in a thin region adjoining the surface known as the boundary layer. It follows from the definition of vorticity that vorticity anywhere in the flowfield induces velocity everywhere in the flowfield. This is a kinematical result and valid for viscous as well as inviscid flows. In the actual flow, the vorticity-induced disturbance emanating from the boundary layers interferes with the oncoming stream to the extent that both the no-slip and no-penetration boundary conditions are satisfied on the surface of the wing. In the present aerodynamic model, the boundary layers are simulated by vortex sheets wrapped over the body surfaces. When the wing is thin, the vortex sheets on the upper and lower surfaces are merged into a single surface at the camber line. These infinitesimally thin layers of vorticity may be viewed as the infinite-Reynolds-approximation of the actual boundary layer. Hence, one can expect the present model to improve as the Reynolds number increases. To expedite the calculation of the induced-velocity field, the sheets are represented by lattices of discrete vortex lines. Each line segment in the lattice is relatively short and straight, and its induced velocity is readily calculated from the familiar Biot-Savart law (e.g. see Karamcheti, 1980). The position of the vortex sheet representing the body is known, whereas the vortex sheet representing the wake deforms freely, into a force-free position; thus, there are two types of vortex sheets: one bounded and the other free.

Associated with each closed loop is the value of the circulation around the segments in the loop, a control point where the no-penetration condition is imposed, and an area. The control point is chosen to be the centroid of the corners. Each of the straight segments, except for those in the elements along in the leading-edge of a thin-wing, belongs to two

loops. The circulations of the loops, G_i, are obtained by applying the no-penetration boundary condition, which is

$$\sum_{j=1}^{N} A_{ij} G_j = (\vec{V}_s - \vec{V}_w)_i \cdot \vec{n}_i \qquad (2.1)$$

for i=1,2,...,N. N is the total number of elements representing the body, $\vec{n}_i$ is the unit vector normal to the ith element, and A_{ij} represents the normal component of the velocity at the control point of the ith element (the centroid of the four corners) generated by the unit-circulation loop of discrete vortices around the jth element. $(\vec{V}_s)_i$ and $(\vec{V}_w)_i$ are the velocity of surface of the wing and the velocity induced by the vortex segments in the wake at the control point of the ith element.

In order for the pressures on the upper and lower surfaces of the body along the sharp edges where wakes emanate from the wing to be the same, vorticity must be shed along there. This shed vorticity is convected away from the wing and constitutes the wake. The flow is irrotational everywhere except in the boundary layer of the body, where vorticity is being generated, and in the wake, where shed vorticity is being convected. The segments in the wake convect with the flow at the local particle velocity and, hence, occupy the force-free position. Because the vorticity in the wake now was shed from the wing earlier, the wake serves as the historian of the flow. When a segment in the wake reaches a point far downstream, it is neglected.

2.2.1 Constructing The Numerical Solution: Conditions to be Satisfied

1)Boundary Conditions

I. The disturbances which the body creates vanish at infinity. This condition is satisfied because the velocity calculated by the Biot-Savart law is inversely proportional to the distance from the field point to the vortex tube.

II. The normal component of the velocity of the fluid relative to the surface of the body must be zero

$$(\vec{V} - \vec{V}_s) \cdot \vec{n}_i = 0 \tag{2.2}$$

on the surface, where $\vec{V}$ is the absolute velocity of the fluid particle and $\vec{V}_s$ is the velocity of the lifting surface. $\vec{V}$ is the sum of two parts: one contribution from the wake and one from vorticity on the wing. When $\vec{V}$ is separated, the result is equation 2.1.

2) The force-free position of the wake:

The Kelvin-Helmholtz Theorem requires that in an inviscid fluid all vorticity be transported with the fluid particles. This condition is used to obtain the position of the force-free wake. This theorem can be stated as $\frac{D\Gamma}{Dt} = 0$, where Γ is the circulation of any arbitrary closed loop.

3) The Unsteady Kutta condition:

The Kutta condition requires the pressure difference along the sharp edges of the wing to be zero. This condition is satisfied at each time step by convecting the vorticity along these edges into the wake at the local particle velocity.

2.2.2 Aerodynamic Load for Thick Bodies

The pressure coefficient is calculated from the familiar Bernoulli equation for unsteady flows:

$$C_p = \frac{P - P_\infty}{1/2\rho V_\infty^2} = 1 - \frac{\vec{V} \cdot \vec{V}}{V_\infty^2} - \frac{2}{V_\infty^2} \frac{\partial \Phi}{\partial t}\bigg|_R \tag{2.3}$$

where V_∞ is free-stream velocity, Φ is velocity-potential, $\Big|_R$ denotes the time derivative in the ground reference frame, and ρ is the density of the fluid. The equation above is written in the ground frame. For convenience, in the present work the body frame is used. The partial derivative with respect to time in the inertia frame is related to that in the moving frame by (Konstadinopoulos, 1981):

$$\frac{\partial \Phi}{\partial t}\bigg|_R = \frac{\partial \Phi}{\partial t}\bigg|_g - \vec{V} \cdot (\vec{V_A} + \vec{\omega} \times \vec{r}) \tag{2.4}$$

where $\vec{V}$ is the velocity of the fluid particle in the ground-fixed frame, $\vec{V_A}$ is the velocity of the origin of the body-fixed frame, $\vec{\omega}$ is the angular velocity of the body-fixed frame,

$\Big|_g$ denotes the time derivative in the body-fixed frame, and $\vec{r}$ is the position of the fluid particle in the body-fixed frame. Thus the Bernoulli equation expressed in terms of the body frame quantities can be written as:

$$C_p = 1 - \frac{\vec{V} \cdot (\vec{V} - 2\vec{V_A} - 2\vec{\omega} \times \vec{r})}{V_\infty^2} - \frac{2}{V_\infty^2}\frac{\partial \Phi}{\partial t} \tag{2.5}$$

Computation of Velocity Potential

In order to calculate the derivative of the velocity potential, the value of the velocity potential is needed (of the control point of each element) at every time step.
For an irrotational flow:

$$\vec{V} = \nabla \Phi \tag{2.6}$$

integrating from the control point of the element number j to the element number j+1:

$$\Phi_{(j+1)} - \Phi_{(j)} = \int_j^{j+1} \vec{V} \cdot d\vec{r} \tag{2.7}$$

$$\Phi_{(j+1)} \cong \Phi_{(j)} + \frac{\vec{V}_{j+1} + \vec{V}_j}{2} \cdot (\vec{r}_{j+1} - \vec{r}_j) \tag{2.8}$$

j goes from 1 to N-1, $\vec{V}$ is the velocity of the control point on the element, and $\vec{r}_{j+1} - \vec{r}_j$ is the position of the control point of the element j+1 relative to the one of elment j. The above equation can also be used to calculate $\Phi_{(1)}$ by beginning from a position in space where the value of Φ is known, far away from the body, and marching toward the element number one on the body. The velocity potential on element j is given by:

$$\Phi_{(j)} = \Phi_{(1)} + \sum_{k=1}^{j-1} \frac{\vec{V}_{k+1} + \vec{V}_k}{2} \cdot (\vec{r}_{k+1} - \vec{r}_k) \tag{2.9}$$

for j=2,...,N.

The force on each element can be calculated by:

$$\vec{F} = \sum_{j=1}^{N} (C_{p_j} A_j) \vec{n}_j \tag{2.10}$$

where A_j is area of the jth element. The moment about the origin is given by:

$$\vec{M} = \sum_{j=1}^{N} (\vec{R} \times \vec{F})_j \tag{2.11}$$

where $\vec{R}$ is the position of the control point of the element in the body frame. Substituting for C_p and Φ in the force equation, one obtains:

$$\vec{F} = \sum_{j=1}^{N} \left\{ \frac{-2}{V_\infty^2 \Delta t} \left[\Phi_{(1)} + \sum_{k=1}^{j-1} \frac{\vec{V}_{k+1} + \vec{V}_k}{2} . \Delta \vec{r}_k \right]_t^{t+\Delta t} + 1 - \frac{V^2}{V_\infty^2} \right\} A_j \vec{n}_j \tag{2.12}$$

The constant term $\Phi_{(1)}$ affects the value of the pressure equally at each element, but does not contribute to the resultant loads. Therefore, the contribution from the constant term at every time step is zero.

The force for thin-wings is given by (Konstadinopoulos, 1981):

$$\vec{F} = \sum_{j=1}^{N} \left\{ 1 - \left[\frac{2\Delta \vec{V}}{V_\infty^2} . (\vec{V}_m - \vec{V}_A - \vec{\omega} \times \vec{r}) \right]_i - 2 \frac{\partial (G_i)}{\partial t} \right\} A_j \vec{n}_j \tag{2.13}$$

where $\vec{V}_m$ is the velocity generated at the control point of an element by all the vortex segments of the wing and the wake except those around the element and $\Delta \vec{V}$ is the velocity jump in the tangential direction across the lifting surface. For the derivation of the pressure coefficients and more details on thin-wings the reader is referred to Konstadinopoulos (1981).

The Effect of Time Step

A first-order Euler explicit scheme is used to determine the displacements of the points in the wake:

$$\vec{r}_i(t + \Delta t) = \vec{r}_i(t) + \vec{V}_i(t) \Delta t \tag{2.14}$$

where $\vec{r}_i(t + \Delta t)$ is the position of the point i in the body-fixed frame at time $t + \Delta t$. The value of Δt affects the accuracy of the results. As Δt decreases, the accuracy of the results increases. The time step affects the pressure coefficients everywhere on the wing. Moreover, the time step determines the size of the elements in the wake. Therefore, the value used in the calculation has to allow a smooth transition in the size of the elements from the wing to the wake and still be small enough to provide a time-accurate solution.

Aspect-Ratio Effect

The effect of the wing-tip vortices corresponding to positive lift is to induce a downward component of velocity at and behind the wing, which is called downwash. The magnitude of the downwash at any section along the span is equal to the sum of the effects of the wing-tip vortices on that section; hence, as the aspect ratio increases, the downwash at the mid-span decreases. Therefore, the lift generated by the airfoil section at mid-span increases, and the results obtained at the mid-span of a 3-D thick wing using the UVLM converge to the results obtained using a 2-D unsteady panel method as the aspect ratio increases.

2.3 Two-Dimensional Panel Method

The results from the UVLM are compared with the results obtained from the exact steady-state solution. For unsteady flowfields, the present results are compared with the results obtained from a two-dimensional panel method.

A unit circle in the z-plane is mapped into the Karman-Trefftz airfoil in the ζ-plane through the transformation:

$$\frac{\zeta - nc}{\zeta + nc} = \frac{(z-c)^n}{(z+c)^n} \tag{2.15}$$

on the unit circle with its center at z=A, $z - A = e^{i\theta}$, where n is related to the angle on the airfoil at the trailing edge by $n = 2 - \lambda/\pi$, λ is the trailing-edge angle, and c is the location of the point on the circle in the z-plane which maps into the trailing edge in the ζ-plane. From the above:

$$\zeta = \frac{nc[(z+c)^n + (z-c)^n]}{(z+c)^n - (z-c)^n} \tag{2.16}$$

the velocity on the airfoil in the ζ-plane is given by:

$$\mu - i\nu = i[-2\sin(\alpha - \theta) + \frac{\Gamma}{2\pi}]e^{-i\theta}\frac{[(z+c)^n - (z-c)^n]^2}{4c^2n^2(z^2-c^2)^{n-1}} \tag{2.17}$$

where α is the angle of attack, and μ and ν are velocities on the airfoil in the ζ-plane. This is the exact steady-state velocity on the airfoil.

The present model used is a cambered Karman-Trefftz airfoil of $\theta = 5$ degrees and $n = 1.93$. To satisfy the Kutta condition, circulation around the airfoil is:

$$\Gamma = 4\pi \sin(\alpha - \theta_{T.E.}) \quad . \tag{2.18}$$

For more information about the 2-D panel method the reader is referred to Dong (1987).

2.4 Numerical Results and Comparisons

Thin Lifting Bodies

The UVLM was used to calculate the loads on a rectangular, uncambered wing of unit aspect ratio. Steady results are computed from the general unsteady algorithm by giving the wing an impulsive start and then having it move at a constant velocity until the steady state develops. In Figure 2.1 the present results are compared with the experimental data obtained by Belotserkovskii (1977). The present solution is in good agreement with the experimental data. The computed wake behind a rectangular wing of unit aspect ratio is shown in Figure 2.2, for an angle of attack of 20 degrees. The wing-tip vortex systems are curl as one would expect. These vortical structures originate at the intersection of the leading edge, with the wing-tip increasing in diameter. The well-known starting vortex is not shown, due to the impulsive start, since the wake was cut after the wing had traveled approximately 3 chord lengths. The contribution of the segments of the wake far downstream is not significant, and by cutting the wake computational time is saved.

The present results are compared with the experimental data obtained by Chang (1985) for the tapered wing of an F-104A in Figure 2.3. Again, there is good agreement. In order to check the ability of the method to model a wing in ground effect, the present method was applied to an F-104A wing. In Figure 2.4 the present results are shown to be in good agreement with the experimental data obtained by Chang for the coefficients of lift and drag. However, the agreement between the present solution and the experimental data for the moment is not good. The data for the moment in ground effect do not follow the same

trend as the data for the wing out of ground effect. Near the ground, there seems to be a problem with the data.

NonLifting Bodies

The UVLM was applied to a sphere of unit radius in a uniform stream parallel to the z-axis. In Figure 2.5 the present results are compared with the analytical solution. The figure shows that there is a good agreement between the present solution and the analytical solution.

The UVLM was then applied to a cylinder with a finite aspect ratio. L/D, where L is the length and D is the diameter of the cylinder, is 5.5 and the ends of the cylinder are open. In Figure 2.6a the mid-span velocities of the cylinder are compared with the exact solution of the flow around a circle. In order to investigate if there is an end effect, the method was applied to the same cylinder, but with closed ends, in Figure 2.6b. Comparing Figure 2.6a with Figure 2.6b shows that the mid-span of the cylinder is not affected by the condition of the ends. In Figure 2.6 it is shown that as the value of θ increases, the inequality between the present calculation and the exact solution becomes more noticeable. In Figure 2.7 (a-c) the mid-span velocities of the cylinder with different L/D are compared with the exact solution. As the value of L/D increases, the agreement between the present results and the exact solution grows closer. In Figure 2.7c where L/D=33, the present results are in excellent agreement with the exact solution.

The UVLM is then applied to a more complex geometry, a cone-cylinder. In Figure 2.8 the present computed results are compared with the experimental data obtained by Faulkner et al. (1964) for pressure coefficients. Again, there is a good agreement between the present results and experimental data.

Thick 2-D Wings

The exact steady-state pressure distribution for a Karman-Trefftz airfoil is shown in Figure 2.9. The angle of attack is 8 degrees. In Figure 2.10 the calculated pressure coefficients obtained from continuous vorticity unsteady panel method when the time step is .000055

are shown. The figure shows the calculated pressure coefficient for d/C=.1 and d/C=.5, where d is the distance the wing has traveled and C is the chord length. Figure 2.11 shows the calculated pressure coefficients obtained from the same method, but when the time step is .00055. The effect of time step is noticeable in comparing Figure 2.11b and Figure 2.10b near the trailing edge. The time step, Δt, plays a role in the accuracy of the wake because the position of the wake is found from a first-order explicit Euler scheme. Those elements on the body which are closer to the trailing edge are closer to the wake; hence, the wing is more influenced by the wake near the trailing-edge. Therefore, Δt has its primary effect near the trailing-edge. Figure 2.11 shows that as d/C increases, the calculated pressure coefficients approach the exact steady-state solution, in Figure 2.9.

The computed wake and airfoil are shown in Figure 2.12a, and an enlarged view of the wake is shown in Figure 2.12b. In this case, the wing has traveled approximately 0.5 chord. Each dot in the figure represents the location of a discrete vortex shed earlier from the trailing edge. The spacing of the cores is often so dense that the representation of the wake appears to be a continuous line rather than a collection of discrete points. The initial starting vortex is clearly visible at the end of the wake. Moreover, it can be seen that between the trailing edge and the starting vortex the wake is breaking up, forming somewhat isolated agglomerations of vorticity. This phenomenon seems to be consistent with observations and would be responsible for fluctuations in the pressure on an object in or near the wake. The computed wake and airfoil for the case where the wing has traveled 4 chord lengths are shown in Figure 2.13.

Thick 3-D Wings

For further evaluation of UVLM, the method is applied to thick wings of very high aspect ratio. Then the results are compared with those obtained by a continuous-vorticity panel method.

In Figure 2.14a the pressure coefficient calculated at the mid-span of a wing with an aspect-ratio of 11 by the UVLM is shown. The time step used to convect the wake is 0.166.

The results from the UVLM are not in very good agreement with those obtained using the panel method (Figure 2.11c), particularly near the trailing edge. The difference is due to the time step used in the calculation. The time step affects the pressure coefficients everywhere on the wing, but especially near the trailing edge. The time step determines the size of the elements in the wake. Therefore, the value used in the calculation has to allow a smooth transition in the size of the elements from the wing to the wake and also be small enough to provide a time-accurate solution. Figures 2.14 (a-c) show the effect of the time step. In all cases the predicted loading near the trailing edge is quite large and qualitatively in agreement with the observations. As the time step decreases, the present results come into close quantitative agreement with those from the more refined continuous-vorticity panel method. The pressure on the upper and lower surfaces don't match near the trailing edge unless a small time step is used.

In Figure 2.15 the calculated pressure distribution obtained from the UVLM for different aspect-ratios is compared with the exact steady-state solution. Steady-state results are obtained with the general UVLM by giving the wing an impulsive start and then having it move at constant velocity until the steady-state develops. The numerical results approach the exact solution as the aspect-ratio increases. The unsteady results are shown after the wing has traveled twenty-five chords and are compared with the exact steady-state solution. There is better agreement with the exact steady-state solution when the wing travels further. As the value of the time step decreases and the aspect-ratio increases, the comparison with the exact solution improves.

In Figure 2.16, the calculated wake using the UVLM is shown. The figure shows the curling of the vortices due to the impulsive start. Although vortices are not shed from the wing-tip, the wake does curl along its streamwise edges and these vortices have some effect on the pressure at mid-span. As the angle of attack increases, these vortices become stronger and they have more influence on the pressures at mid-span. As the aspect ratio increases, the influence of these vortices on the pressure distribution is reduced. The side view of the wing and the wake obtained from the UVLM are shown in Figure 2.17. In this

figure the wing has traveled one chord and the aspect ratio is 5.54. The dots locate the ends of the discrete vortex segments that represent the wake. Again, the curling of the vortices due to the impulsive start is shown.

2.5 Conclusion

The UVLM was applied to thin and tapered wings and the results are in good agreement with the experimental data. The method is capable of giving accurate lift and moment coefficients for a wing in ground effect. The method can predict the aerodynamic load on thick nonlifting bodies. The UVLM was applied to a sphere, cylinder, and cone-cylinder. The computed results are in good agreement with the analytical and experimental data.

The general UVLM can model wings in steady and unsteady flows. The method is capable of giving accurate pressure distributions on thick lifting bodies in both steady and unsteady flowfields. The method is sensitive to the time step used in the calculation, particularly for an unsteady flowfield. The aspect ratio affects the pressure distribution on the wing at mid-span.

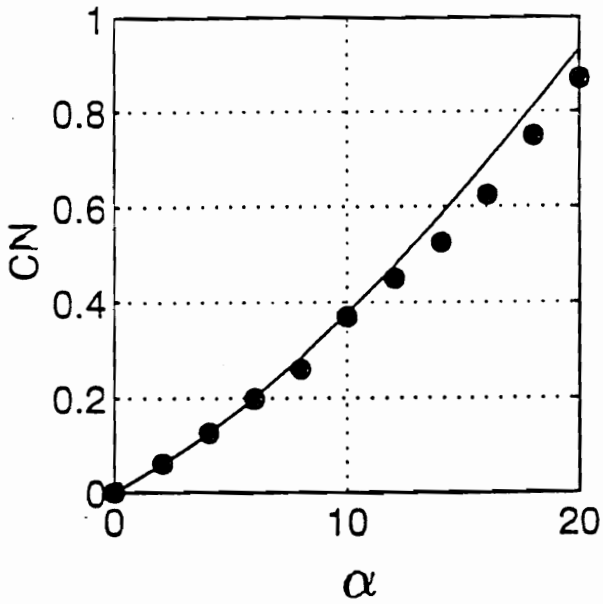

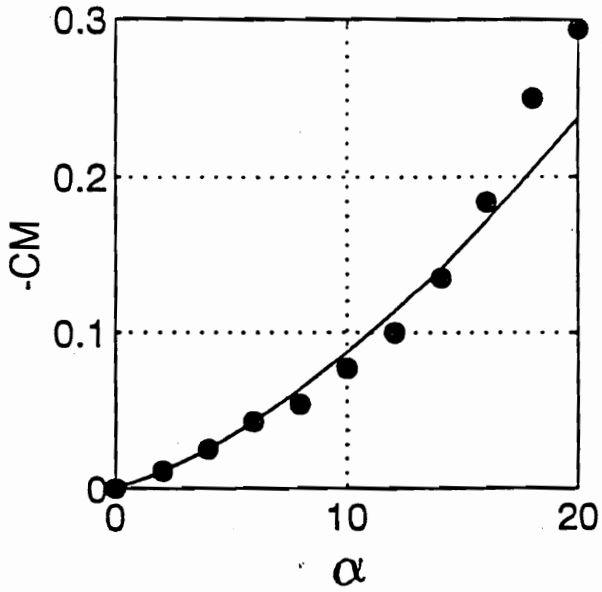

Figure 2.1: Comparison of numerically predicted normal force and moment coefficients as functions of angle of attack with the experimental data.
- Present solution
• Experimental Data of Belotserkovskii

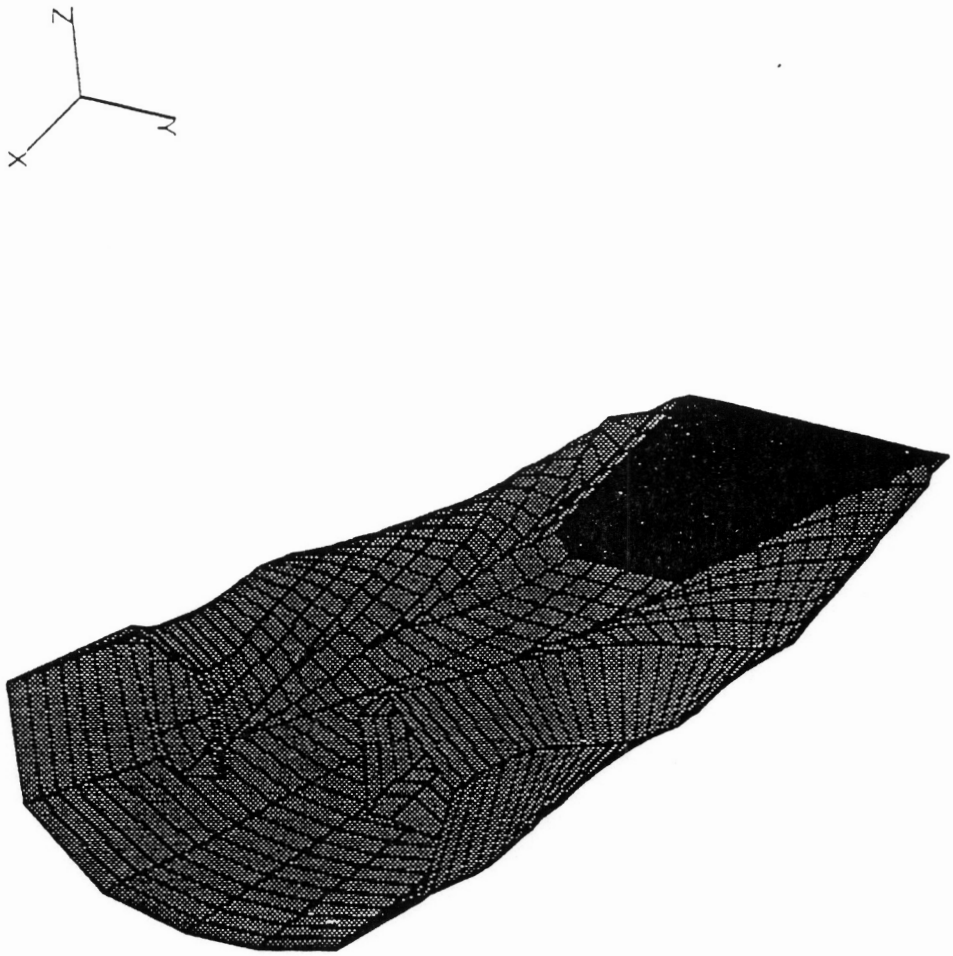

Figure 2.2: Computed wakes for a rectangular wing of unit aspect ratio with 20 degrees angle of attack.

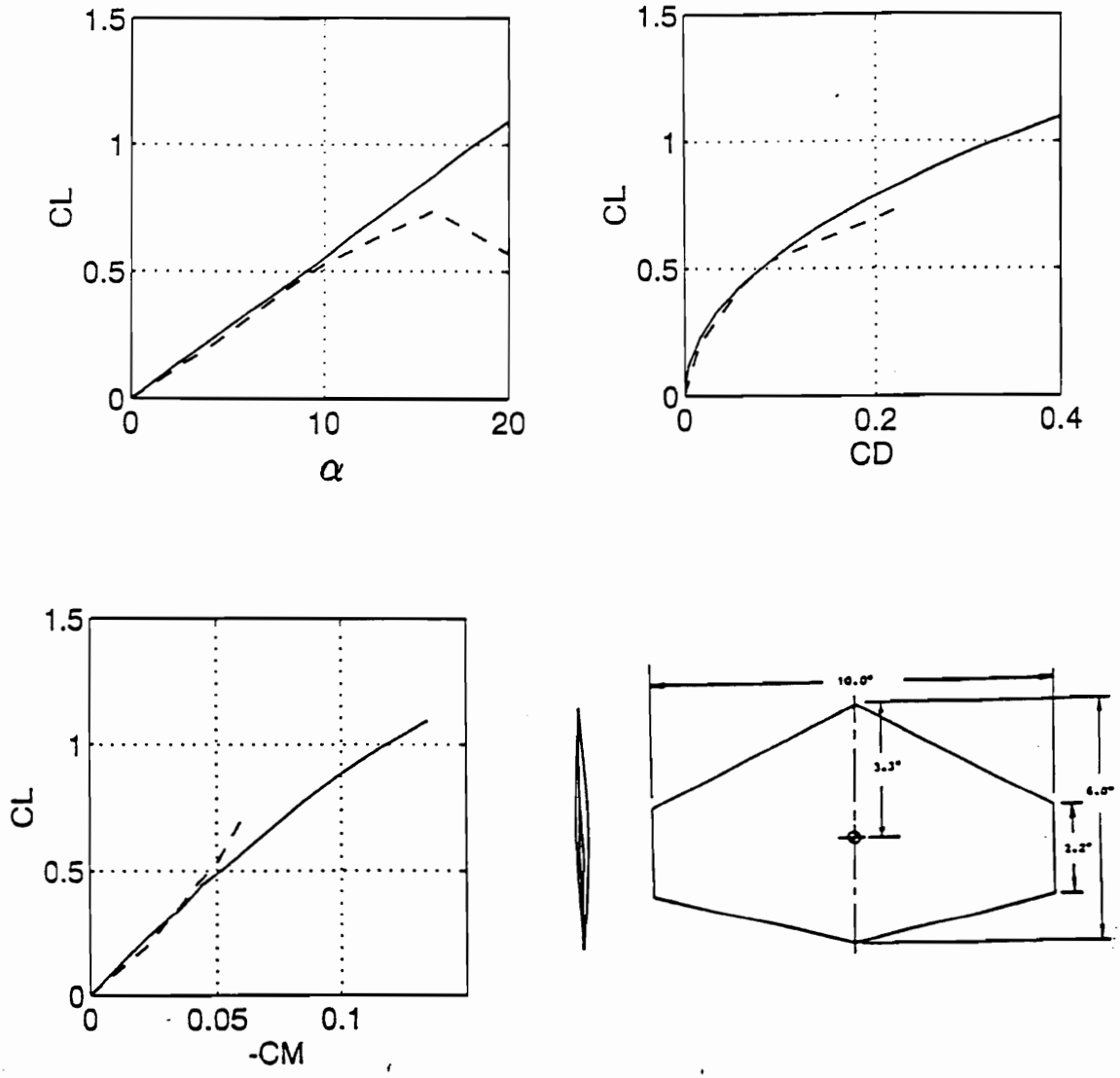

Figure 2.3: Comparison of numerically predicted lift, drag, and moment coefficients with the experimental data for a wing of F104-A type.
— Lattice method
- - Experimental Data of Chang

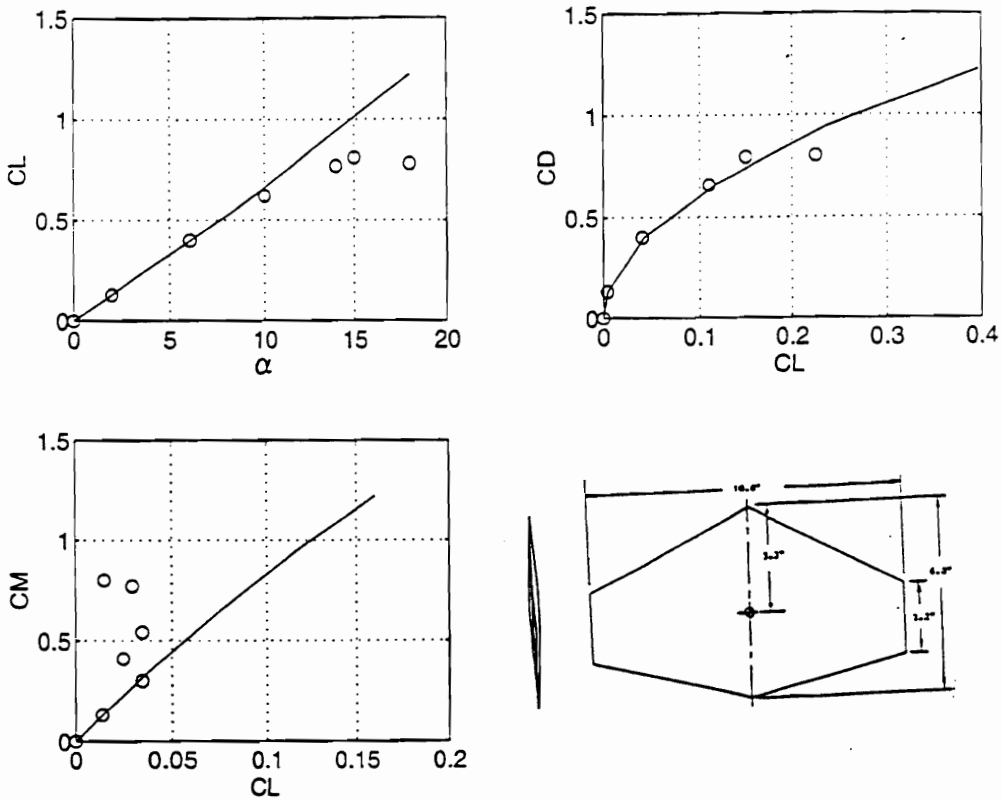

Figure 2.4: Comparison of numerically predicted lift, drag, and moment coefficients with experimental data for an F104-A in ground effect. The height above the ground is 0.28 span and is measured 3.3 inches behind the apex.
- Present solution
o Experimental Data of Chang

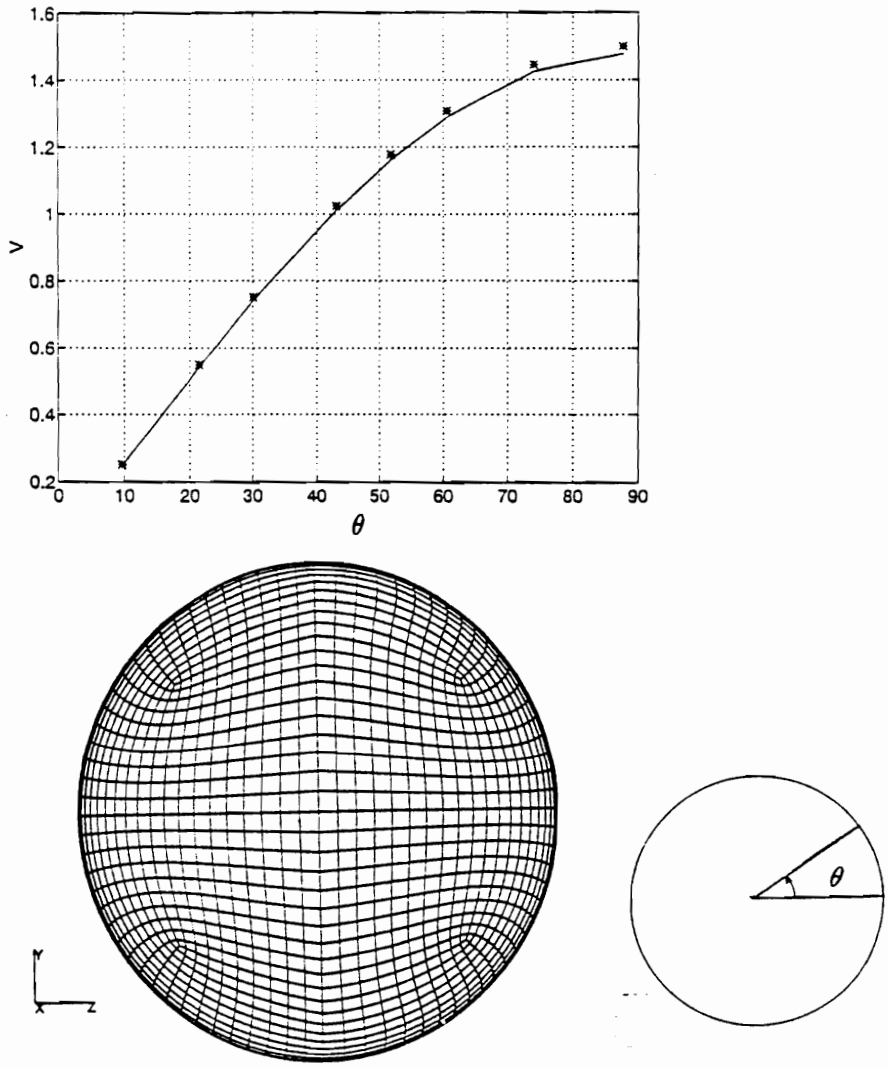

Figure 2.5: Comparison of numerically-calculated velocity as a function of position with the exact solution for a sphere of unit radius.
- Lattice method
* Exact solution

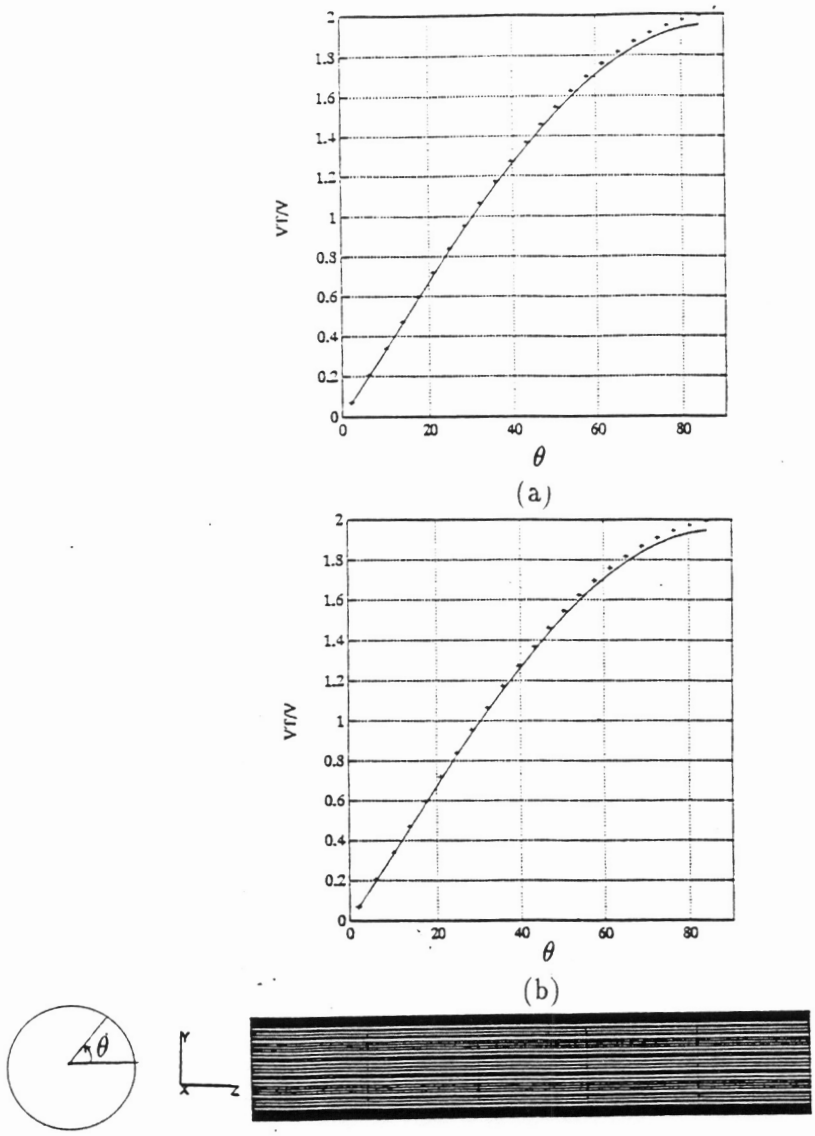

Figure 2.6: Comparison of numerically calculated velocity in the mid-span of a cylinder, L/D=5.5, with the exact solution of flow over a circle in a uniform-stream parallel to the x-axis. (a) open ends cylinder and (b) closed ends cylinder.
– Mid-span velocity using the vortex-lattice method.
+ Velocity of flow over a circle using the exact solution.

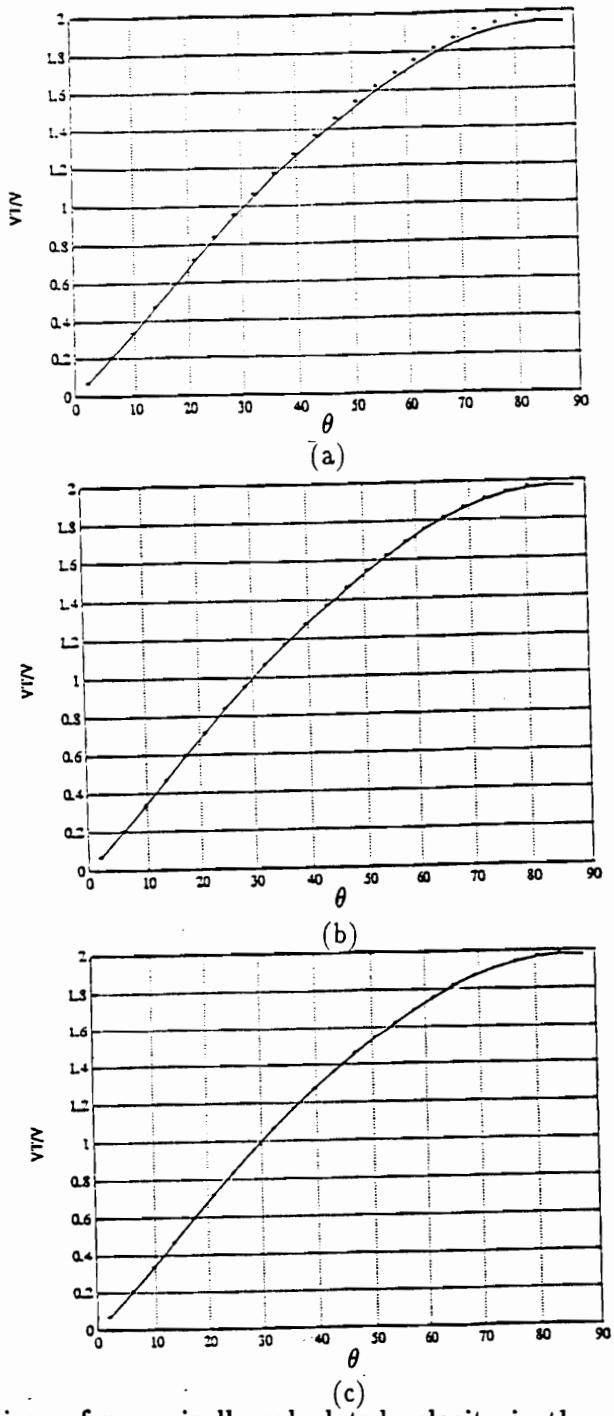

Figure 2.7: Comparison of numerically calculated velocity in the mid-span of a cylinder with the exact solution of flow over a circle (a) L/D=11, (b) L/D=22, and (c) L/D=33.
– Mid-span velocity using vortex-lattice method.
+ Velocity of flow over a circle using the exact solution.

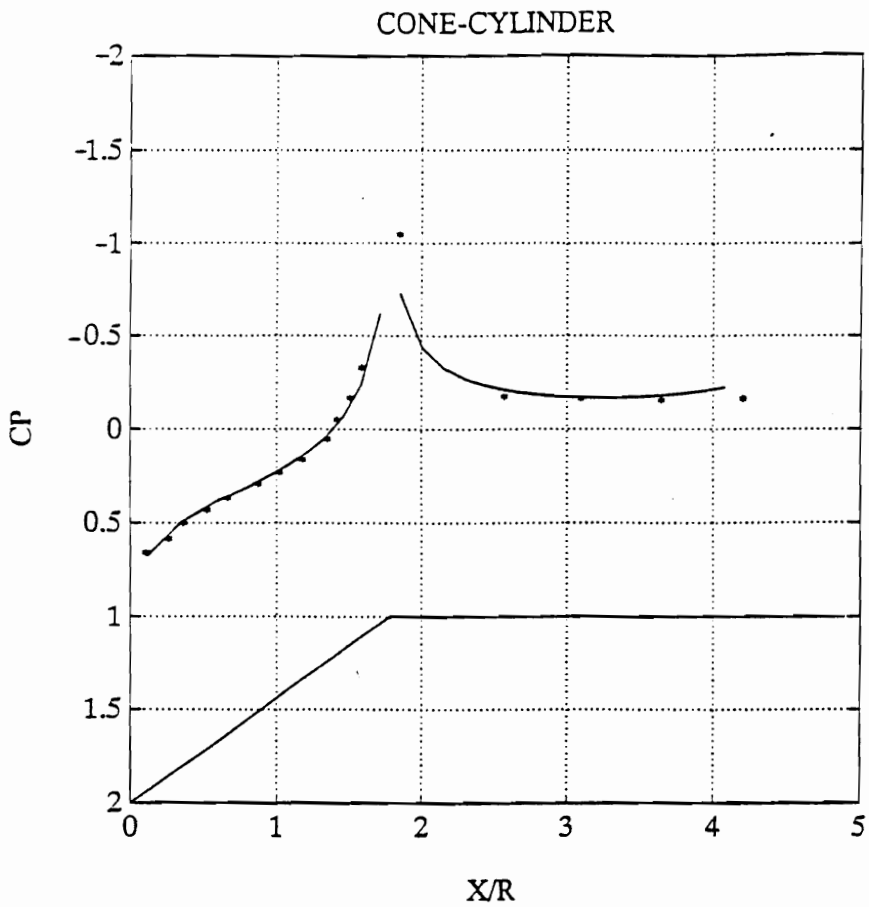

Figure 2.8: Comparison of numerically predicted velocity with the experiment for a cone-cylinder with zero angle of attack.
- Vortex-lattice method
* Experimental Data of Faulkner

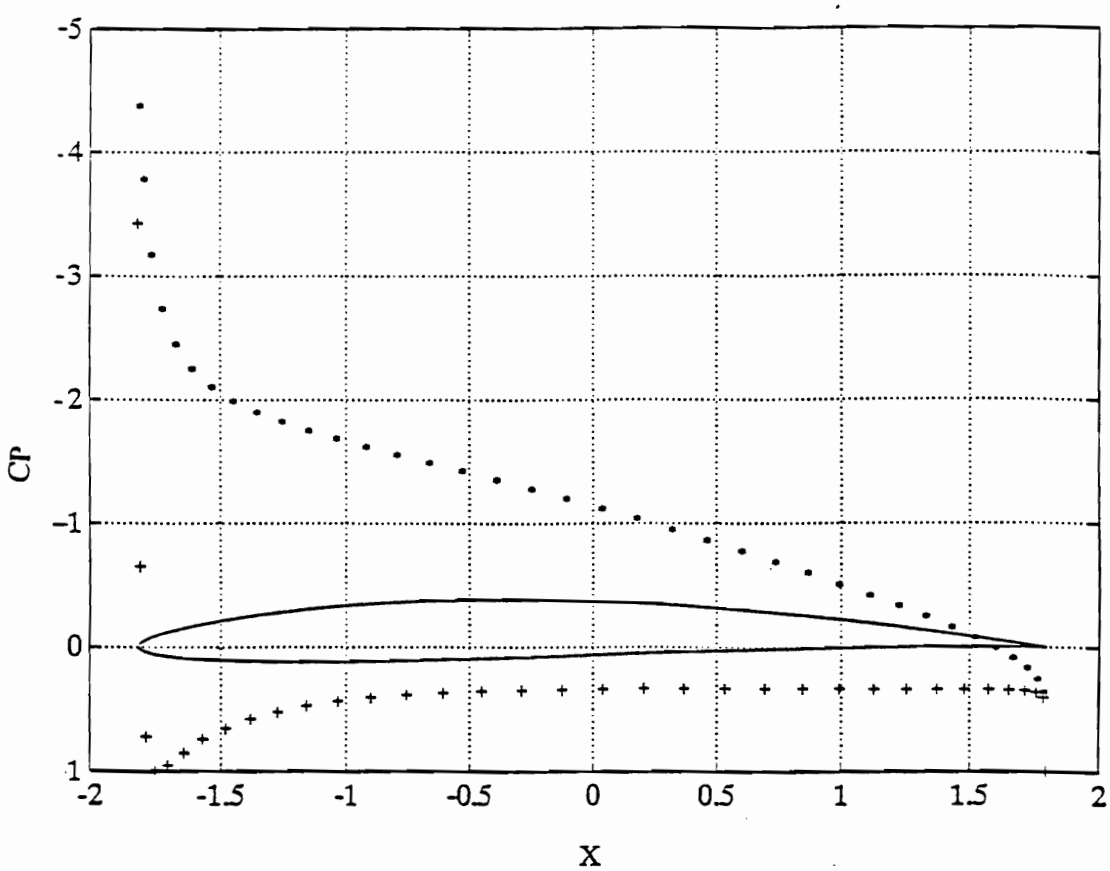

Figure 2.9: Exact steady-state solution for flow over a Karman-Trefftz airfoil with 8 degrees angle of attack.

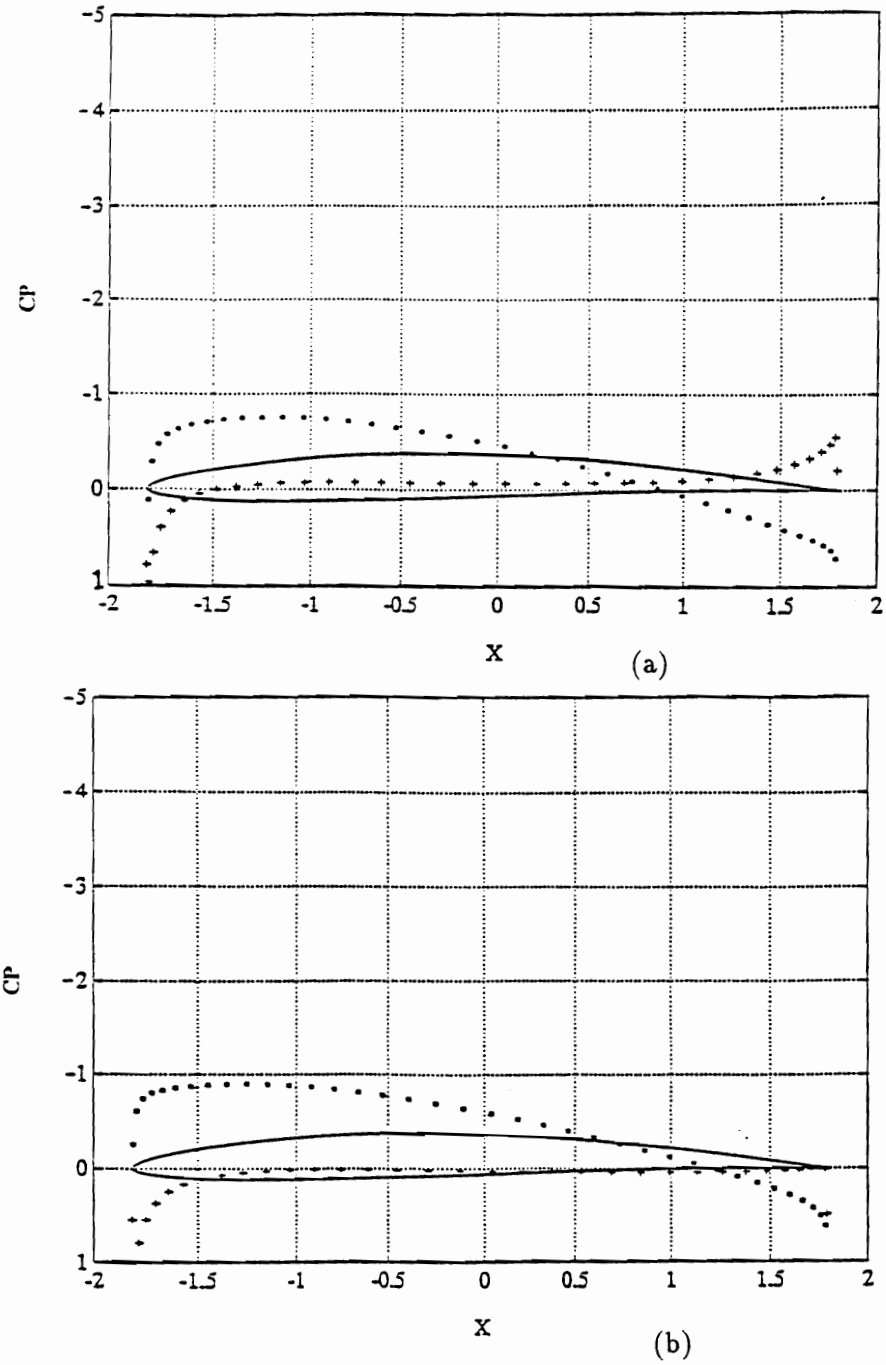

Figure 2.10: Pressure coefficient as a function of position using 2-D unsteady panel method, 72 elements, 8 degrees angle of attack, .000055 time step. The wing has traveled (a) .1 Chord and (b) .5 Chord.

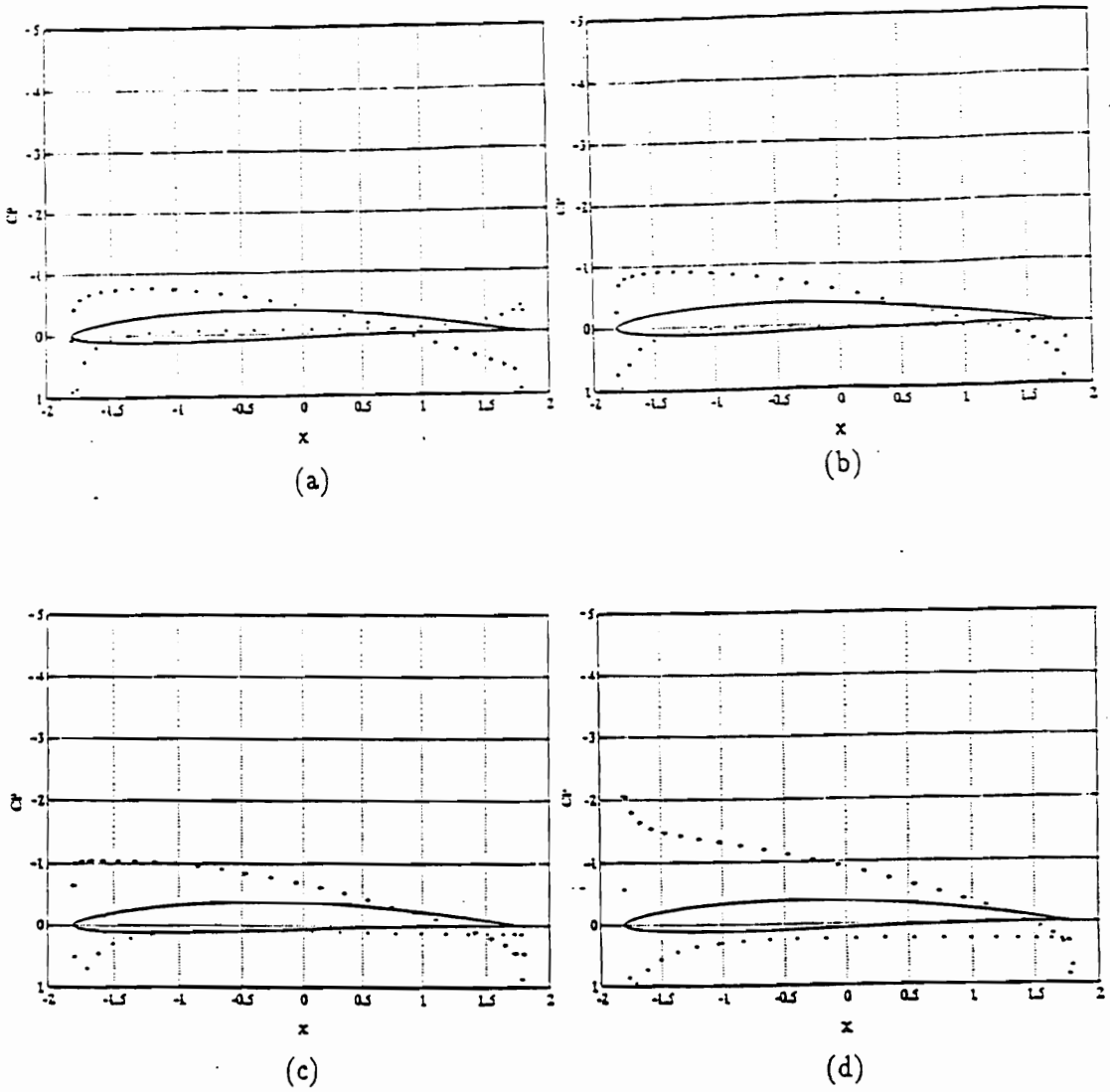

Figure 2.11: The pressure coefficient as a function of position using the 2-D unsteady panel method, 50 elements, 8 degrees angle of attack, .00055 time step. The wing has traveled (a) .1 chord, (b) .5 chord, (c) 1 chord, and (d) 4 chords.

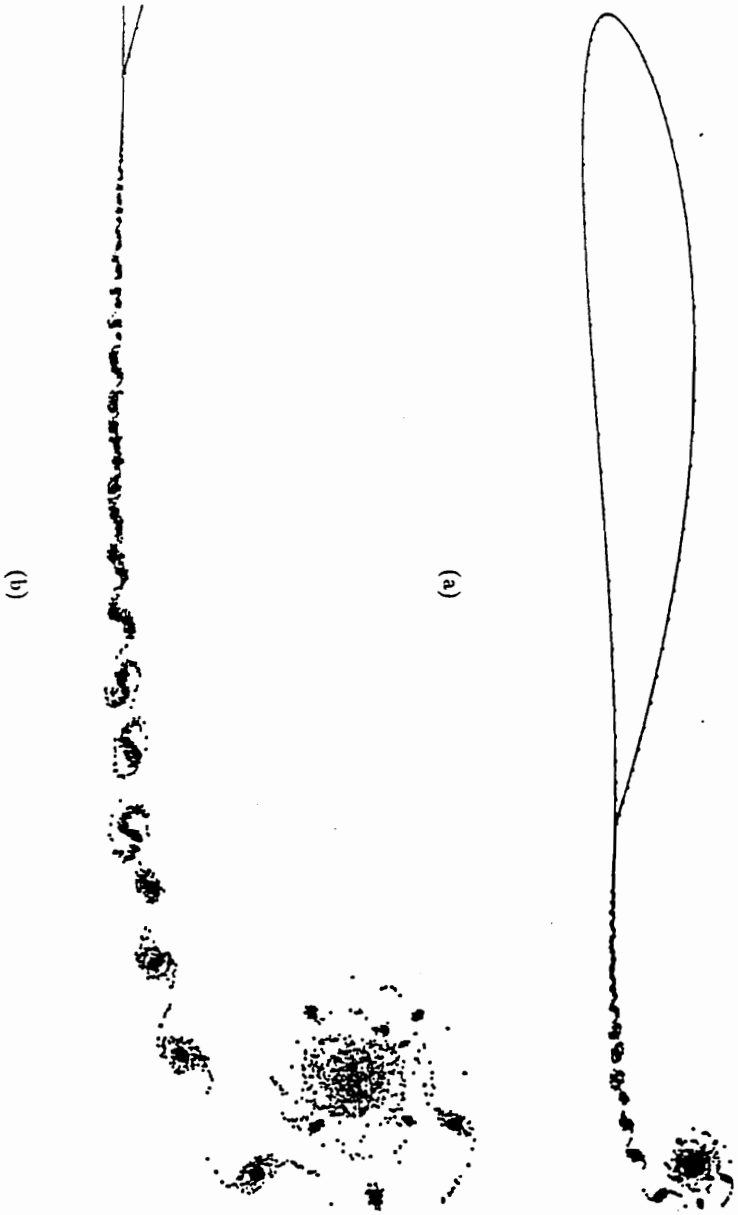

Figure 2.12: Computed wakes for a Karman-Trefftz airfoil with 8 degrees angle of attack, after the wing has traveled .5 chord.

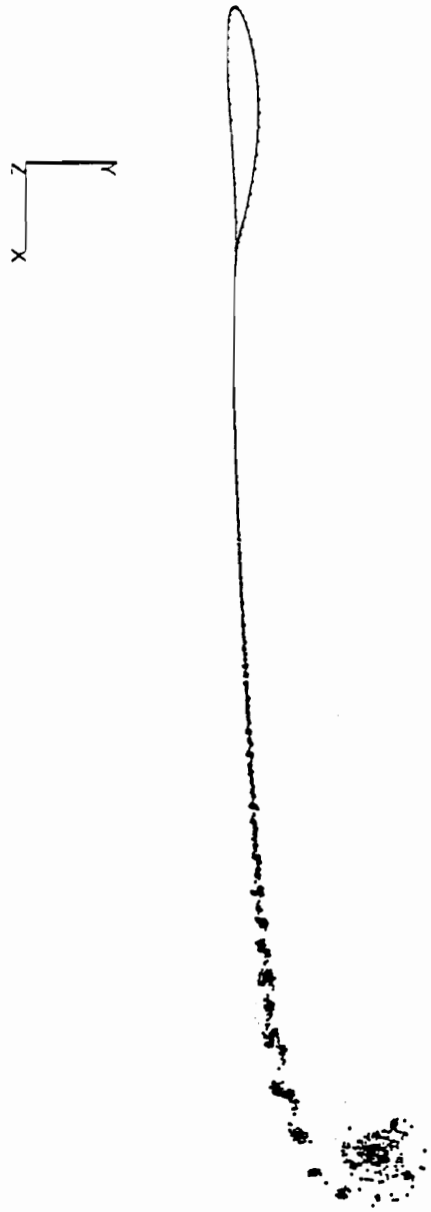

Figure 2.13: Computed wakes for a Karman-Trefftz airfoil with 8 degrees angle of attack, after the wing has traveled 4 chords.

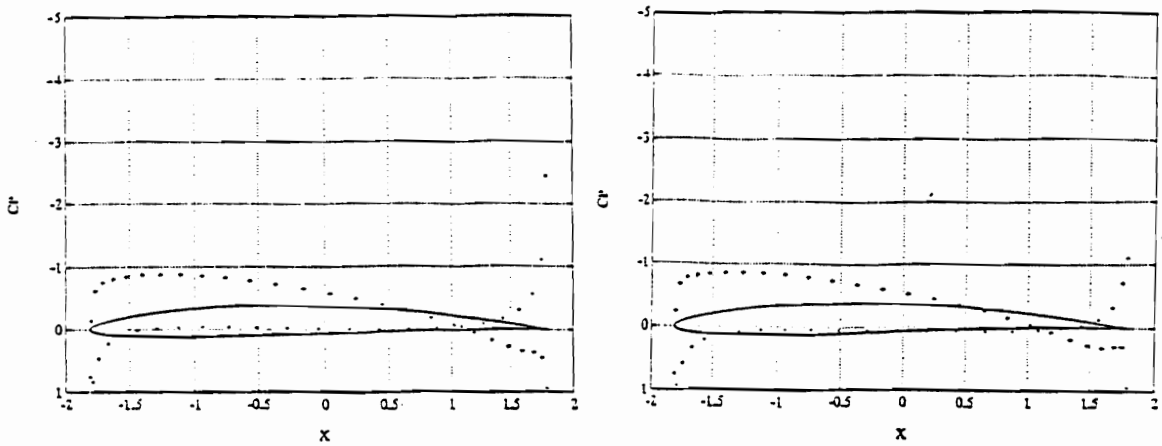

(a)

(b)

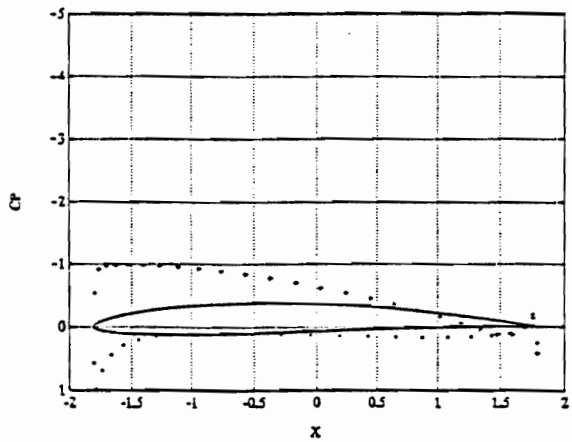

(c)

Figure 2.14: Calculated pressure distributions for flow over a 3-D Karman-Trefftz airfoil, 8 degrees angle of attack. The wing has traveled one chord and the aspect ratio is 11.1. The unsteady vortex lattice method is used.
a) Time step = .166
b) Time step = .083
c) Time step = .0083

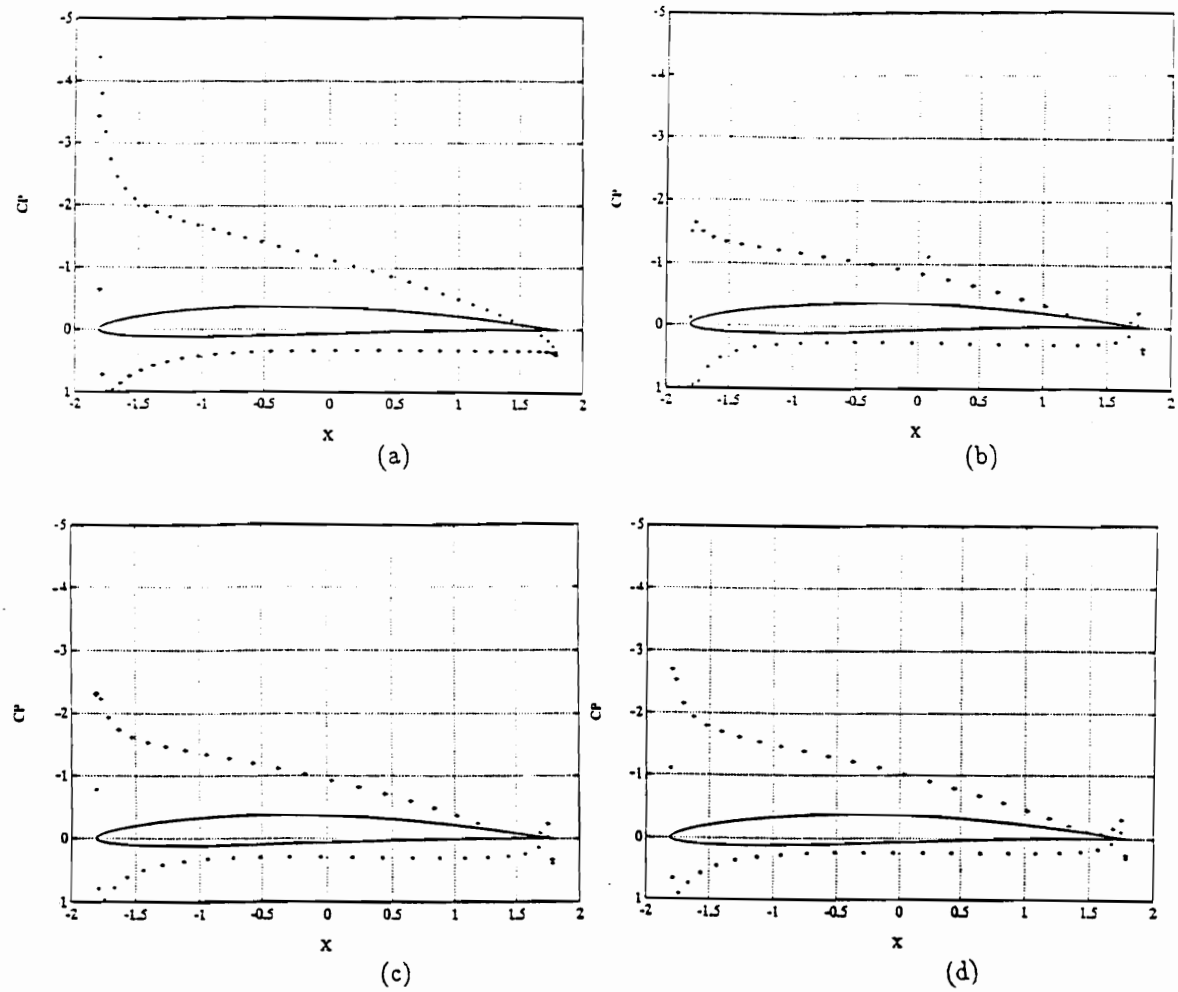

Figure 2.15: Calculated pressure distributions for flow over a Karman-Trefftz airfoil, 8 degrees angle of attack.
a) 2-D wing, exact steady-state solution
b) Vortex-lattice solution for aspect ratio = 5.5
c) Vortex-lattice solution for aspect ratio = 11
d) Vortex-lattice solution for aspect ratio = 16.6
In parts b), c), and d) the time step is .166 and the wing has traveled 25 chords following the impulsive start.

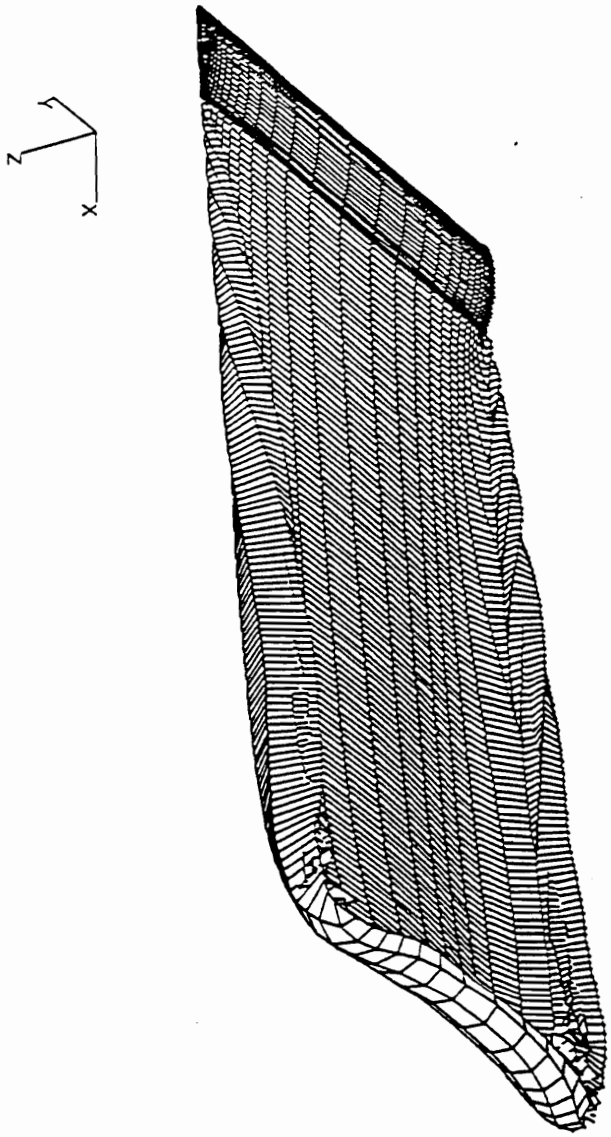

Figure 2.16: Computed wakes for a 3-D Karman-Trefftz airfoil with 8 degrees angle of attack. The aspect ratio is 5.5.

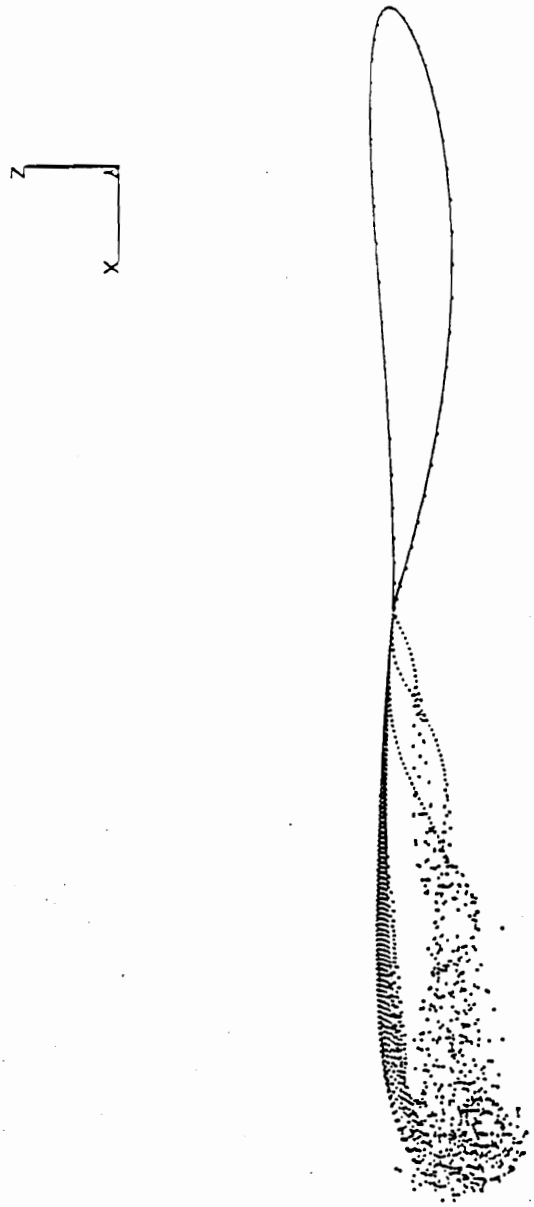

Figure 2.17: Computed wakes for a Karman-Trefftz airfoil with 8 degrees angle of attack. The aspect ratio is 5.5 and the wing has traveled 1 chord.

Chapter 3

WING IN HEAVING OSCILLATORY MOTION

3.1 Introduction

The aerodynamic characteristics of an aircraft are known to be influenced by the proximity of the ground. At the beginning of the twentieth century, it was observed that airplanes take off easily and tend to 'float' during landing. The interaction of the aircraft with the ground is known as 'ground effect'. There is an interest in designing airplanes to operate near the ground since there is a marked increase in the ratio of lift to drag that occurs when a wing flies near the ground. An aircraft can also fly near the surface of the ocean from continent to continent. In order to use such an airplane in transoceanic flight, the effect of the ocean waves on the performance of the craft needs to be investigated. As a first approximation to a wing flying low over a wavy surface, the performance of the wing in an oscillatory heaving motion is investigated. Furthermore, the effect of the value of the frequency of the oscillation is studied. As a means of establishing the credibility of the numerical model for an oscillating wing, the UVLM is used to compute the loads on a wing with a NACA 0012 profile. The results are compared with the experimental data. Then

the method is applied to the problem of interest.

3.2 Description of the Simulation

A rectangular cambered wing of unit aspect ratio (small aspect ratios are desirable for wingships) oscillating in heave at various mean heights above a plane surface is considered in the present analysis. The time-dependent height of the wing above the ground, H, is given by $H = h + A\sin\theta$, where h is the mean height, A is the amplitude of the oscillation, $\theta = 2\pi t/T = \omega t$, T is the period of the heaving motion, ω is the angular velocity, and t is time. $H' = H - h$ is the vertical position of the wing with respect to the mean height above the ground. The relationship between ω and k is given by $k = \omega C/2V_\infty$, where C is the chord length, V_∞ is the free-stream velocity, and k is the reduced frequency.

In the limit where λ (wave length) $\gg A\sin\theta$, $\lambda \gg C$, and $\lambda \gg h$, the wave appears to be a flat surface moving in a vertical direction to the wing. The vertical motion of the wave induces an apparent vertical component to the oncoming stream. A wing flying close to the surface is affected by this disturbance. Hence, the relative angle of attack changes. The angle of attack increases as the surface moves up and decreases as the surface moves down. In the present work, the ground is considered a stationary flat surface and steady. The vertical motion of the wave is simulated by having the wing oscillate in heave.

3.3 The Mean Aerodynamic Load

In the present simulation, the height above the ground is given by:

$$H = h + A\sin\theta \tag{3.1}$$

where the effect of the heaving oscillation on the mean aerodynamic load for one period can be calculated as follows:

$$C_{L_{MEAN}} = \frac{1}{2\pi}\int_0^{2\pi} C_L d\theta \tag{3.2}$$

Using the trapezoidal rule, one can evaluate the integral in the equation above:

$$\begin{aligned} C_{L_{MEAN}} = & \quad [C_L(0) + C_L(\Delta\theta)]\frac{\Delta\theta}{2} \\ + & \quad [C_L(\Delta\theta) + C_L(2\Delta\theta)]\frac{\Delta\theta}{2} + \ldots \\ + & \quad [C_L(n-1)\Delta\theta + C_L(n\Delta\theta)]\frac{\Delta\theta}{2} \end{aligned} \tag{3.3}$$

where $\Delta\theta = \theta_2 - \theta_1 = \frac{2\pi}{T}(t_2 - t_1)$

$$\begin{aligned} C_{L_{MEAN}} = & \quad \frac{1}{T}\left\{\frac{1}{2}[C_L(0) + C_L(n\Delta\theta)]\right. \\ + & \quad \left. C_L(\Delta\theta) + C_L(2\Delta\theta) + C_L[(n-1)\Delta\theta]\right\} \end{aligned} \tag{3.4}$$

$C_{D_{MEAN}}$ and $C_{M_{MEAN}}$ are calculated the same way and are given below:

$$\begin{aligned} C_{D_{MEAN}} = & \quad \frac{1}{T}\left\{\frac{1}{2}[C_D(0) + C_D(n\Delta\theta)]\right. \\ + & \quad \left. C_D(\Delta\theta) + C_D(2\Delta\theta) + C_D[(n-1)\Delta\theta]\right\} \end{aligned} \tag{3.5}$$

$$\begin{aligned} C_{M_{MEAN}} = & \quad \frac{1}{T}\left\{\frac{1}{2}[C_M(0) + C_M(n\Delta\theta)]\right. \\ + & \quad \left. C_M(\Delta\theta) + C_M(2\Delta\theta) + C_M[(n-1)\Delta\theta]\right\} \end{aligned} \tag{3.6}$$

3.4 Results

In Chapter 2, it was shown that UVLM can predict the aerodynamic load on a wing in and out of ground effect. To further establish confidence in the method as a model for an oscillating wing, it is used here to calculate the loads on a wing with a NACA 0012 profile and an aspect ratio of 30 oscillating sinusoidally in pitch about the quarter chord. The numerical results are then compared with the observations of McCroskey et al. (1981). In Figure 3.1 the calculated mid-span aerodynamic load is shown. In this example, the mean angle of attack is 3 degrees and the amplitude of the oscillation is 10 degrees. The reduced frequency, defined as $k = \omega C/2V_\infty$, is 0.1. McCroskey et al. gave other results, but for

higher angles of attack that produced separation. The present solution agrees well with the data.

3.4.1 Oscillation With High Frequency

Small aspect ratios are desirable for surface-effect aircraft. Because the wing-tip vortex systems influence the flow over a significant percentage of the whole wing, small aspect ratios often present difficult problems for classical lifting-surface approximations, but this is not true for the general vortex-lattice method. A rectangular cambered wing of unit aspect ratio is used for the remaining examples. The nominal angle of attack for the stationary wing is 3 degrees. The amplitude of oscillation is 0.25 chord, C_M is the coefficient of moment about the quarter chord, and C_L is the coefficient of lift. In Figure 3.2, the aerodynamic loads and the vertical position of the wing are shown as functions of the distance traveled for a wing in an oscillatory heaving motion. The mean height of the trailing edge of the wing in ground effect is 0.5 chord. These results were obtained by first fixing the wing at 3 degrees angle of attack until a steady state developed and then having it oscillate in heave at an amplitude of 0.25 chord and at a rather high frequency of $\pi/2$. The solid lines are the results for the wing in ground effect, and the broken lines are the results for the wing out of ground effect. The two sets of results are nearly the same because the frequency is so high that its effect overwhelms the ground effect. It is interesting to note that the peak lift force occurs slightly before both the peak-induced drag and minimum pitch moment. The latter two extrema occur almost simultaneously, and all occur noticeably after the low point of motion is reached. The peak loads are rather high as a result of the very rapid oscillation. The symmetry about zero loads is destroyed by the mean angle of attack and the ground.

3.4.2 Oscillation With Low Frequency

In Figures 3.3, 3.4, and 3.5 the aerodynamic loads are plotted as functions of the distance traveled for k=$\pi/16$, $\pi/32$,and $\pi/64$, respectively; all three of these reduced frequencies are considerably lower than the one in Figure 3.2. The differences between the loads in ground

effect (solid lines) and those out of ground effect (broken lines) are now clearly evident. In both cases (high and low frequencies) and for all frequencies, the peak lift occurs before the peak induced drag and the minimum pitch moment, as is the case when k=$\pi/2$. But now, unlike the situation when k=$\pi/2$, all three occur before the low point in the oscillation.

As the frequency is decreased, the peaks tend to flatten, last longer, and be smaller. This behavior is more pronounced in ground effect than out of ground effect. In ground effect, the wing tends to carry the high loads longer. Here the shape of the curves deviates from a sinusoidal form much more than it does when k=$\pi/2$.

3.4.3 The Effect of The Reduced Frequency

In Figures 3.6 and 3.7 the influence of the reduced frequency on the lift, drag, and moment in ground effect is shown. The figures compare the aerodynamic load for the frequencies of $\pi/2$, $\pi/4$, $\pi/8$, $\pi/16$, $\pi/32$, and $\pi/64$. There is a shift in the phase of the aerodynamic loads, and this shift decreases as the value of the reduced frequency decreases. Furthermore, higher peak aerodynamic loads occur as the reduced frequency increases. In Figures 3.8 and 3.9 the aerodynamic loads are compared for different values of reduced frequencies out of ground effect. There is a shift in the phase on the aerodynamic loads. The magnitude of the aerodynamic load for a wing out of ground effect decreases faster as the reduced frequency decreases (Figures 3.8 and 3.9), in comparison with the wing in ground effect (Figures 3.6 and 3.7). The oscillation and the ground increase the magnitude of the aerodynamic load. As the value of the reduced frequency decreases, the unsteady result approaches its steady-state value. The aerodynamic load does not vary linearly with h. The magnitude of the aerodynamic load is higher for the wing going down than for the wing going up. Therefore, the mean aerodynamic load during one cycle is larger than the steady-state load at the mean height. As the value of reduced frequency increases, this gap decreases.

In Figure 3.10 the mean aerodynamic loads for an oscillating wing are compared with those for a wing in steady flow. The wing is in ground effect. The mean aerodynamic load over one cycle is higher than the load in the steady flow at the mean height. The mean

aerodynamic load approaches the load in steady flow as the reduced frequency decreases. In Figure 3.11 the mean-value of the aerodynamic load on an oscillating wing is compared with the load on a wing in a steady flow out of ground effect.

Comparing the two sets of results, one finds that the mean loads on the wing in ground effect are higher than those on the wing out of ground effect. The trends, however, are quite similar: the mean lift and induced drag increase with frequency and the moment decreases. Of course, trying to augment the lift by oscillating a wing is not practical, although doing so could raise the mean lift. The present results suggest the same effect can be produced by flying low over a wavy surface, and hence, the waves may actually boost the efficiency of a wingship.

The unsteady aerodynamic load is compared with the result of the steady flow for a wing in ground effect in Figures 3.12 and 3.13. The values of the reduced frequencies are $\pi/2$, $\pi/4$, $\pi/8$, $\pi/16$, $\pi/32$, and $\pi/64$. The work is positive for the reduced frequencies of $\pi/2$ and $\pi/4$ and negative for the other values of the frequencies.

3.4.4 Calculated Wake

In the remaining figures, some of the computed wakes of the oscillating wings are shown. The dots locate the ends of the discrete vortex segments that represent the wakes. The computations were carried out by first giving the wing an impulsive start from rest, then having it move forward at a constant velocity and angle of attack until the steady state developed, and finally making it oscillate with a simple harmonic motion in heave. The portion of the wake generated during the initial development of the steady state is clearly visible in the figures. In all cases, the amplitude of the heaving motion is 0.25 chord, the nominal angle of attack is 3 degrees, and for the wing in ground effect, the mean height is 0.5 chord.

In Figures 3.14 and 3.15 the reduced frequency of the oscillation is a rather high, $k=\pi/2$. In both figures, the top and side views are shown. In Figure 3.14, the wing is flying near the ground, and in Figure 3.15, the wing is away from the ground. Comparing the two figures,

one sees that the ground clearly restricts the vertical extent of the wakes and increases the horizontal extent. Spreading the wake horizontally generally has the beneficial effect of making the wing appear to have a larger aspect ratio than it actually has.

In both figures the wings are approaching the low points of their trajectories. Near the low points of the trajectories, the wing in ground effect develops more lift and therefore sheds more vorticity than the other wing, and the corresponding portions of the two wakes have very different forms. The wake near the ground spreads horizontally in the cross flow direction more than the other wake. In contrast, near the high points of the trajectories, both wings shed about the same vorticity and the corresponding portions of their wakes have similar forms. The different positions of the wakes signifies that their influence on the flowfields around the tail assemblies in and out of ground effect will be somewhat different. The use of low-aspect-ratio wings makes the difference more noticeable.

In Figures 3.16 and 3.17 the reduced frequency of the oscillation is a rather high $\pi/4$. In both figures, the top and side views are shown. The above argument is also true for these two figures since the reduced frequency is still rather high.

In Figures 3.18 and 3.19 the reduced frequency is $\pi/16$. In Figure 3.18 the wing is flying near the ground. One sees that the effects of the ground are similar to those at the higher frequency, although the changes occur much more slowly. In comparing parts (b) of the two figures, one sees that, although the wakes are depicted at the same points in the trajectories, the wing-tip vortex systems of the wing in ground effect are more widely spread than those of the wing away from the ground, giving the wing in ground effect a greater apparent aspect ratio and a corresponding increase in efficiency.

By comparing Figure 3.16 with Figure 3.18 and Figure 3.17 with Figure 3.19, one can see the effects of changing the frequency in and out of ground effect, respectively. The scale in Figures 3.16 and 3.17 differs from that in Figures 3.18 and 3.19. The horizontal and vertical extents of the wakes for the high-frequency motions are a little greater than their counterparts for the low-frequency motions. The stronger vorticity generated during the faster motion induces a stronger velocity field which causes the wakes to migrate more.

3.5 Conclusion

Recent interest in transoceanic, ground effect airplanes raises the question of what effect the waves would have on their performance. Would the waves enhance or degrade the benefits that can be derived from operating near the surface? As a first attempt to simulate a wing flying over a wavy surface, a small-aspect-ratio and slightly cambered wings oscillating in heave near and far from a flat surface are considered. The mean aerodynamic loads on a wing oscillating in heave at a nominal angle of attack are higher than the corresponding loads on a wing in steady flight at the same angle of attack. This result is true for wings operating both near and far from the ground. The increases are about the same in both cases. Moreover, they grow as the frequency increases, even reaching the point at a rather high frequency where the effects of the oscillation completely dominate those of the ground. Of course, oscillating a wing to augment its aerodynamic performance is not practical, but flying near a wavy surface may well be, and the effects appear to be quite similar. Thus, it is concluded from this preliminary study that flying over a wavy surface probably would enhance the efficiency of a ground-effect craft and be rather beneficial.

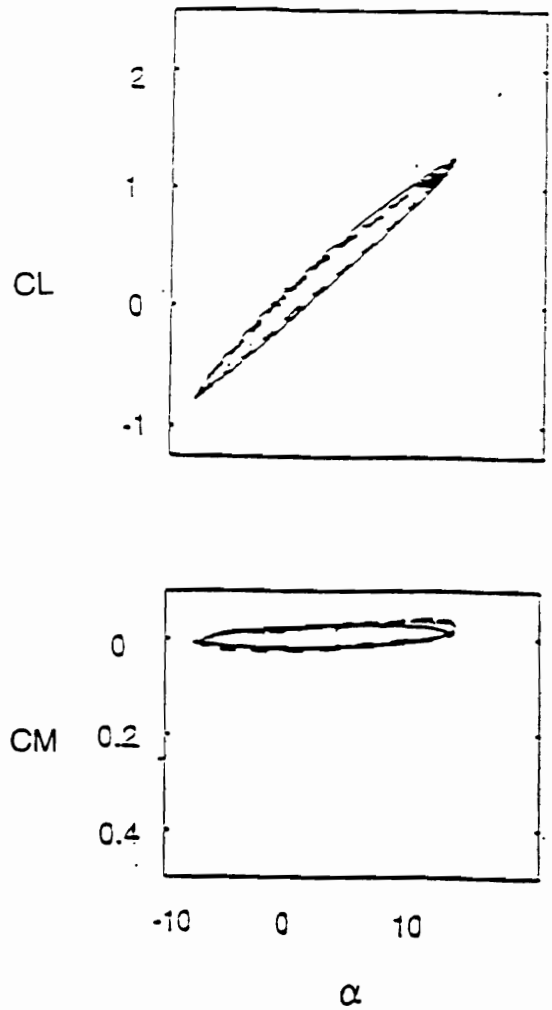

Figure 3.1: Lift and moment coefficients as functions of angle of attack for the NACA 0012 airfoil, $\alpha = 3° + 10° \sin \omega t$, and $k = \omega C/2V_\infty$=0.1. The moment is taken about quarter chord from the leading edge.
— Present solution
- - Experimental data of McCroskey et al.

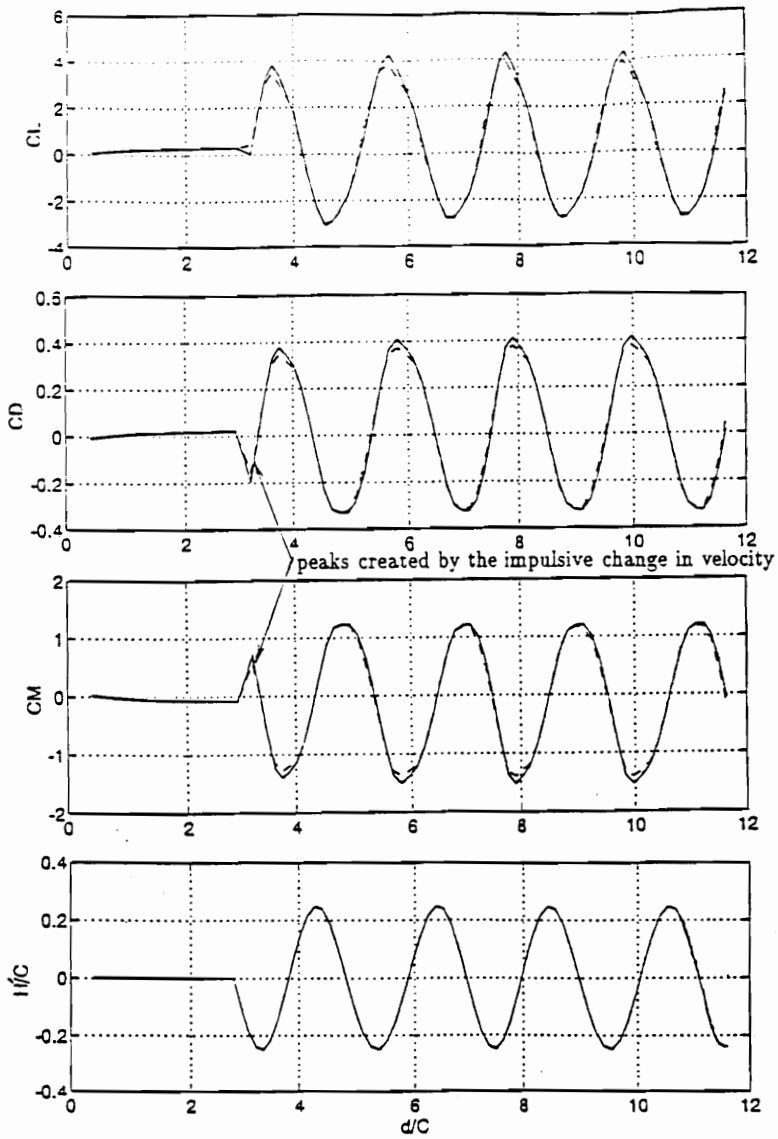

Figure 3.2: Lift, drag, moment, and vertical position of the wing with respect to the mean height above the ground as functions of the distance traveled, d, in terms of chords, C. The moment is taken about the quarter chord from the leading edge, and k=$\pi/2$. — in ground, - - out of ground

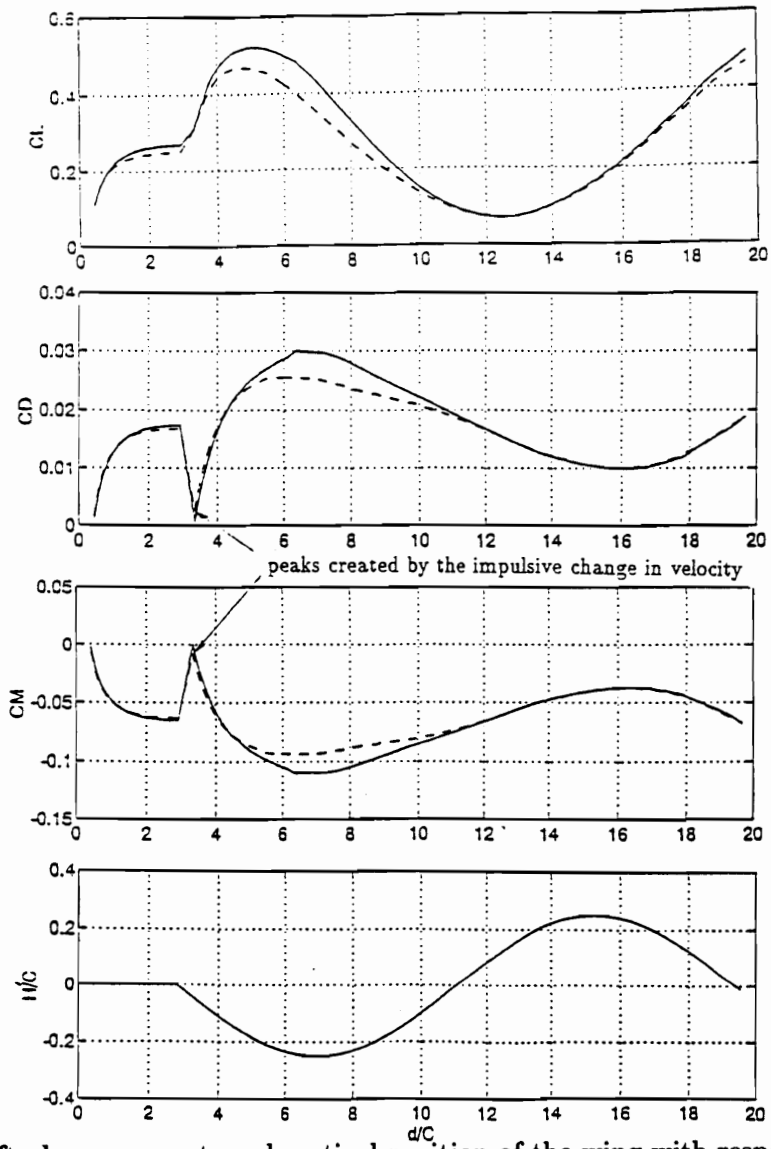

Figure 3.3: Lift, drag, moment, and vertical position of the wing with respect to the mean height above the ground as functions of the distance traveled, d, in terms of chords, C. The moment is taken about the quarter chord from the leading edge, and k=$\pi/16$. — in ground, - - out of ground

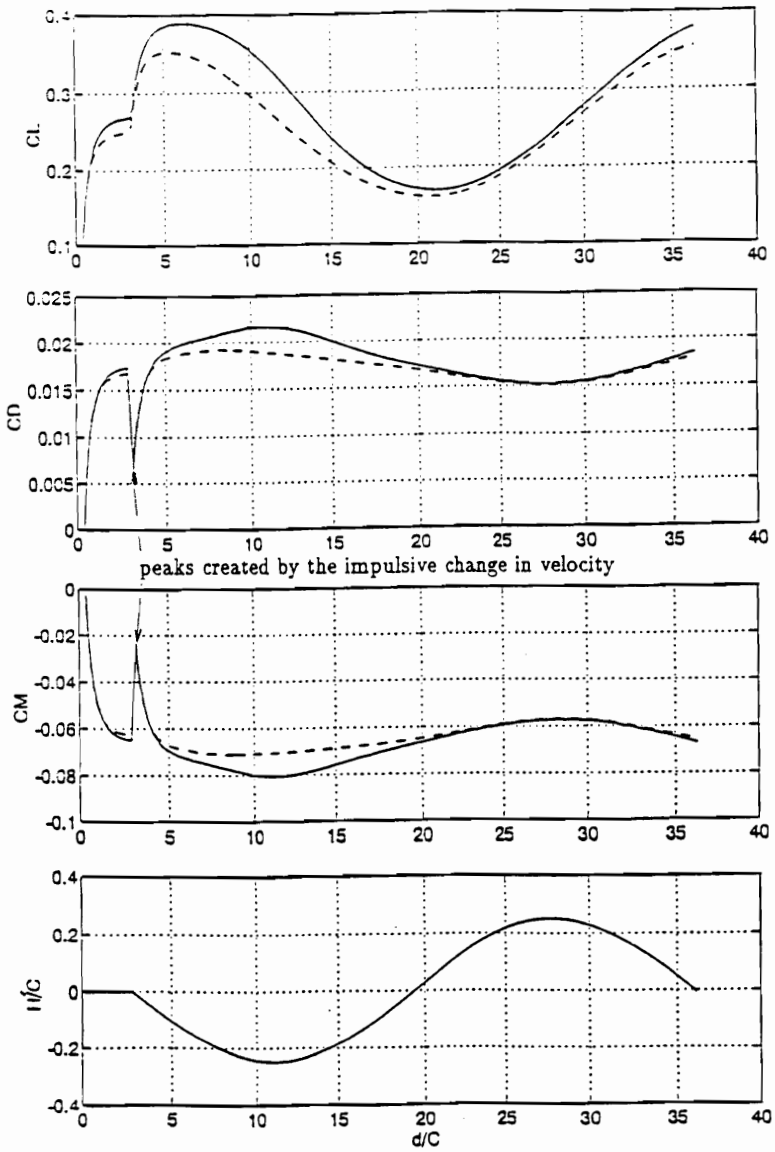

Figure 3.4: Lift, drag, moment, and vertical position of the wing with respect to the mean height above the ground as functions of the distance traveled, d, in terms of chords, C. The moment is taken about the quarter chord from the leading edge, and k=$\pi/32$. — in ground, - - out of ground

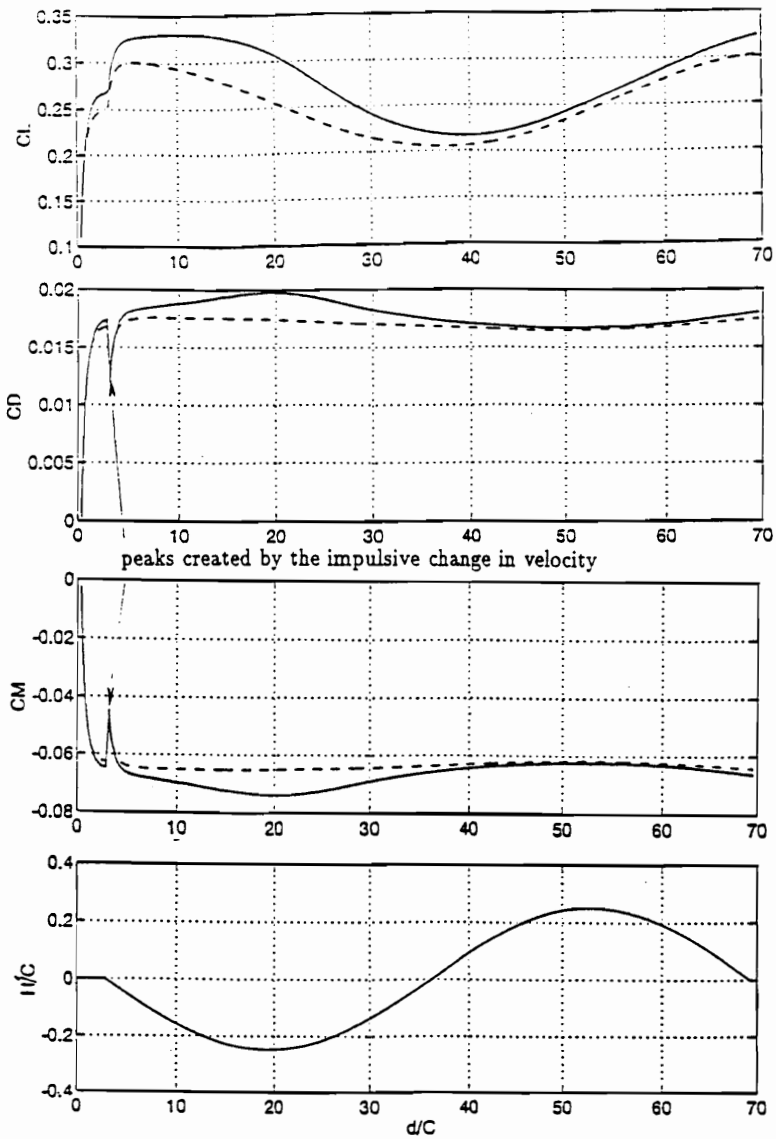

Figure 3.5: Lift, drag, moment, and vertical position of the wing with respect to the mean height above the ground as functions of the distance traveled, d, in terms of chords, C. The moment is taken about the quarter chord from the leading edge, and k=$\pi/64$. — in ground, - - out of ground

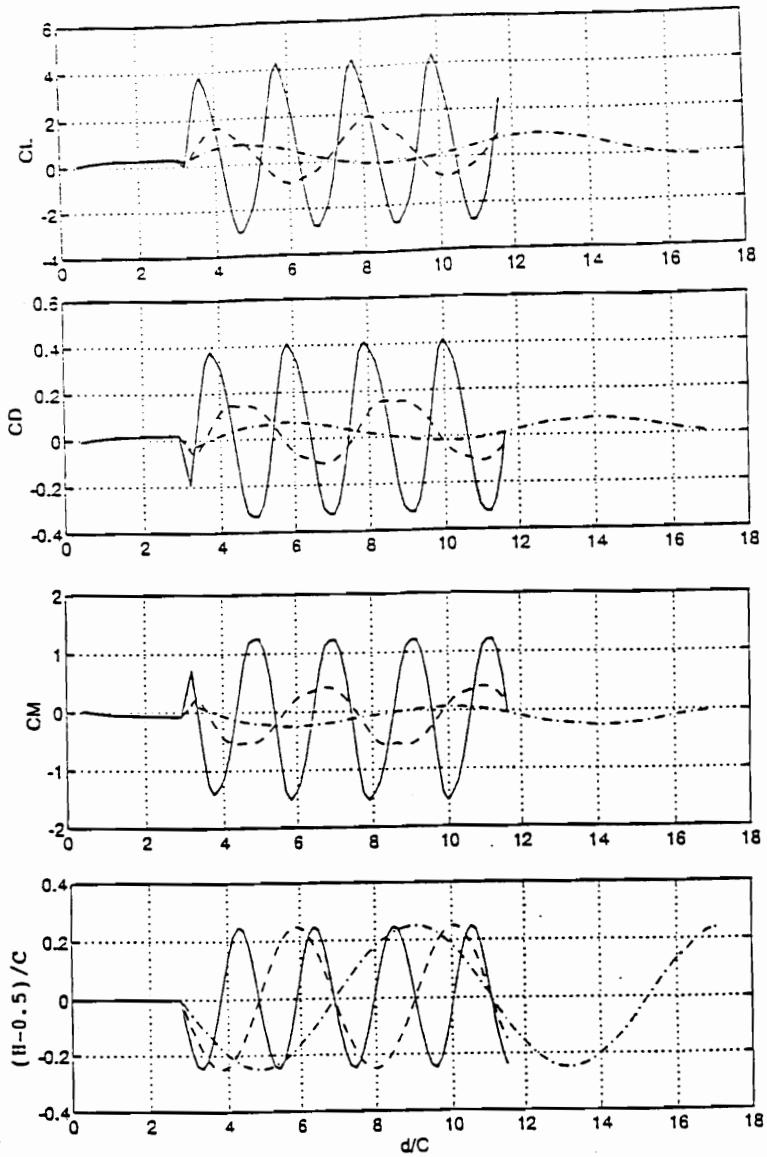

Figure 3.6: Lift, drag, moment, and vertical position of the wing with respect to the mean height above the ground as functions of the distance traveled in chords for a heaving wing in ground effect at three different frequencies. The angle of attack is 3 degrees. — k=$\pi/2$, - - k=$\pi/4$, -.- $k = \pi/8$

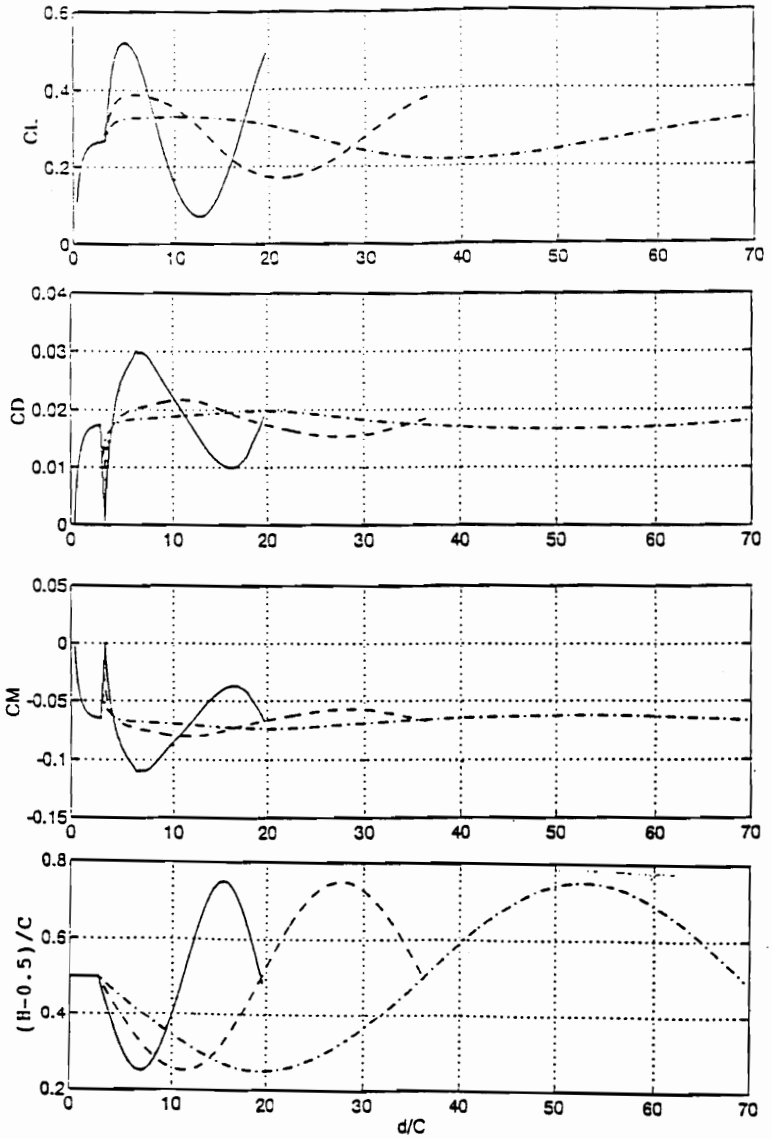

Figure 3.7: Lift, drag, moment, and vertical position of the wing with respect to the mean height above the ground as functions of the distance traveled in chords for a heaving wing in ground effect at three different frequencies. The angle of attack is 3 degrees. — k=$\pi/16$, - - k=$\pi/32$, -.- $k = \pi/64$

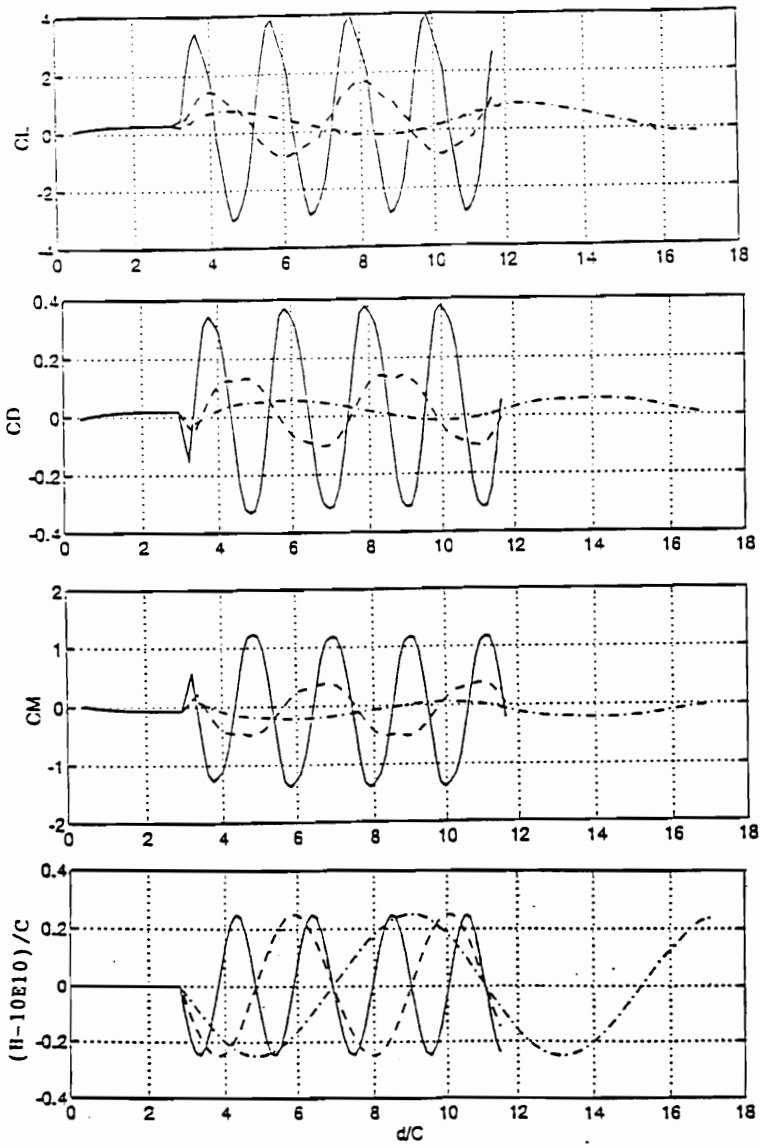

Figure 3.8: Lift, drag, moment, and vertical position of the wing with respect to the mean height above the ground as functions of the distance traveled in chords for a heaving wing out of ground effect at three different frequencies. The angle of attack is 3 degrees. — k=$\pi/2$, - - k=$\pi/4$, -.- $k = \pi/8$

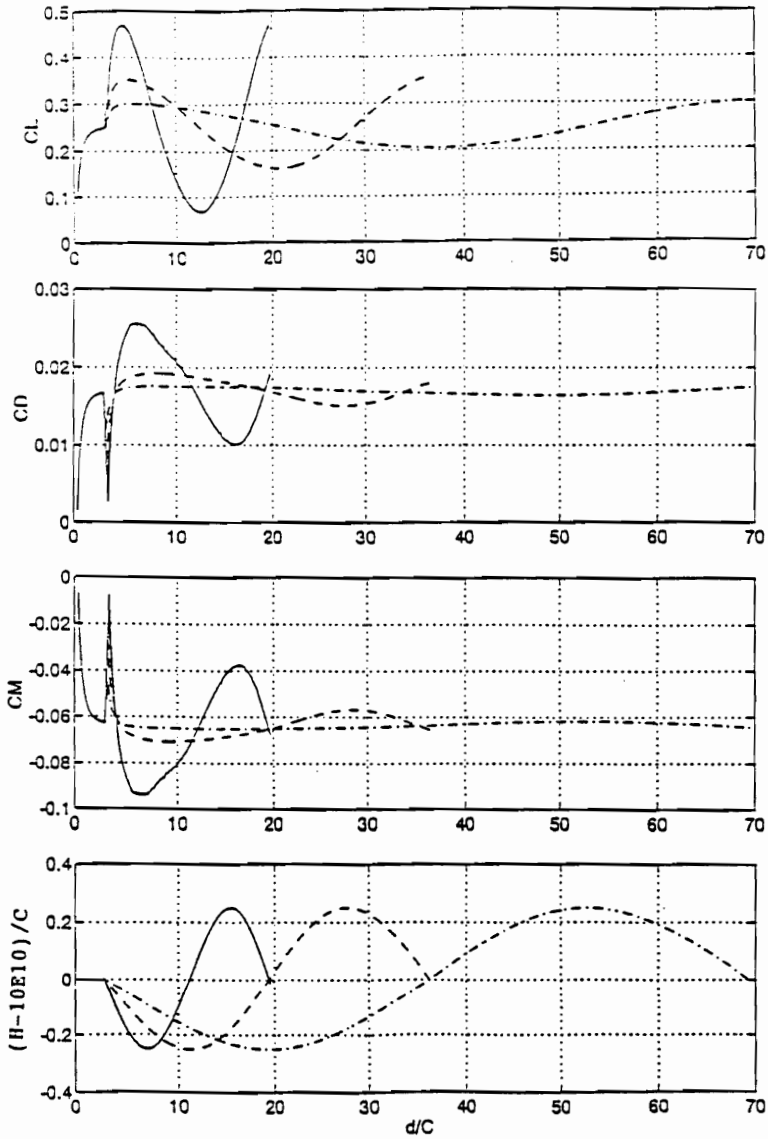

Figure 3.9: Lift, drag, moment, and vertical position of the wing with respect to the mean height above the ground as functions of the distance traveled in chords for a heaving wing out of ground effect at three different frequencies. The angle of attack is 3 degrees. — k=$\pi/16$, - - k=$\pi/32$, -.- $k = \pi/64$

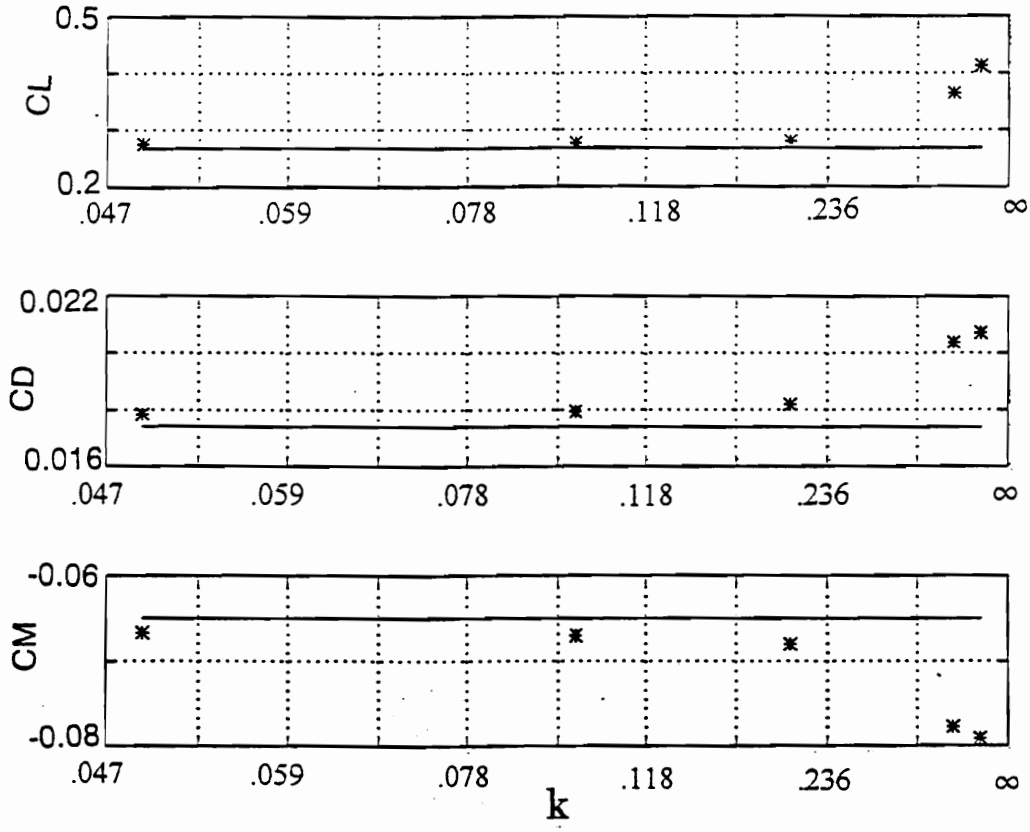

Figure 3.10: Comparison of mean values of lift, drag, and moment coefficients for different periods of oscillation with the steady-state result in ground effect. The mean angle of attack is 3 degrees and h=0.5 chord.
— Steady-state (T= ∞)
* Mean value during the heaving oscillation

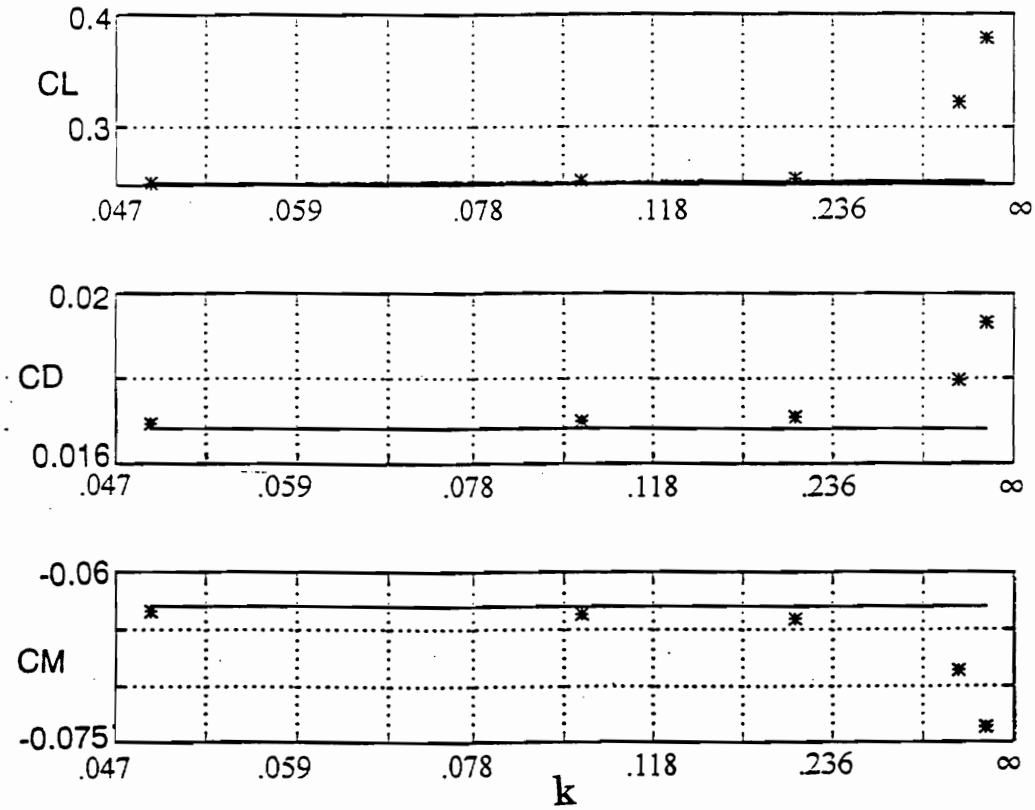

Figure 3.11: Comparison of mean values of lift, drag, and moment coefficients for different periods of oscillation with the steady-state result out of ground effect. The mean angle of attack is 3 degrees.
— Steady-state (T= ∞)
* Mean value during the heaving oscillation

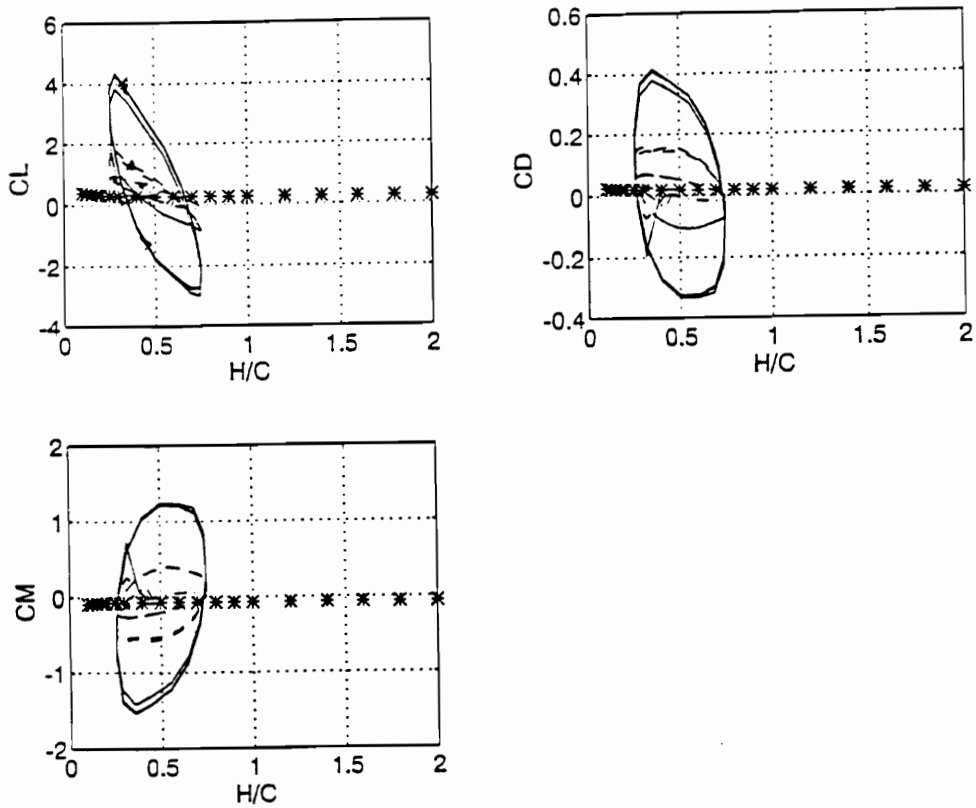

Figure 3.12: Comparison of the unsteady lift, drag, and moment coefficients with the steady-state result. Angle of attack is 3 degrees.
— k=$\pi/2$
- - k=$\pi/4$
-.- k=$\pi/8$
* Steady-state result

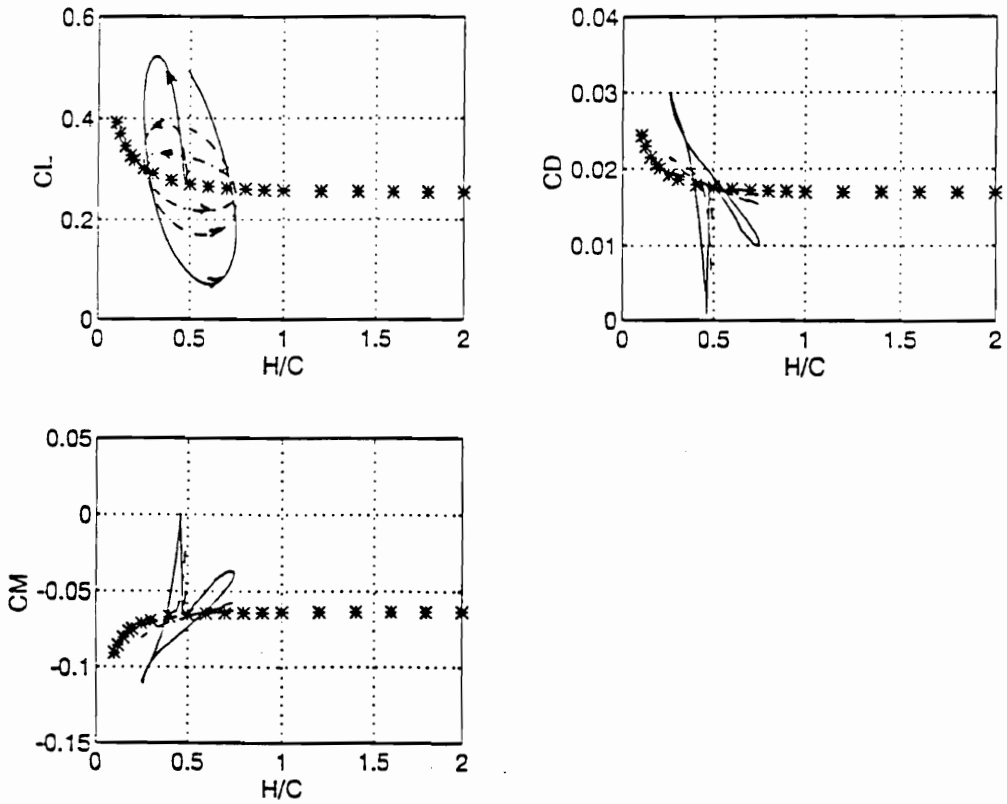

Figure 3.13: Comparison of the unsteady lift, drag, and moment coefficients with the steady-state result. Angle of attack is 3 degrees.
— k=$\pi/16$
- - k=$\pi/32$
-.- k=$\pi/64$
* Steady-state result

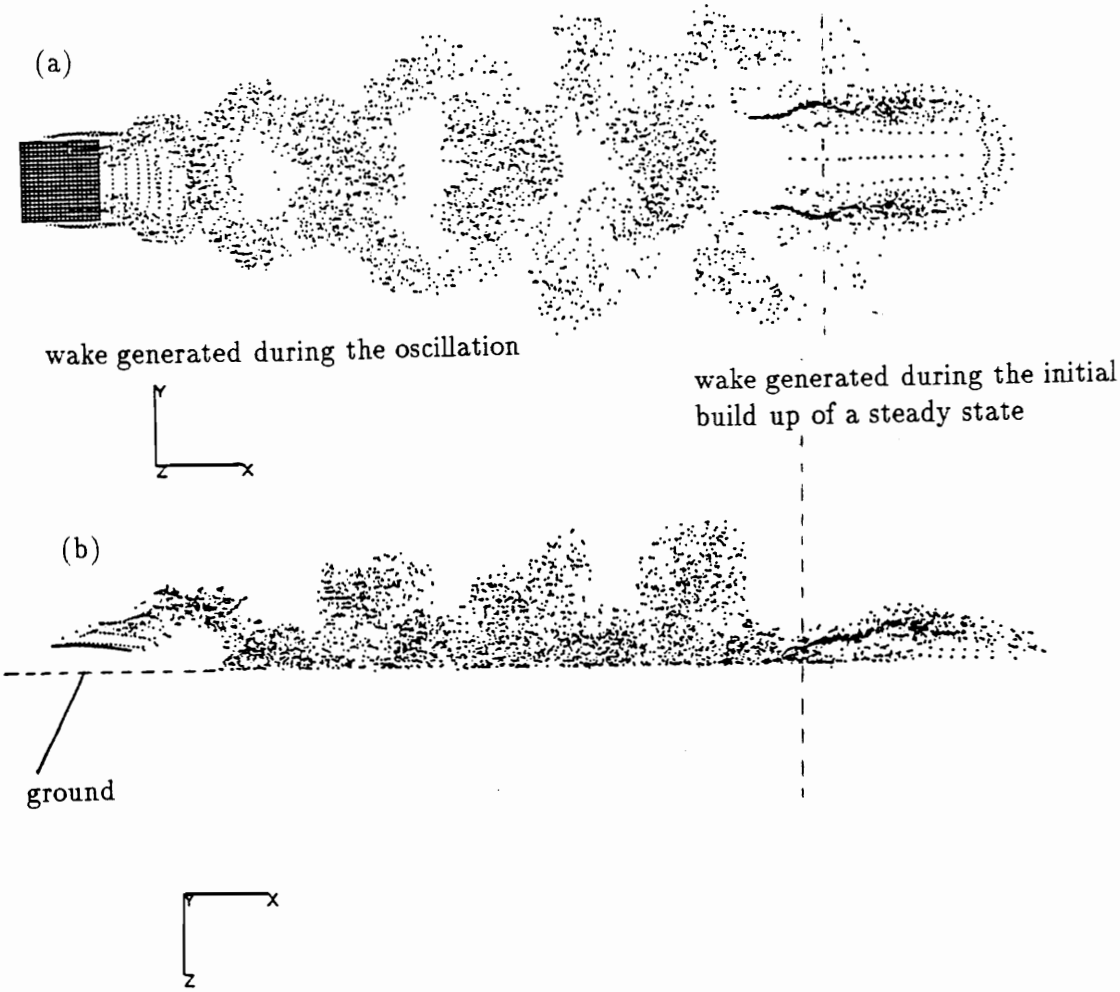

Figure 3.14: Computed wakes for the wing in ground effect where k=$\pi/2$, amplitude=0.25 chord. The dots represent the location of vorticity in the wake of the wing. The portion of the wake generated during the initial start up can be seen at the far right.
(a) Top view
(b) Side view

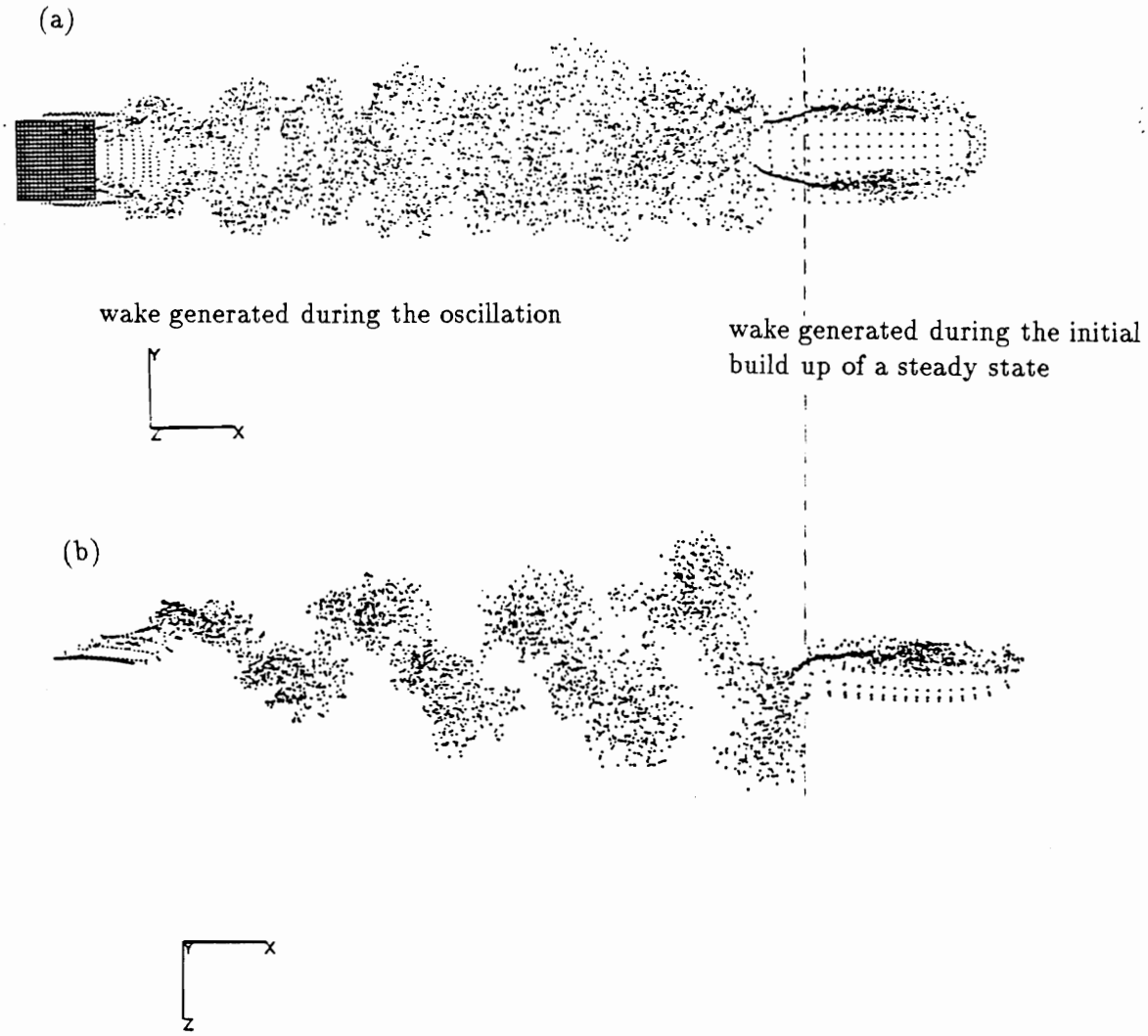

Figure 3.15: Computed wakes for the wing out of ground effect where k=$\pi/2$, amplitude=0.25 chord. The dots represent the location of vorticity in the wake of the wing. The portion of the wake generated during the initial start up can be seen at the far right.
(a) Top view
(b) Side view

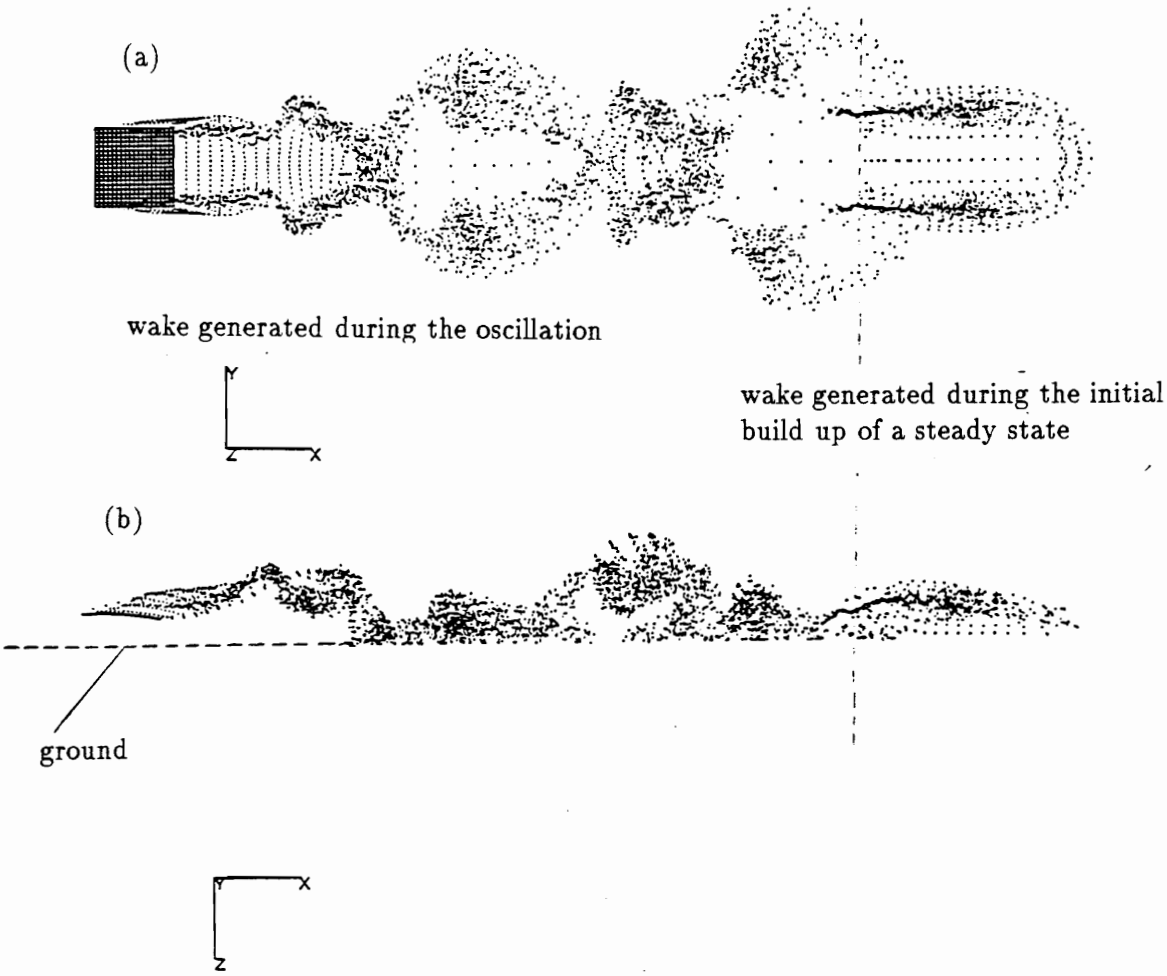

Figure 3.16: Computed wakes for the wing in ground effect where k=$\pi/4$, amplitude=0.25 chord. The dots represent the location of vorticity in the wake of the wing. The portion of the wake generated during the initial start up can be seen at the far right.
(a) Top view
(b) Side view

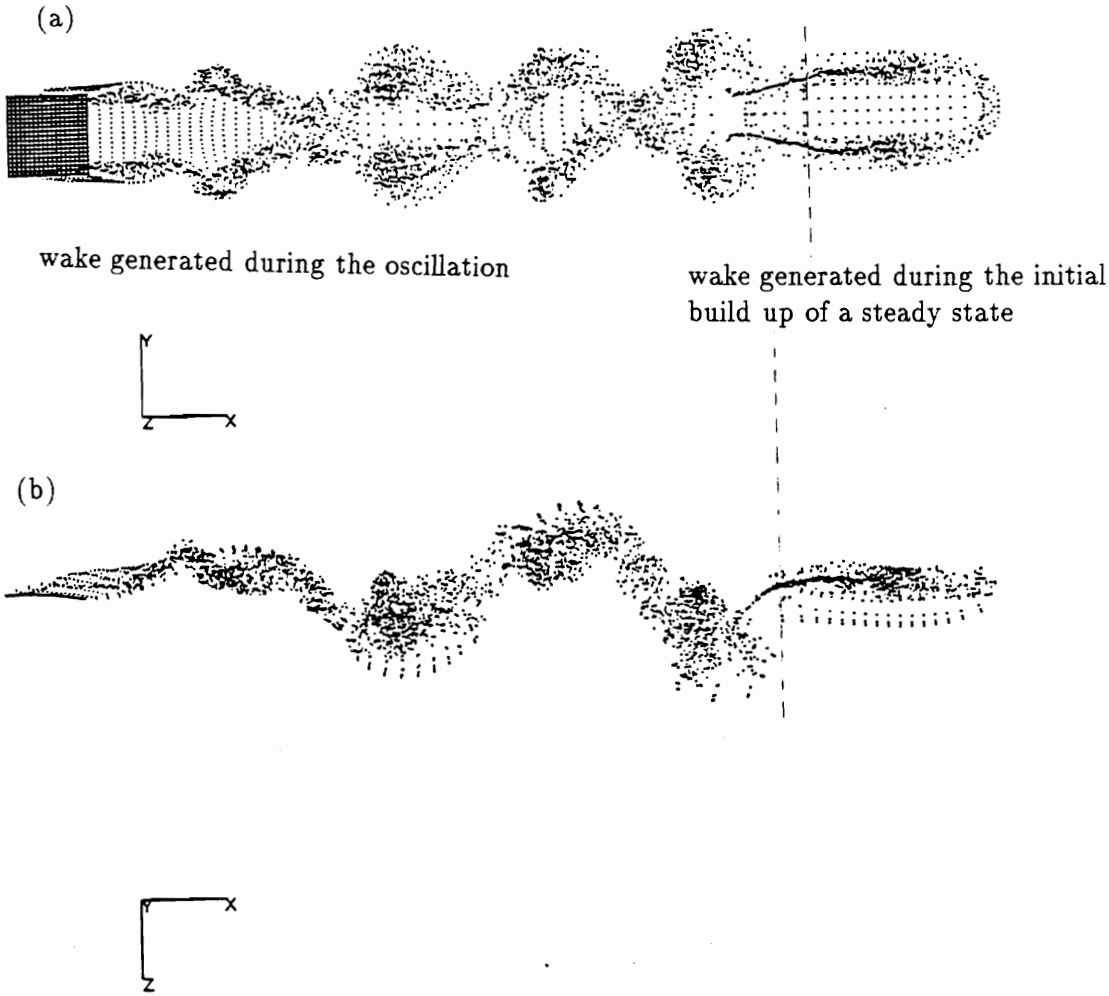

Figure 3.17: Computed wakes for the wing out of ground effect where k=$\pi/4$, amplitude=0.25 chord. The dots represent the location of vorticity in the wake of the wing. The portion of the wake generated during the initial start up can be seen at the far right.
(a) Top view
(b) Side view

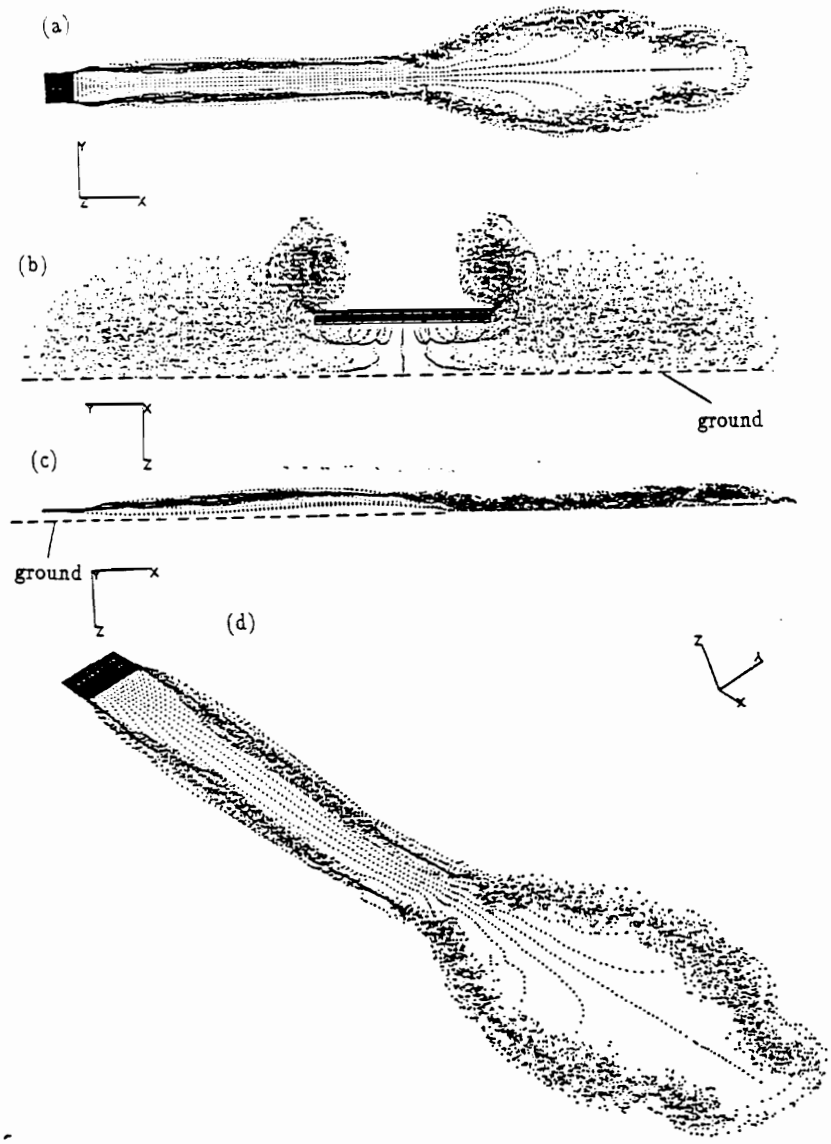

Figure 3.18: Computed wakes for the wing in ground effect k=$\pi/16$, amplitude=0.25 chord. The dots represent the location of vorticity in the wake of the wing. The portion of the wake generated during the initial start up can be seen at the far right.
(a) Top view, (b) Front view, (c) Side view , (d) View from an angle

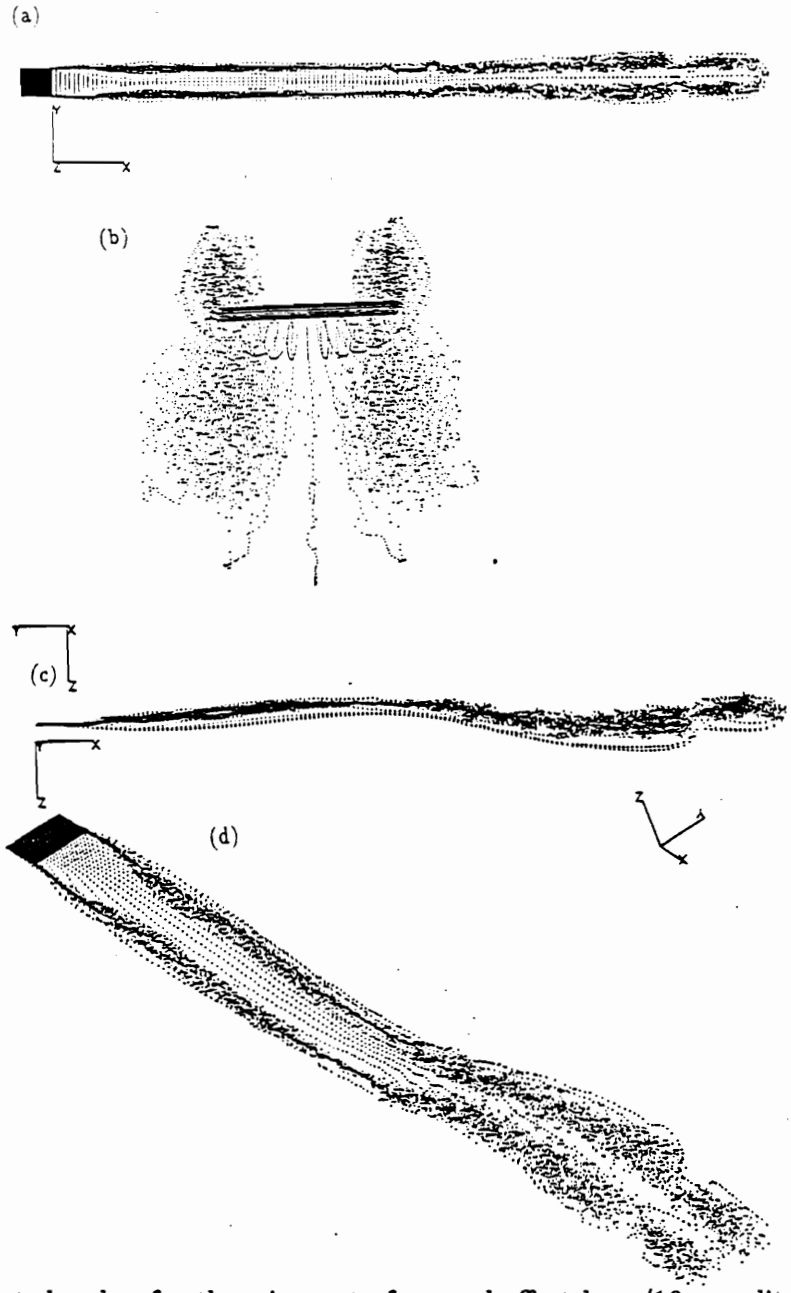

Figure 3.19: Computed wakes for the wing out of ground effect k=$\pi/16$, amplitude=0.25 chord. The dots represent the location of vorticity in the wake of the wing. The portion of the wake generated during the initial start up can be seen at the far right.
(a) Top view, (b) Front view, (c) Side view, (d) View from an angle

Chapter 4

THICK-WING IN STEADY AND UNSTEADY FLOWFIELD

4.1 Introduction

In this chapter the effect of thickness and Reynolds number on the aerodynamic lift and moment is investigated. The general, unsteady, three-dimensional, vortex-lattice method (UVLM) is evaluated by making a number of comparisons between numerical results obtained from UVLM and experimental results. Both thick-wing and lifting-surface versions of UVLM are used. The interest is in future applications of UVLM to numerical simulations of the interactions among aerodynamics, rigid-body and structural dynamics, and mechanisms that drive control surfaces. One can often realize substantial reductions in computational time by using a lifting-surface approximation instead of a thick-wing model. The most important questions are, when is such an approximation appropriate and what is the effect of the Reynolds number on the aerodynamic load? This chapter attempts to answer these questions.

4.2 Description of The Problem

In this chapter, rectangular wings of very high aspect ratio are considered. The aspect ratio is 30. To investigate the effect of thickness, the method is applied to wings with thicknesses ranging from 0% to 27%. This is done for NACA airfoils with no camber, 00XX. In order to study the effect of thickness on a cambered airfoil, NACA airfoils of 44XX with thicknesses ranging from 0% to 27% are considered.

Steady results are computed from the UVLM by giving the wing an impulsive start and then having it move at constant velocity until the steady state develops. Then the results from the mid-span of the wing are compared with the experimental data. The results for a wing in oscillation are obtained by first reaching the steady state and then having the wing oscillate.

4.3 Results

4.3.1 Effect of Reynolds Number

In Figure 4.1 the numerical results are compared with experimental data for various chord-based Reynolds numbers. The wing in the experiment was a symmetric NACA 0009 and the results were computed for a flat plate. The computed lift coefficients are in good agreement with the experimental data up to an angle of attack of 8 degrees and moment coefficients 10 degrees. The agreement improves as the Reynolds number increases. It should be noted that the Reynolds numbers here are low for most aerodynamic applications. The numerical results correspond to the infinite Reynolds number approximation. The present computational results for a flat plate were compared with the experimental data of the NACA 0009 for higher Reynolds numbers. In Figure 4.2 there is good agreement up to separation.

In Figure 4.3 the numerical results are compared with experimental data for a cambered airfoil. The numerical results were obtained from a lifting surface lying on the camber

surface of the actual airfoil. Again, the results are in good agreement for lower values of the angle of attack. The difference between the experimental data starts before separation occurs. The comparison of the present results with the experimental data should improve as the Reynolds number increases. Figure 4.4 compares the experimental data of a NACA 4409 with the numerical data obtained using a NACA 4400. Again, they are in good agreement until the separation occurs.

4.3.2 Thickness Effect

Steady Flowfield

In Figure 4.5 the numerical results for a flat plate are compared with the experimental data for several symmetric airfoils of different thicknesses. The lift coefficients are in good agreement even at 18% thickness, but there is some noticeable difference in the moment coefficient for angles of attack above 10 degrees. In Figure 4.6, the numerical results for a cambered airfoil with no thickness are compared with the experimental data for several airfoils with different thickness. Again, the lift coefficients are in good agreement even at 15% thickness, but there is some noticeable difference in the moment coefficient for angles of attack above 10 degrees. The results show that a thick wing can be replaced by a lifting surface lying on the camber surface of the actual airfoil.

To further analyze the effect of thickness on aerodynamic loads, the numerical results for symmetric airfoils of different thicknesses are shown in Figure 4.7. The agreement of the present results with the experimental data for NACA 0015 is excellent. As the thickness of the wing increases, the lift coefficient increases. It should be noted that this difference in the lift coefficient increases with the angle of attack. Figure 4.8 compares the numerical result with the experimental data for a cambered airfoil, NACA 4415. The agreement is good, and better agreement is expected as the value of Reynolds number increases. Furthermore, the effect of thickness is to enhance the lift.

Oscillating Wing

The method was used to calculate the loads on a NACA 0012 profile with an aspect ratio of 30 oscillating sinusoidally in pitch about the quarter chord.

In Chapter 3 the mid-span aerodynamic load of the numerical results was compared with the experimental data of McCroskey et al. It was shown that the present solution agrees well with the data.

To investigate the effect of the thickness of a wing in oscillation, the numerical results for various thicknesses are presented in Figure 4.9. In this example, the mean angle of attack is 3 degrees, the time step is 0.055, and the amplitude of the oscillation is 10 degrees. The reduced frequency, defined as $k = \omega C/2V_\infty$, is 0.1. The predicted lift is slightly affected by the thickness; the predicted moment is much more sensitive to the thickness. But to illustrate this phenomenon it was necessary to go as high as 27% thickness. The widening of the hysteresis loops indicates that the thick profile will dissipate more energy during a cycle.

4.4 Conclusion

A thick airfoil can be replaced by a lifting surface lying on the camber surface of the actual airfoil. A wing as thick as 18% can be replaced by a lifting surface. For high values of Reynolds number, the thin-wing solution agrees well with the experimental data up to the point where separation occurs. As the Reynolds number decreases, the agreement breaks from higher angle of attack.

The vortex-lattice method can predict the aerodynamic load on a thick-wing in oscillation. Lift and moment coefficients are affected by the thickness of a wing in oscillation. The moment is more sensitive to the thickness than the lift. A thick profile would dissipate more energy during a cycle.

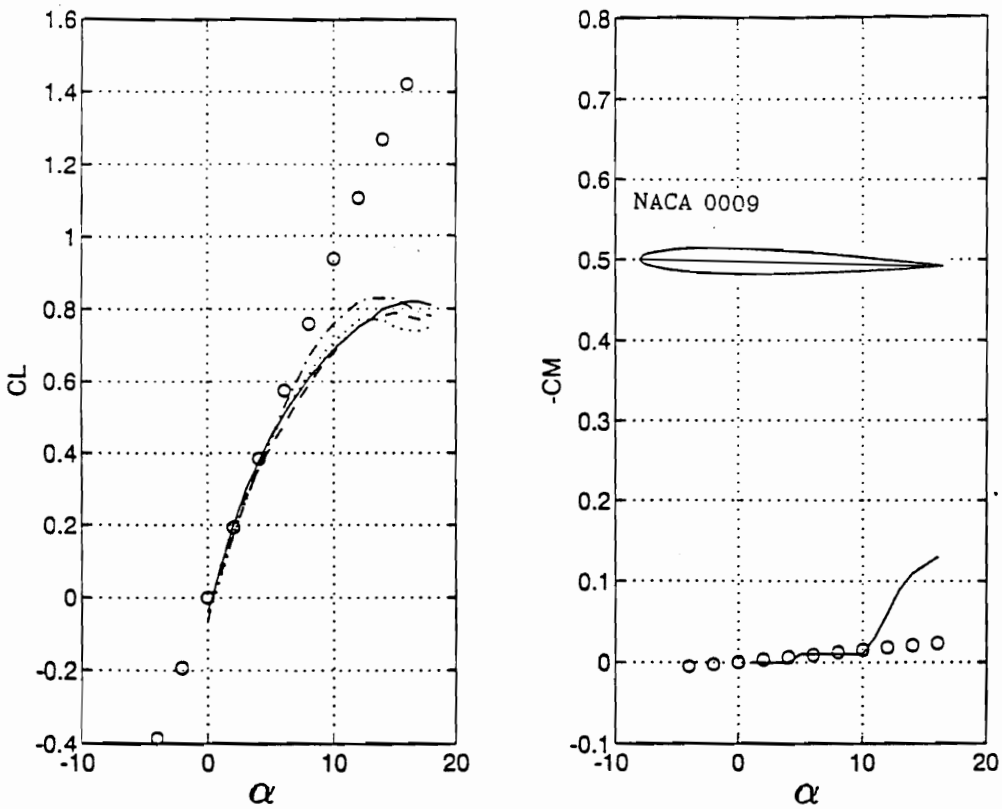

Figure 4.1: Experimental and numerical lift and moment as functions of the angle of attack for the NACA 0009 airfoil.
Experimental Data (Miley, 1982):

Reynolds number	Test conditions
$4.2 * 10^4$	Tunnel: NACA VDT
$8.4 * 10^4$ - - -	Date: 1937
$1.7 * 10^5$ ——	Test: 3-D
$3.3 * 10^5$ -.-.-	Turbulence: 2.0 %
	Surface: Smooth

o Present solution for the flat plate, aspect ratio=30

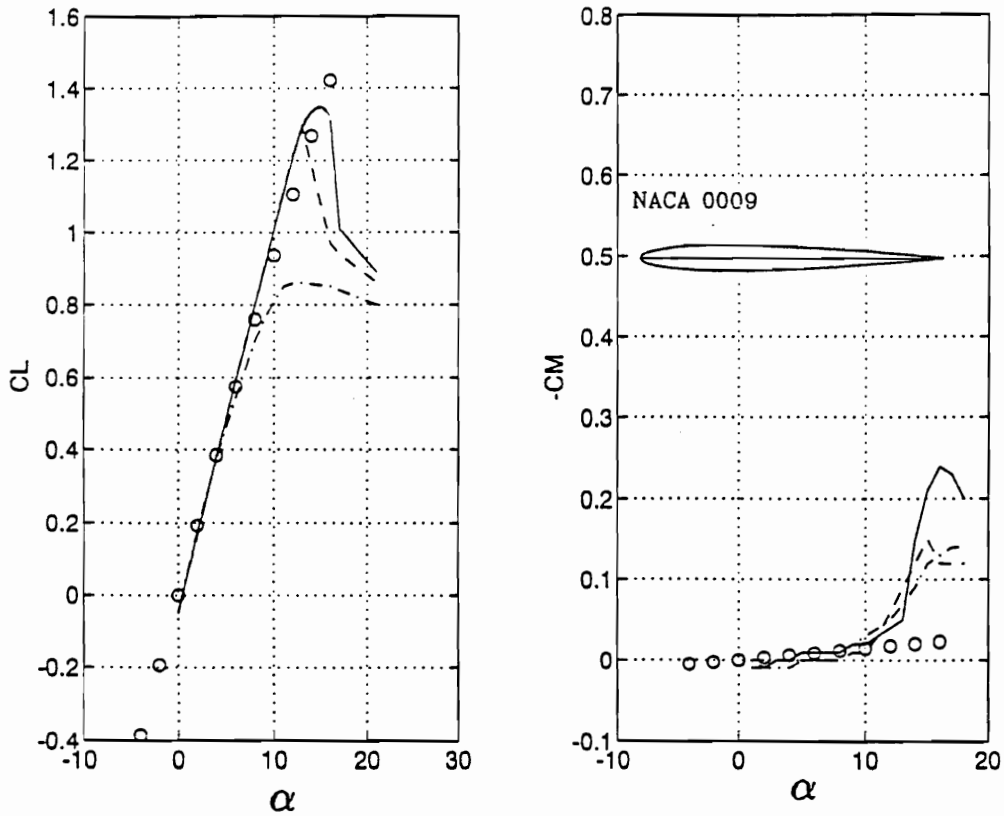

Figure 4.2: Experimental and numerical lift and moment as functions of the angle of attack for the NACA 0009 airfoil.
Experimental Data (Miley, 1982):

Reynolds number	Test conditions
$6.7 * 10^5$ -.-.-	Tunnel: NACA VDT
$1.3 * 10^6$ - - -	Date: 1937
$2.3 * 10^6$ ——	Test: 3-D
	Turbulence: 2.0 %
	Surface: Smooth

o Present solution for the flat plate, aspect ratio=30

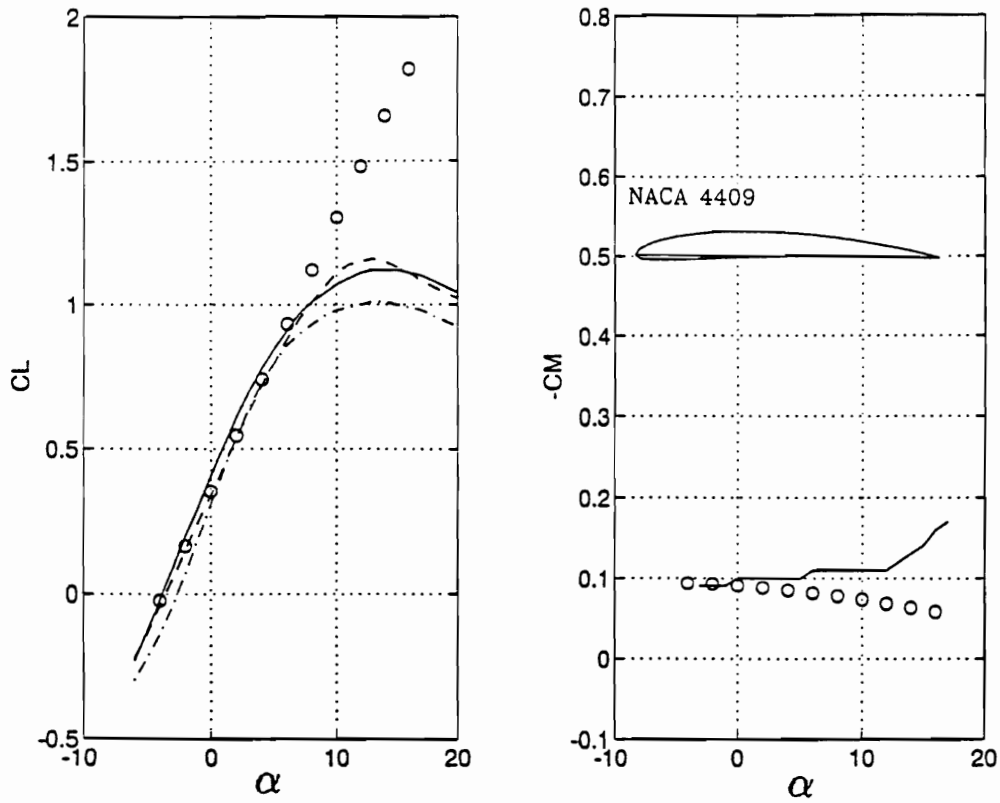

Figure 4.3: Experimental and numerical lift and moment as functions of the angle of attack for the NACA 4409 airfoil.

Experimental Data (Miley, 1982):

Reynolds number	Test conditions
$4.2 * 10^4$ -.-.-	Tunnel: NACA VDT
$8.3 * 10^4$ - - -	Date: 1937
$1.7 * 10^5$ ——	Test: 3-D
	Turbulence: 2.0 %
	Surface: Smooth

o Present solution for the NACA 4400 lifting surface, aspect ratio=30

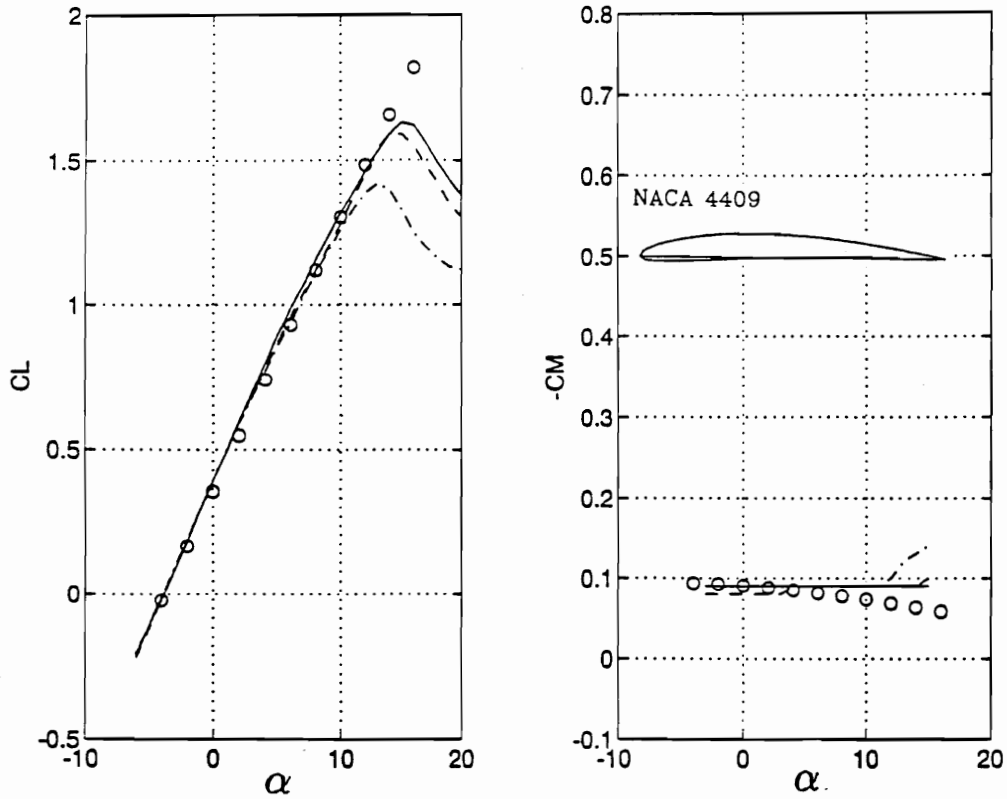

Figure 4.4: Experimental and numerical lift and moment as functions of the angle of attack for the NACA 4409 airfoil.

Experimental Data (Miley, 1982):

Reynolds number	Test conditions
$2.7 * 10^5$ -.-.-	Tunnel: NACA VDT
$2.3 * 10^6$ - - -	Date: 1937
$3.1 * 10^6$ ——	Test: 3-D
	Turbulence: 2.0 %
	Surface: Smooth

o Present solution for the NACA 4400 lifting surface, aspect ratio=30

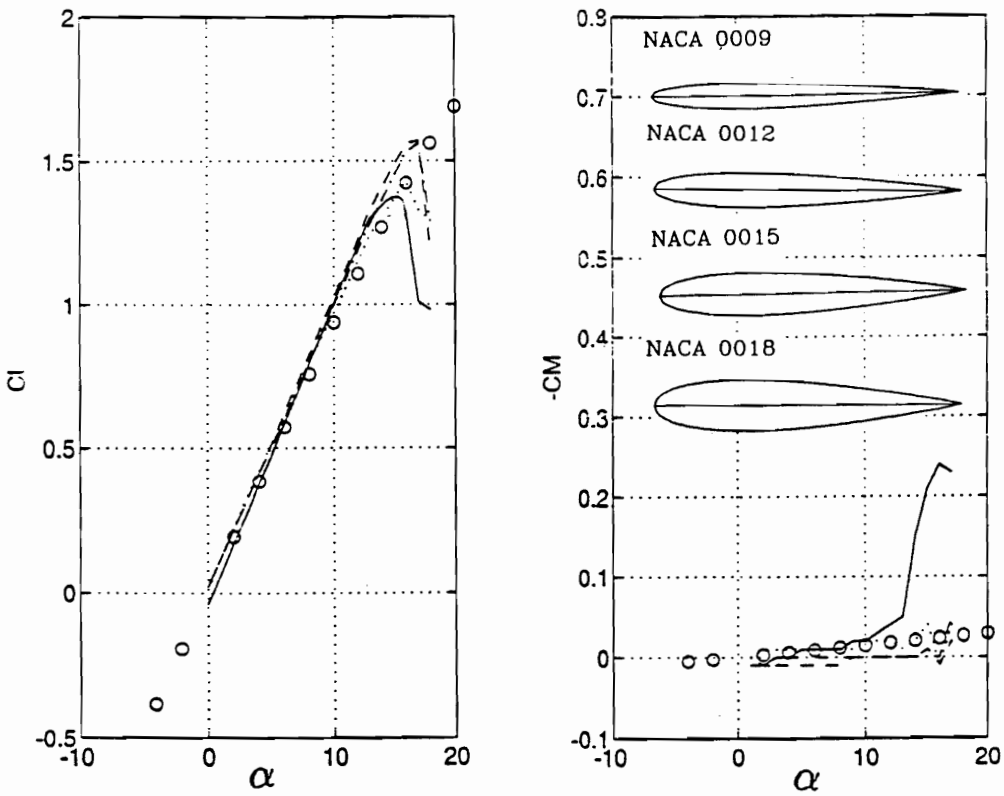

Figure 4.5: Experimental and numerical lift and moment as functions of the angle of attack for symmetric NACA 00xx airfoil of different thicknesses.

Experimental Data (Miley, 1982):

NACA Airfoil	Reynolds number	Test conditions
0009	$2.3 * 10^6$ ——	Tunnel: NACA VDT
0012	$3.2 * 10^6$ - - -	Date: 1937
0015	$3.3 * 10^6$ -.-.-	Test: 3-D
0018	$3.0 * 10^6$	
		Turbulence: 2.0 %
		Surface: Smooth

o Present solution for a flat plate, aspect ratio=30

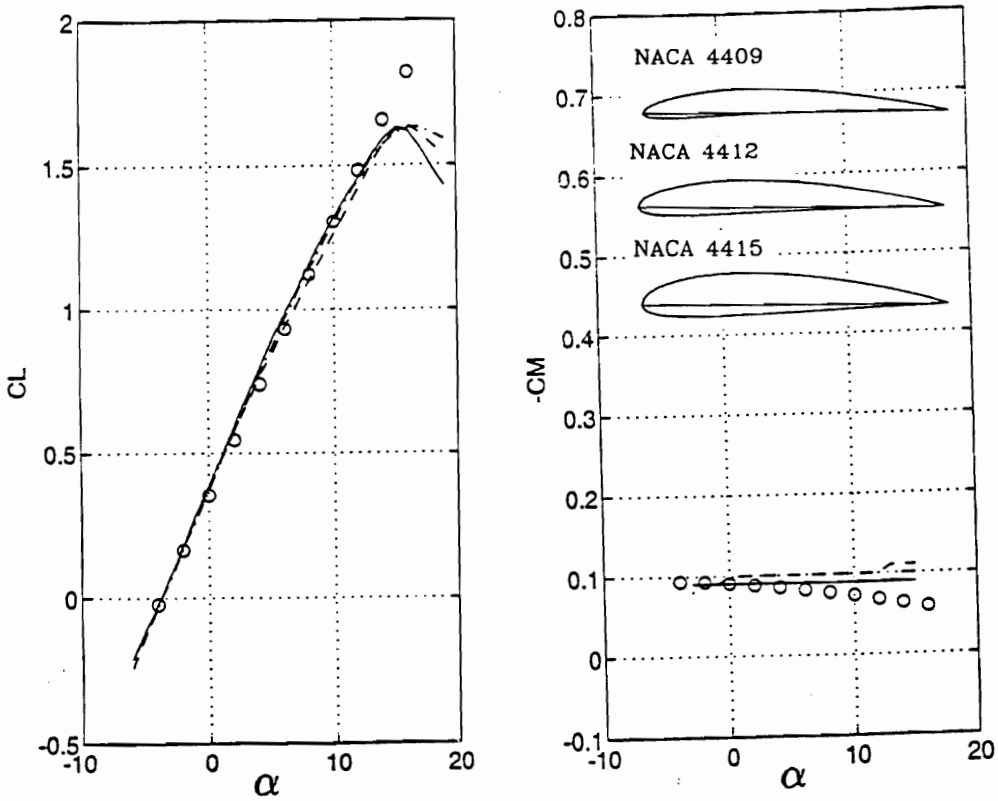

Figure 4.6: Experimental and numerical lift and moment as functions of the angle of attack for symmetric NACA 44xx airfoil of different thicknesses.
Experimental Data (Miley, 1982):

NACA Airfoil	Reynolds number	Test conditions
4409	$3.1 * 10^6$ ——	Tunnel: NACA VDT
4412	$3.0 * 10^6$ - - -	Date: 1937
4415	$3.0 * 10^6$ -.-.-	Test: 3-D
		Turbulence: 2.0 %
		Surface: Smooth

o Present solution for the 4400, aspect ratio=30

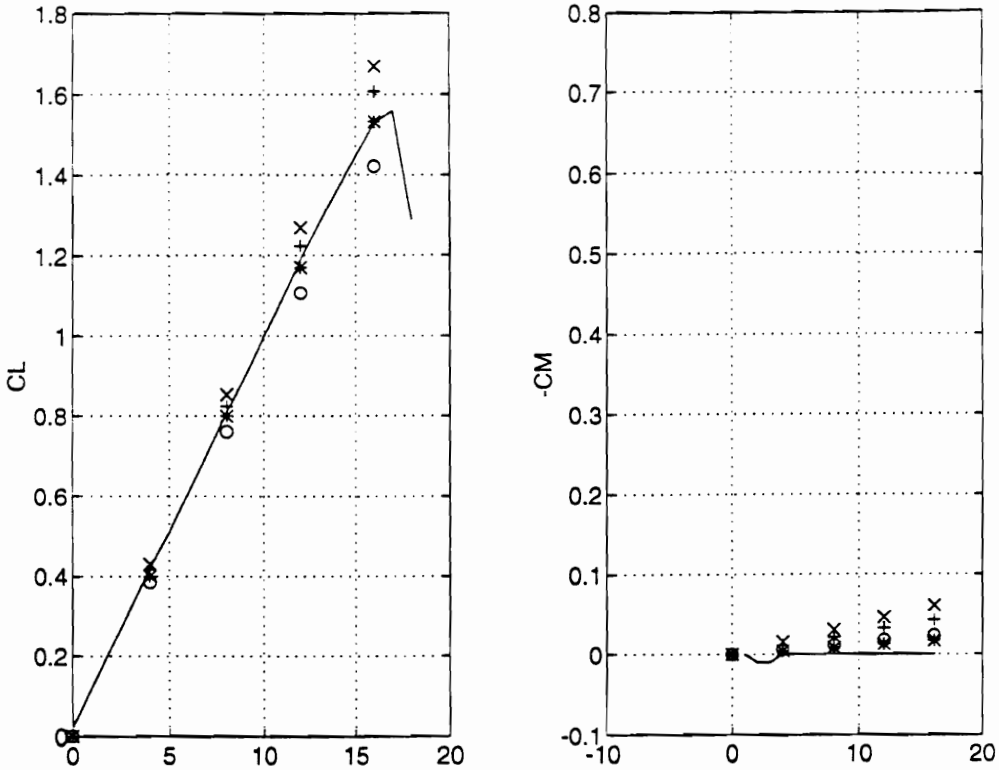

Figure 4.7: Lift and moment as functions of the angle of attack for uncambered airfoils of different thicknesses.
Experimental Data (Miley, 1982):
NACA Airfoil Reynolds number
0015 $3.3 * 10^6$ — Tunnel: NACA VDT
o Lattice method applied to 0000
* Lattice method applied to 0015
+ Lattice method applied to 0021
x Lattice method applied to 0027

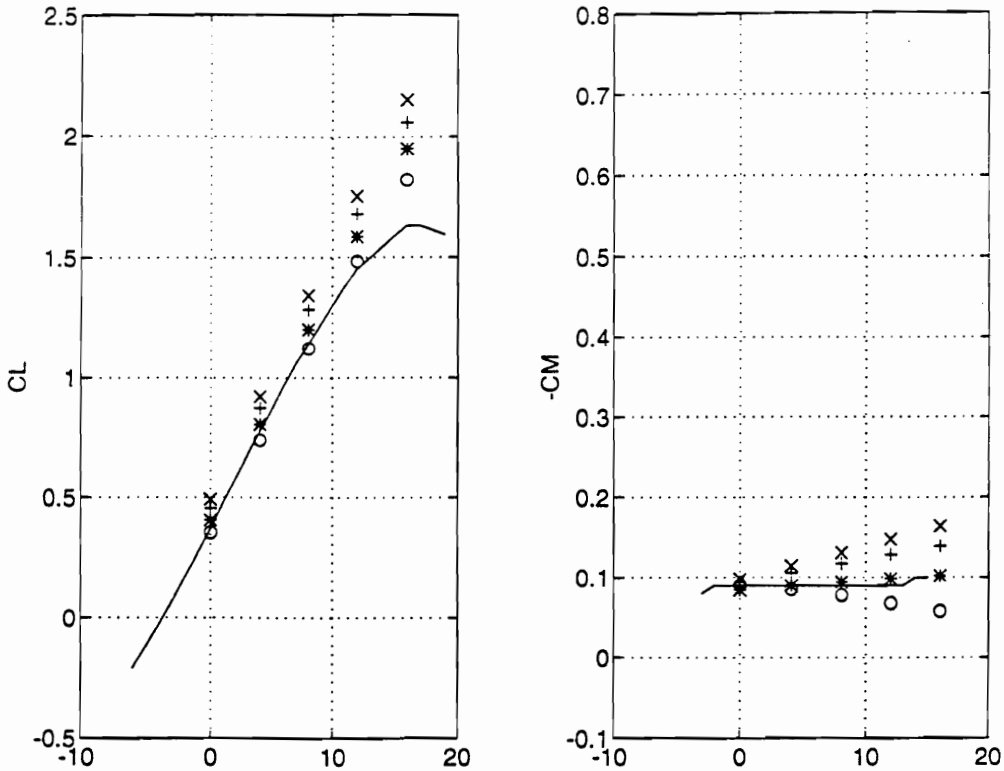

Figure 4.8: Lift and moment as functions of the angle of attack for cambered airfoils of different thicknesses.
Experimental Data (Miley, 1982):
NACA Airfoil Reynolds number
4415 $3.0 * 10^6$ — Tunnel: NACA VDT
o Lattice method applied to 4400
* Lattice method applied to 4415
+ Lattice method applied to 4421
x Lattice method applied to 4427

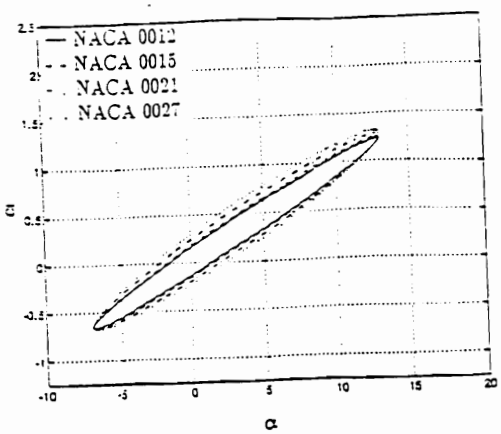

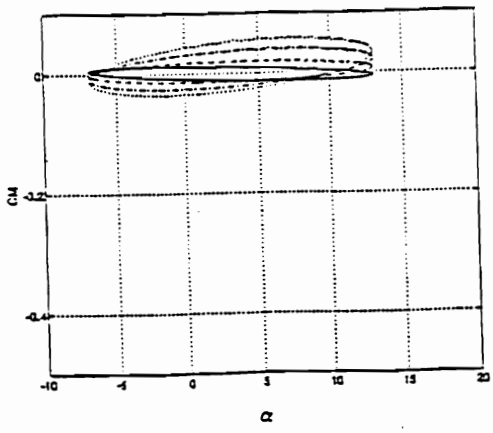

Figure 4.9: Calculated lift and moment coefficients as functions of the angle of attack for wings of different thicknesses, $\alpha = 3° + 10° \sin \omega t$, and k=.1. The moment is taken about quarter chord from the leading edge.
— NACA 0012
- - NACA 0015
- . NACA 0021
. . NACA 0027

Chapter 5

TRAILING VORTICES AND THEIR EFFECTS

5.1 Introduction

The vorticity shed along the edges of a wing forms the wake of the wing. The vorticity shed from the wing-tip is relatively strong and evolves into a region of concentrated vorticity known as the wing-tip vortex. These wing-tip vortices are the counter-rotating cylindrical air masses that trail behind every airplane. Their strength depends mainly on the weight of the aircraft. Other planes flying too close behind can get caught up in the rotating swirl, with devastating consequences.

In one example of an accident, which occurred in Japan, a Cessna airplane crashed and burned at Nagoya Airport (Ogawa, 1993). The investigators concluded that the wing-tip vortex of Boeing 727, which was produced at the tip of the wing, was responsible.

Time magazine in its October 1994 issue reported that the safety board issued a warning about strong wing-tip vortices, concentrating on the turbulence generated by the heavier Boeing 757, whose wake has upset or downed seven other planes. Among them is a 737.

In this chapter the aerodynamic loads acting on one wing operating near the wake of

another are modeled for various positions of the trailing wing relative to the leading wing.

5.2 Description of The Problem

The trailing vortex behaves much like the wake of a ship: the heavier the vessel's displacement weight, the more violent and lasting the disturbance. The trailing vortex of a heavy airplane can have a dangerously strong affect on a lighter aircraft. A typical heavy aircraft, a Boeing 757 is considered to be the leading aircraft and a typical light aircraft, the Cessna 750 Citation X to be the trailing aircraft.

Within crowded airspace, such as an airport, is the most likely place where one aircraft may fly near the wake of another. Therefore, the conditions for a plane that is in the landing pattern are of interest. The velocity of the aircraft is approximately 114 m/s (221 Knots) and the density of the air is 1.2 kg/m^3. At such a speed both the wings are modified by the deployment of flaps, which are not taken into account in the present aerodynamic model. Though the present model could account for flaps, sufficient information to do so was not available. The present example illustrate the potential of the method and the type of results that can be produced.

The Boeing 757 has an average landing weight of 80,000 Kg and wing area of 185 m^2. The Cessna 750 Citation X has an average landing weight of 12000 Kg and wing area of 42 m^2. The coefficient of lift is given by $C_L = \frac{L}{1/2\rho V_\infty^2 S}$, where L is the lift, ρ is the density of air, V_∞ is the free-stream velocity, and S is the area of the wing. This equation is used to calculate the lift coefficients for the Cessna 750 and the Boeing 757, which are 0.36 and 0.54, respectively. Figure 5.1 shows that 7 degrees angle of attack approximately produces the required lift coefficient for the Boeing 757. Figure 5.3 shows that approximately 5 degrees angle of attack for the Cessna 750 produces the required lift coefficient. Therefore, in the present illustration the effect of the trailing vortex from the wing of a Boeing 757 with 7 degrees angle of attack on the wing of a Cessna 750 with 5 degrees angle of attack is investigated.

5.3 Numerical Results

In Figure 5.1 the planform of the wing of a Boeing 757, hereafter called wing B, used in the present study and the calculated lift, drag, and moment coefficients as functions of angle of attack are shown. In Figure 5.2 the computed wake behind the wing for an angle of attack of 7 degrees is shown. The wing-tip vortex systems curl as one would expect. In this figure the cross-stream curling of vortices due to the impulsive start is far downstream and not shown; the wake was cut after the wing had traveled approximately four chords. The contribution of the segments of the wake far downstream is not significant, and by cutting the wake computational time is saved. In Figure 5.3 the profile of the wing of a Cessna 750, hereafter called wing C, and the calculated aerodynamic loads are shown. Figure 5.4 shows the calculated wake for wing C with 5 degrees angle of attack. Again, the cross-stream curling of vortices due to impulsive start is far downstream and not shown. The wake was cut after the wing had traveled approximately eight chords.

Both wings are set in motion with an impulsive start and then moved at constant velocity until the steady-state develops. Wing B is located far from the wing C (more than 20 chords, longitudinally). The wake of wing B far from the wing is affected by the presence of wing C and its wake. By neglecting wing B in the calculation after the steady-state develops, computational time is saved without affecting the accuracy of the results. Wing C moves at a constant velocity until it passes the wake of wing B and the steady-state develops. The effects of the wake from wing B on the wing C are investigated when wing C is in different positions relative to wing B (transversely and vertically). The position of wing C relative to wing B is measured by fixing a coordinate system to the mid-span of wing B.

In Figure 5.5 the calculated lift, drag, and moment coefficients of wing C are shown as functions of the vertical distance from wing B. The moment is taken about the trailing edge at the mid-span, which is not far from the center of mass, and has been nondimensionalized with respect to the root chord of wing C. As the vertical distance between the two wings decreases, the aerodynamic load decreases due to the effect of the wake of wing B. As the

vertical distance between the two wings increases, the effect of wing B reduces. Wing C is most influenced by wing B when the vertical distance between them is zero. Where the two wings are distanced (vertically) about 10 chords, the influence is very small.

In Figure 5.6 the computed wakes of wing C and wing B, and wing C itself are shown. The vertical distance measured from wing B to wing C is zero. The trailing vortices induce a downward velocity on the wing and cause the aerodynamic load to decrease. As the vertical distance between these two wings increases, the influence of the trailing vortices reduces.

It was shown (Figure 5.5) that the aerodynamic loads are not symmetric with respect to Z=0. In Figures 5.7 and 5.8 the calculated wakes of wing C and wing B, and wing C itself when Y=0 are shown. In Figure 5.7 wing C is 1.5 chord lengths above wing B and in Figure 5.8 it is 1.5 chord lengths below wing B. Comparing these two figures provides an answer to the question of why the aerodynamic loads for these two cases are not the same. The trailing vortices of a wing induce a downward velocity on the wing and its wake, called downwash. Downwash causes the wake to be pushed down. This phenomenon is shown in Figures 5.7 and 5.8. In Figure 5.8 the wake of wing B is closer, vertically, to wing C in comparison with Figure 5.7. Therefore, wing C is influenced by a stronger downwash, for Z=1.5 chord. Hence, a lower aerodynamic load on wing C is expected for Z=1.5 chord in comparison with Z=-1.5 chord and Figure 5.5 verifies this.

So far, the mid-span of wing C has been aligned with the mid-span of wing B, Y=0. Because of symmetry, the side force and roll moment are zero. When Y is not zero, the side force is still small, but the roll moment can become significant as wing C approaches the trailing vortex of wing B. In Figure 5.9 the coefficients of lift, drag force, roll, and pitch moment are shown as functions of position measured from wing B to wing C in a transverse direction. Wing C is located 2 chord lengths above wing B. The maximum roll moment occurs before the maximum lift, drag, and pitch moment are reached. The maximum lift and drag coefficients occur when the position between the two wings in transverse direction, Y, is -6 chord lengths. The maximum pitch moment occurs when Y is about -5 chord lengths. The roll moment reaches a peak value and then reduces to zero, which indicates that the

influence of the wake from wing B on wing C is decreasing.

In Figure 5.10 the wakes behind wing B and wing C, and wing C itself are shown. In this figure Y is -4 and Z is -2 chord lengths. The figure shows the position of both wings. The Mid-span of wing C is very close to the wing-tip vortex of wing B. Therefore, a strong roll moment on wing C is expected and Figure 5.9 confirms it. Due to upwash, an increase in the lift coefficient is expected.

To clarify the effect of the wake of wing B on wing C in more detail, some of the velocity vectors in a Trefftz plane located four chord lengths behind wing C are plotted. In Figure 5.11 the velocity vectors in a Trefftz plane located four chord lengths behind wing C and the wing itself are shown. The figure shows that the wing-tip vortex of wing B reduces the downwash on wing C. The wake from wing B influences the direction of the velocity vectors acting on wing C.

In Figure 5.12 the coefficients of lift, drag force, roll, and pitch moment are shown as functions of position measured from wing B to wing C in a transverse direction. Wing C is now two chord lengths below wing B. Again, the peak roll moment occurs before the peak lift, drag force, and pitch moment. Comparison of Figure 5.9 with Figure 5.12 shows that at Y=0 wing C is more influenced when Z=2 chord lengths in comparison with the case when Z=-2 chord lengths. When Z=2 chord lengths, wing C is below wing B and the wake coming from wing B is being pushed down by its trailing vortices. Therefore, for the case Z=2 chord lengths, the wake of wing B influences wing C more than the case when Z=-2 chord lengths.

In Figure 5.13 the calculated wakes of wing B and wing C, and wing C itself are shown. The influence of the trailing vortex from wing B on wing C increases as they approach each other. The roll moment of wing C increases as the mid-span of wing C approaches the core of the trailing vortex of wing B. A relative distance of approximately 3.2 chord lengths aligns the mid-span of wing C with the core of wing B (transversely). In Figure 5.14 the coefficients of lift, drag force, roll, and pitch moment are shown as functions of vertical distance between the two wings. Again, the figure verifies that as the distance between the

two wings increases, the influence of wing B on wing C decreases.

In Figures 5.15 and 5.16 the wakes of both wings and wing C itself are shown. Y=-3.2 chord lengths for both figures, Z=1 chord length for Figure 5.15, and Z=2 chord lengths for Figure 5.16. These figures show the position of both wings and their calculated wakes. To analyze the effect of the wake from wing B on wing C in more detail, the velocity vectors in a Trefftz plane and wing C itself are shown in Figure 5.17, where Y=-3.2 chord length and Z=1 chord length. The wake of wing B influences the direction of the velocity vectors on wing C. The wake from wing B causes the velocity vectors to be more horizontal in direction. The wake decreases the downwash on wing C, causing the lift and roll moment to increase. Figure 5.15 verifies this. In Figure 5.18 the velocity vectors and wing C itself are shown. The transverse position of wing C from wing B is the same, Y=-3.2 chord length and the vertical distance is 4 chord lengths. The wake from wing B increases the downwash on wing C. In Figure 5.19 the two wings are rather far from each other, Z=10 chord lengths. In this figure Y=-3.2 chord lengths. As Z/C increases the influence of wing B on wing C decreases. But when Z=10 and Y=-3.2 chord lengths wing B still has some influence on wing C when Y=-3.2 chord lengths.

In Figure 5.20 the coefficients of lift, drag force, roll, and pitch moment are shown as functions of the vertical position. Y is -3.2 chord lengths but wing C is above wing B. As the magnitude of Z/C increases, the influence of the wake of wing B on wing C decreases. When the vertical distance between these two wings is as high as 10 chord lengths, there is still influence from wing B on wing C. However, the effect on the roll moment is very small.

In Figures 5.21 and 5.22 the calculated wakes and wing C itself are shown when Y=-3.2 chord lengths. In Figure 5.21 Z=-1 chord length and the effect of wing C and its wake on wing B is shown. Wing B is far away from wing C and its wake, so, their effect on the aerodynamic load of wing B is negligible. The trailing vortex coming from wing B is almost below the mid-span of wing C; therefore, a large roll moment develops as shown in Figure 5.20. In Figure 5.23 the velocity vectors when Y=3.2 chord lengths and Z=-1 chord lengths in the Trefftz plane are shown. The velocity vectors are in an upward direction on

one side of the wing and in a downward direction on the other side, causing a high value of the roll moment.

In Figure 5.24 the coefficients of lift, drag force, roll, and pitch moment are shown as wing C crosses the wake of wing B. The figures indicate that as wing C crosses wing B, its lift coefficient increases due to the upwash of large wing/wake vortex system. But when it flies past the tip, above the wing, the downwash prevailing in that area reduces its aerodynamic load. The drag force and the pitching moment data follow trend similar to the lift data. The upwash induced by wing B causes an increasing rolling moment. As wing C slides under wing B, this trend is reversed (before crossing) and once wing C moves behind wing B its rolling moment becomes positive again. As wing C crosses the left trailing-edge wake of wing B, the trend reverses and slowly decays to the steady-state condition.

In Figures 5.25 and 5.26 the calculated wakes of wing B and wing C and both wings are shown. In these two figures the two wings are moving along various paths. The angle between their paths is 45 degrees. The wake of wing B has strong influence on the wake of wing C. Therefore, the aerodynamic load of wing C will be affected by the distortion of the wake.

The wake of a smaller plane has some slight influence on the wake of the bigger plane. In Figure 5.27 the calculated wakes of wing B for different vertical positions and wing C are shown. As the vertical distance between the wings decreases, the wake and wing of wing C causes the wake of wing B to spread in spanwise direction. In Figure 5.28 the calculated wakes of wing B when it is located at different vertical positions from wing C are shown. Again, as the vertical distance between two wings decreases, the wake of wing B spreads in spanwise direction.

5.4 Conclusion

The trailing vortices from a larger leading wing can influence the aerodynamic load on a trailing wing. The magnitude of this effect depends upon the distance between the

two wings. The aerodynamic load of a smaller wing, corresponding to a Cessna 750, was investigated when it is affected by the wake of a larger wing, a Boeing 757. The aerodynamic load on the Cessna 750 was examined when these two wings have different distances between them. Although there are a few positions where the lift on the trailing aircraft increases, in most cases there is a remarkable loss of the lift. Even at a distance of 10 chords (transversely and vertically) from each other, the aerodynamic load on the Cessna 750 is affected by the wake of the Boeing 757. When the mid-span of two wings are aligned, Y=0, the roll moment is zero. But as the mid-span of smaller wing approaches the core of the trailing vortex of the larger wing, the roll moment increases. The value of the roll moment is highest when the mid-span of the smaller wing is closest to the core of the trailing vortex of the larger wing.

When these wings are not moving along the same path, there is initially a small increase in the aerodynamic load due to the upwash. Then it reduces considerably and again increases.

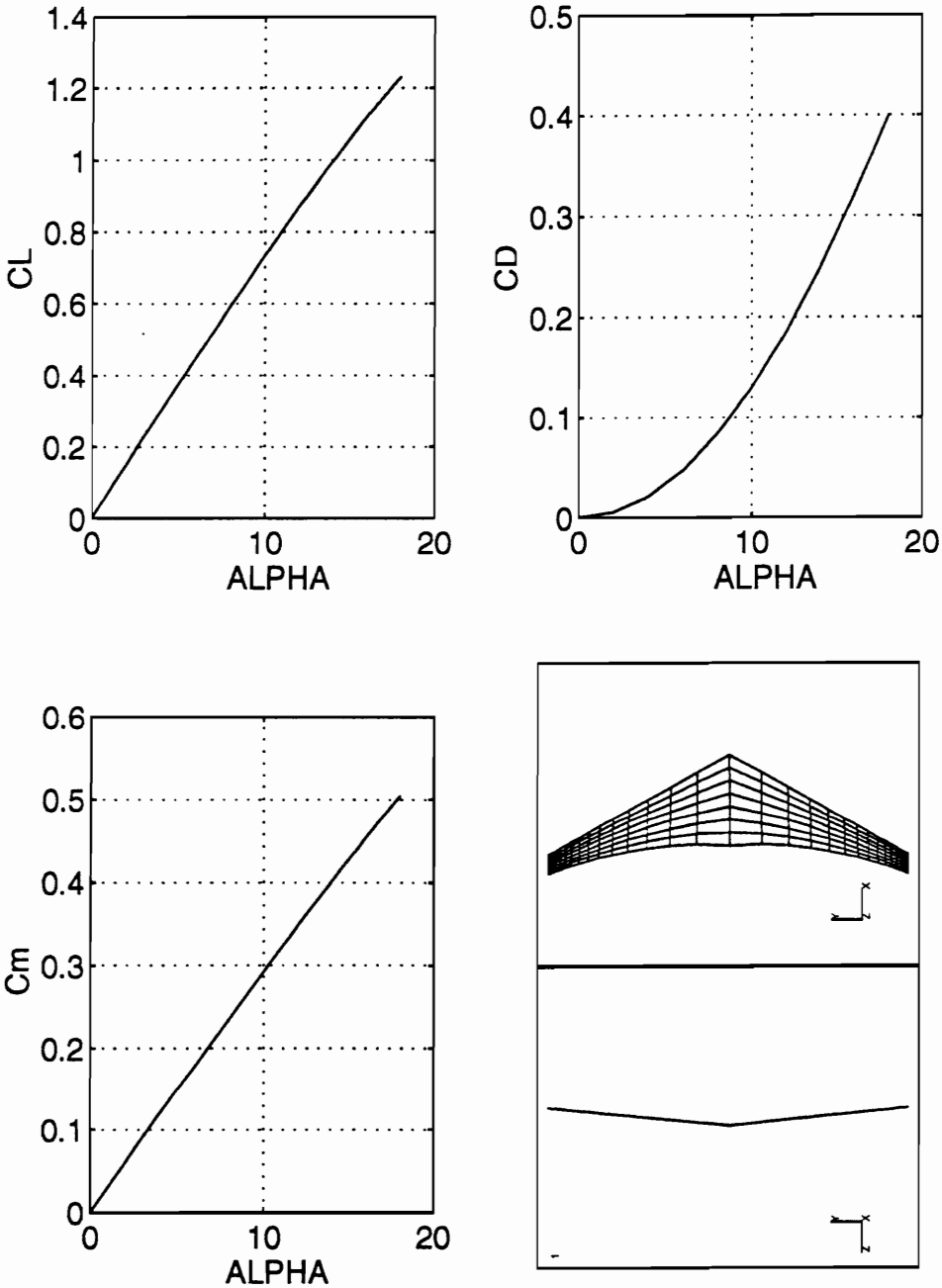

Figure 5.1: Calculated lift, drag, and moment coefficients as functions of the angle of attack for the wing of a Boeing 757.

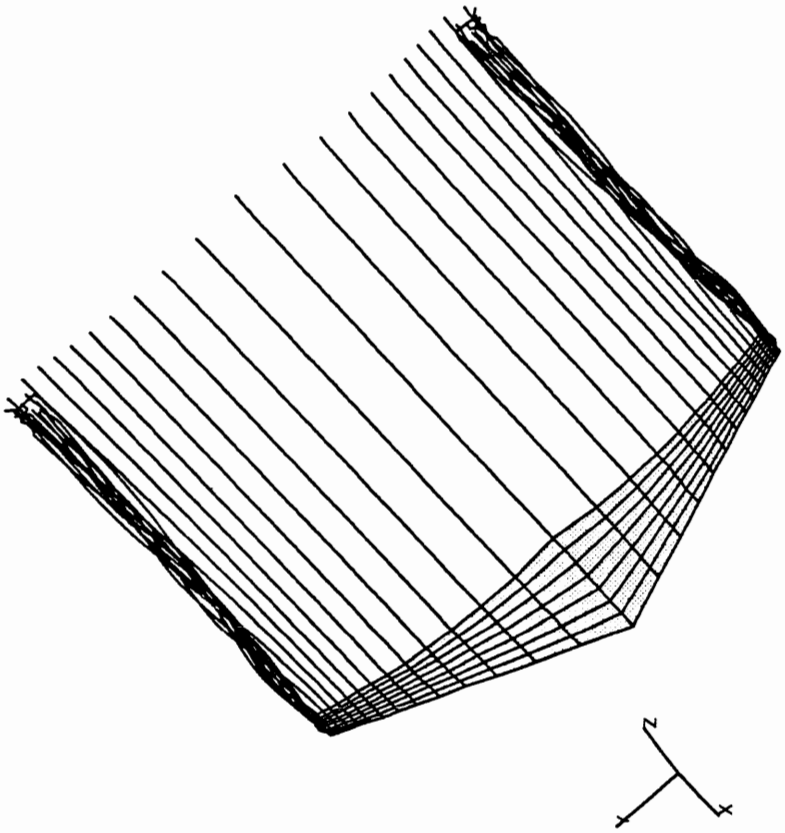

Figure 5.2: Computed wake for the wing of the Boeing 757 with 7 degrees angle of attack.

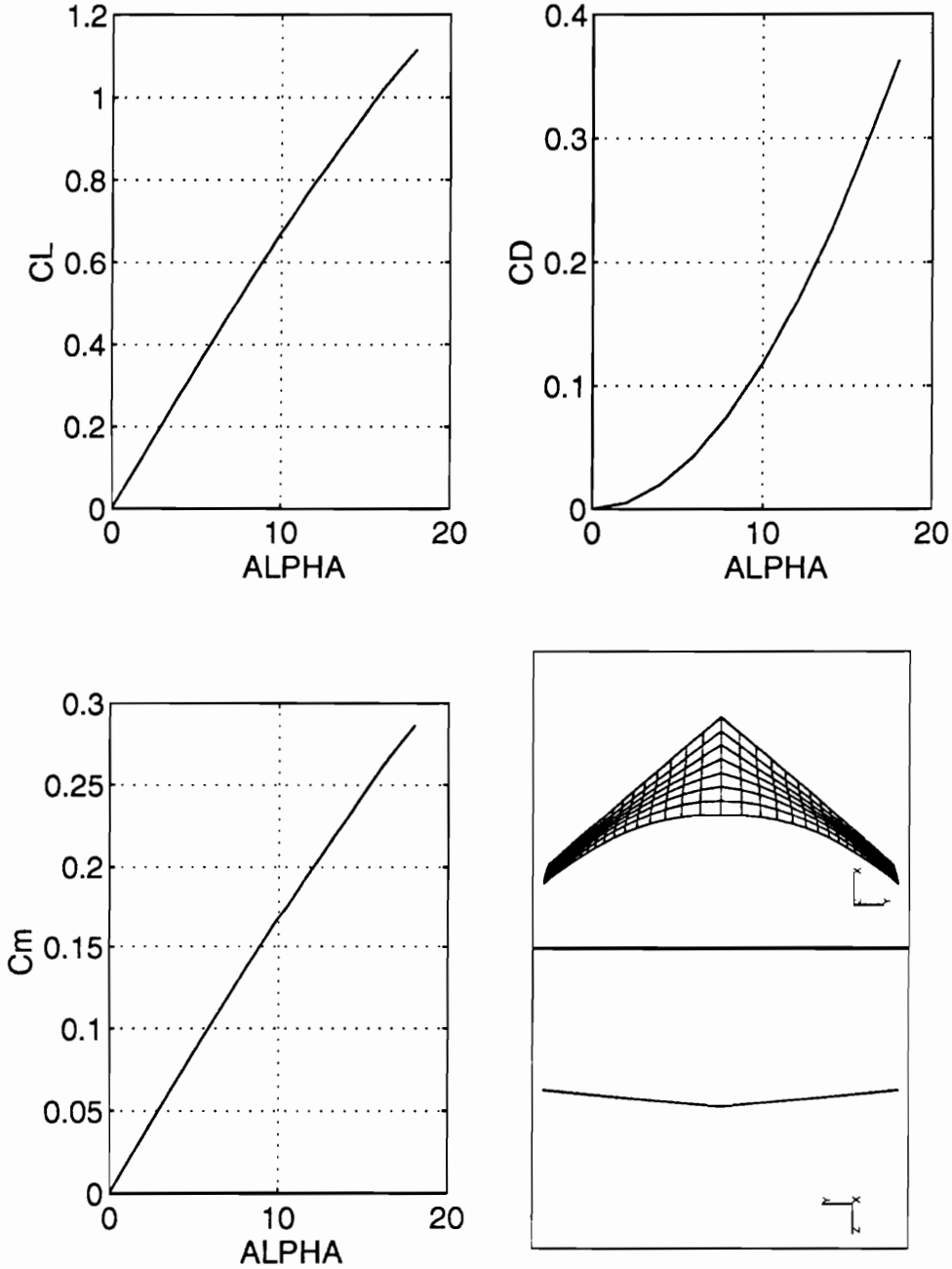

Figure 5.3: Calculated lift, drag, and moment coefficients as functions of the angle of attack for the wing of the Cessna 750 Citation X.

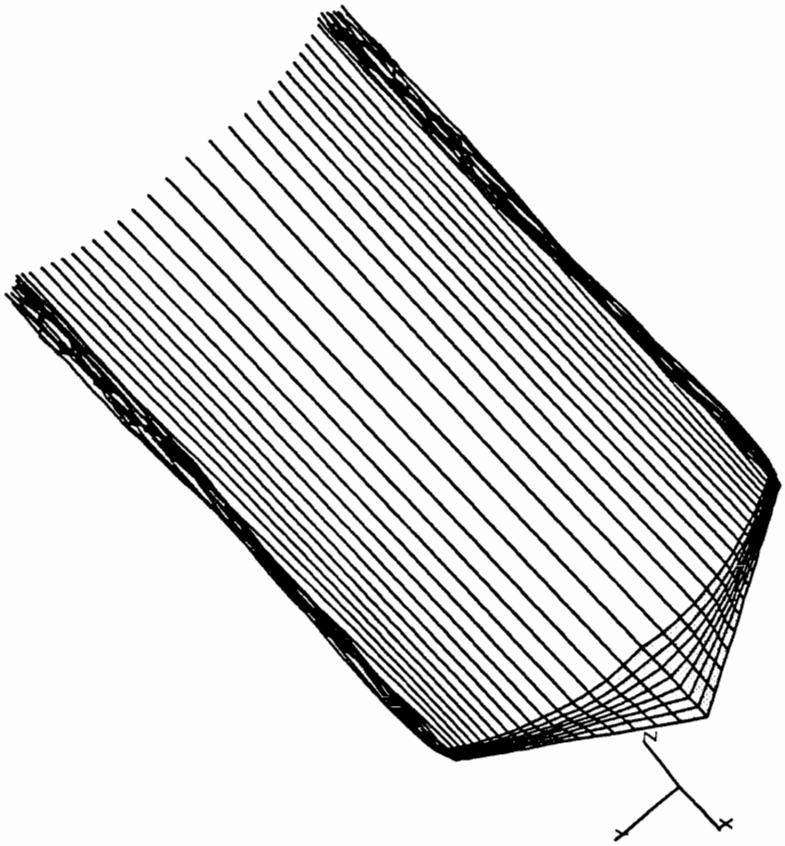

Figure 5.4: Computed wake for the wing of the Cessna 750 citation X with 5 degrees angle of attack.

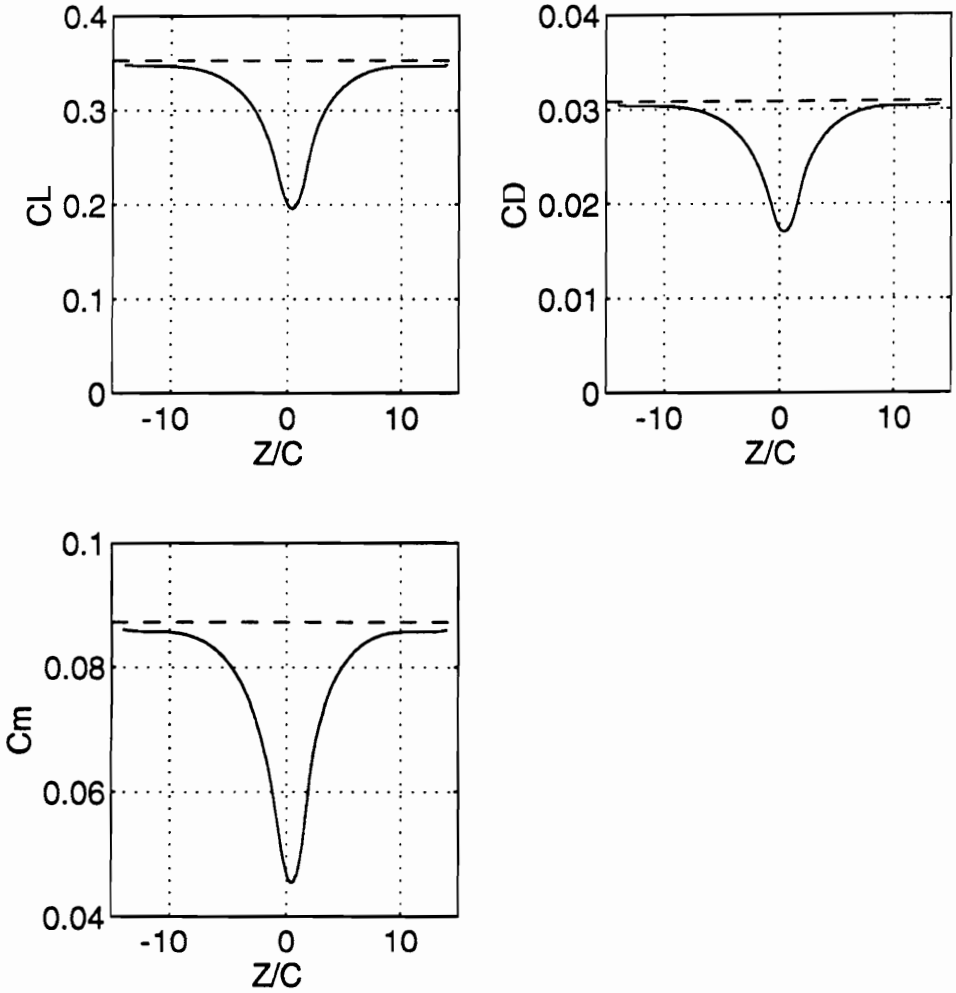

Figure 5.5: Lift, drag, and moment coefficients for the Cessna flying with 5 degrees angle of attack.
—— Cessna wing near the wake of the 757 for Y/C=0.
- - - Cessna wing by itself.

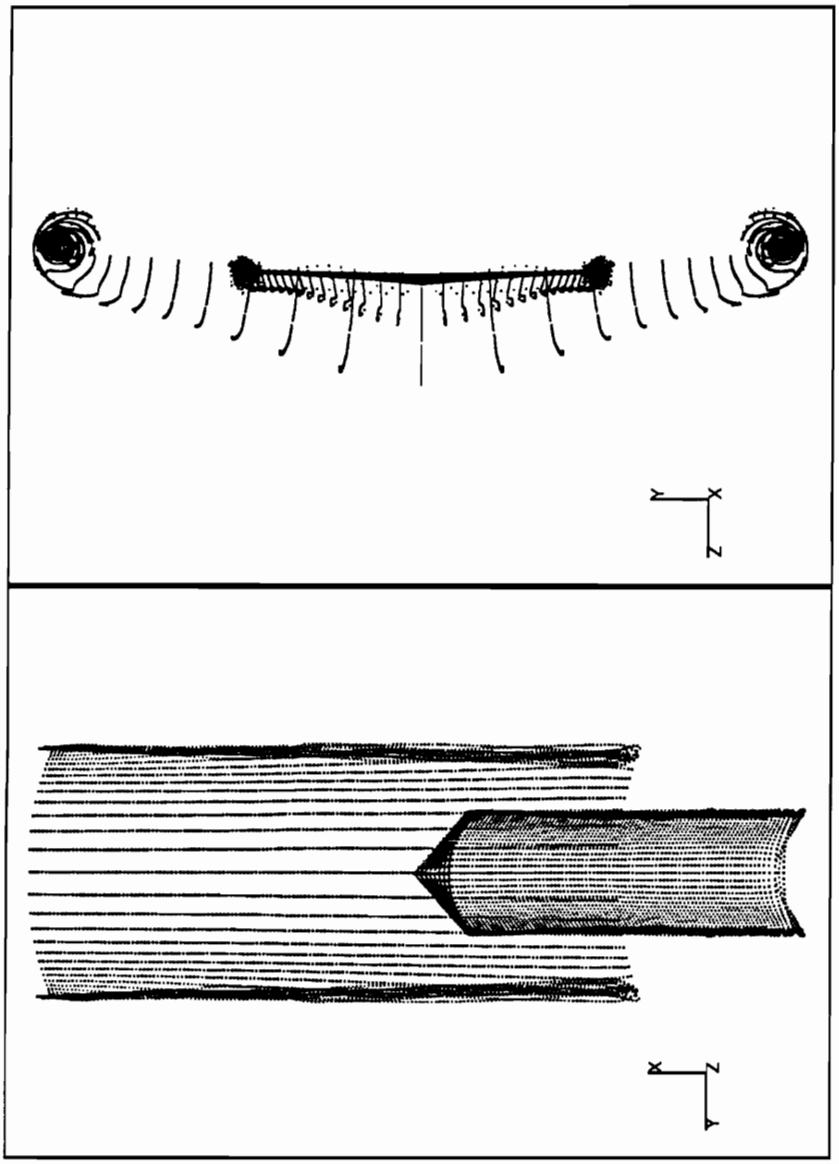

Figure 5.6: The calculated wake of the 757, the wing of the Cessna wing, and its calculated wake, where Y/C=0 and Z/C=0

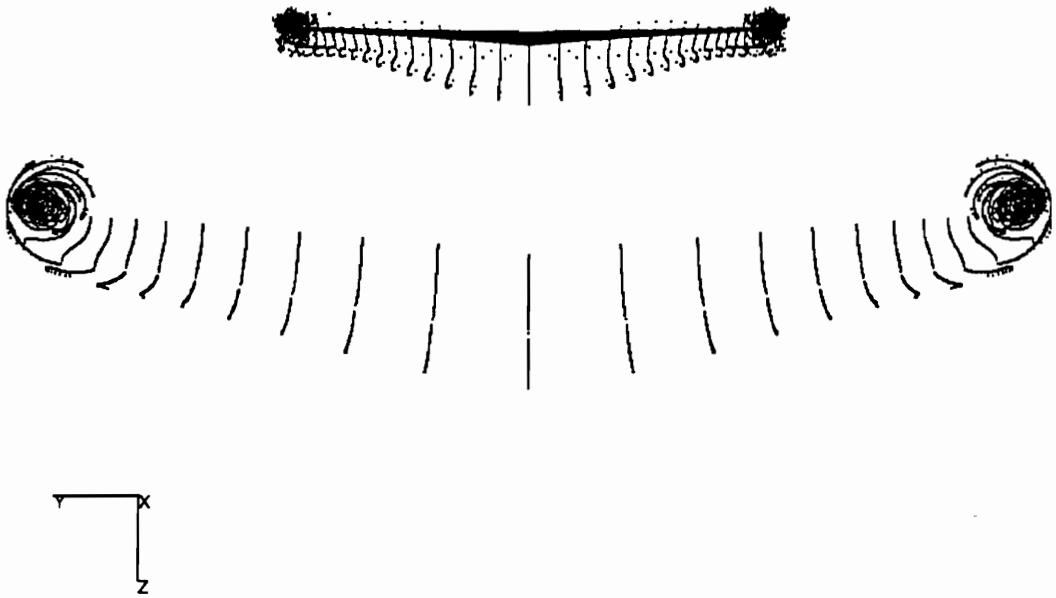

Figure 5.7: The calculated wake of the 757, the wing of the Cessna, and its wake, where Y/C=0 and Z/C=-1.5.

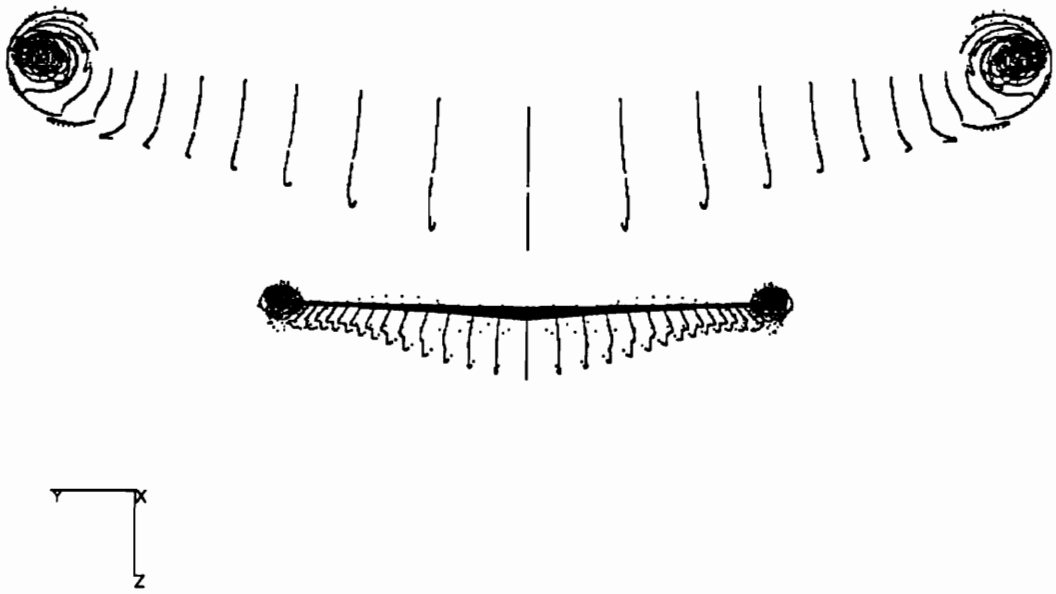

Figure 5.8: The calculated wake of the 757, the wing of the Cessna, and its wake, where Y/C=0 and Z/C=1.5.

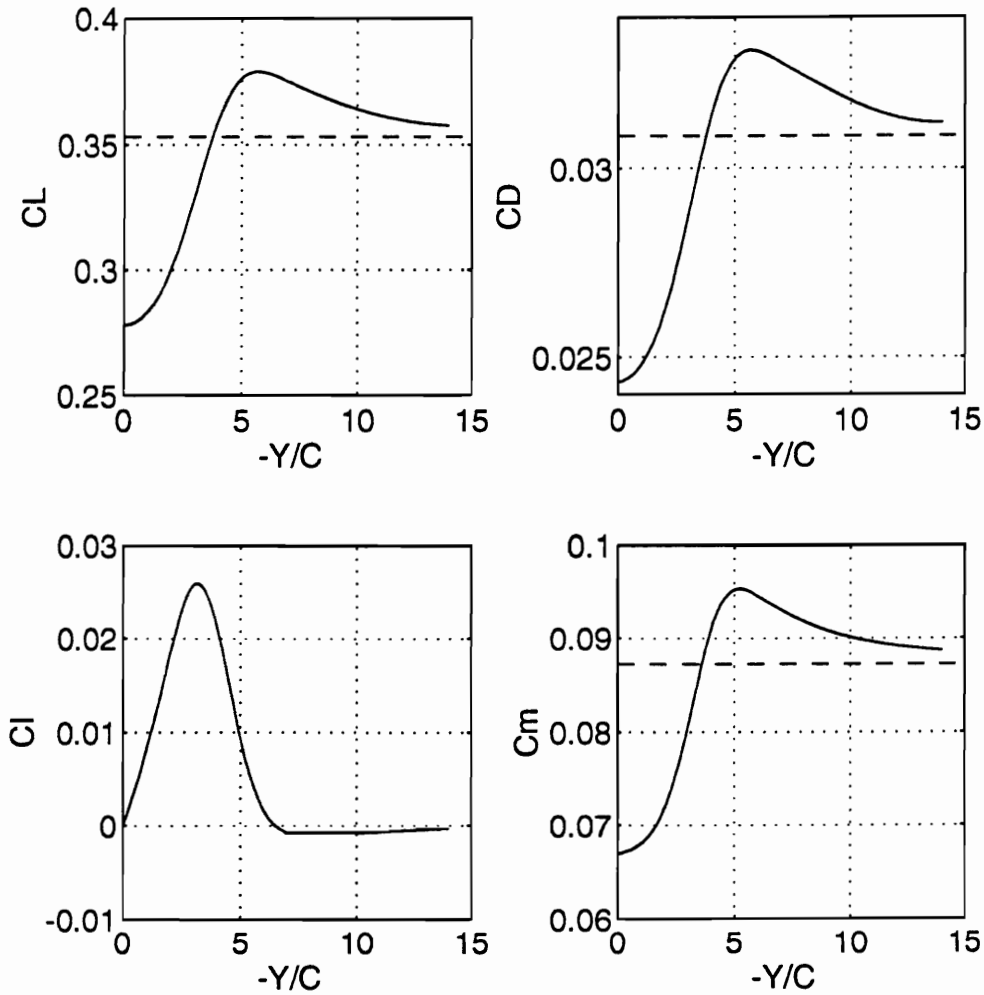

Figure 5.9: Lift, drag, roll, and pitch coefficients for the Cessna flying with 5 degrees angle of attack.
—— Cessna wing near the wake of the 757 for Z/C=-2.
- - - Cessna wing by itself.

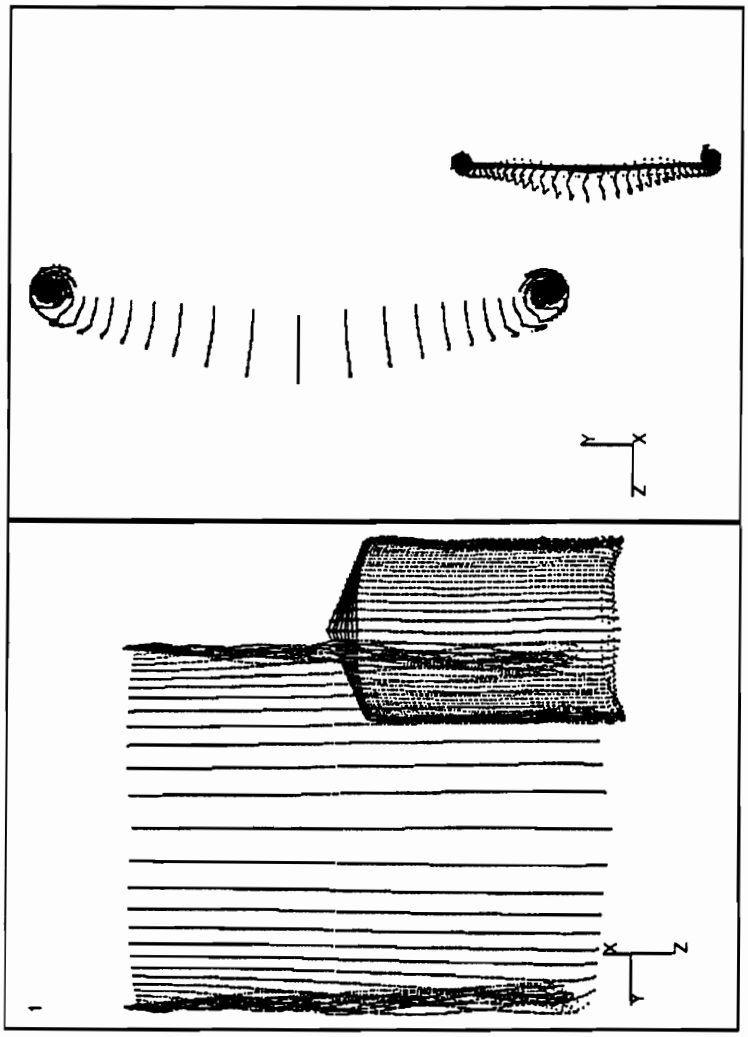

Figure 5.10: The calculated wake of the 757, the wing of the Cessna, and its calculated wake, where Y/C=-4 and Z/C=-2.

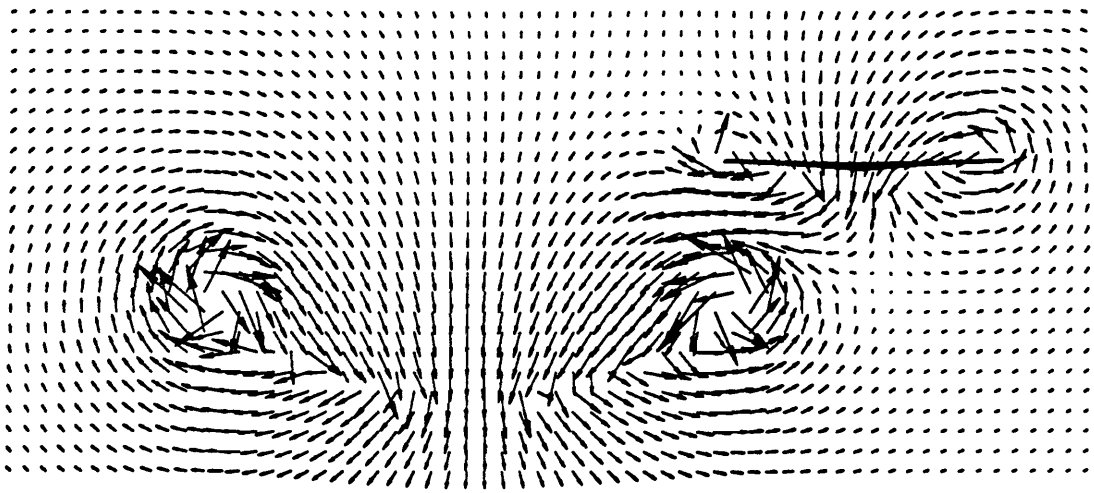

Figure 5.11: The wing of the Cessna and the velocity vectors in the Trefftz plane located four chord lengths behind the wing of the Cessna, where Y/C=-5 and Z/C=-2

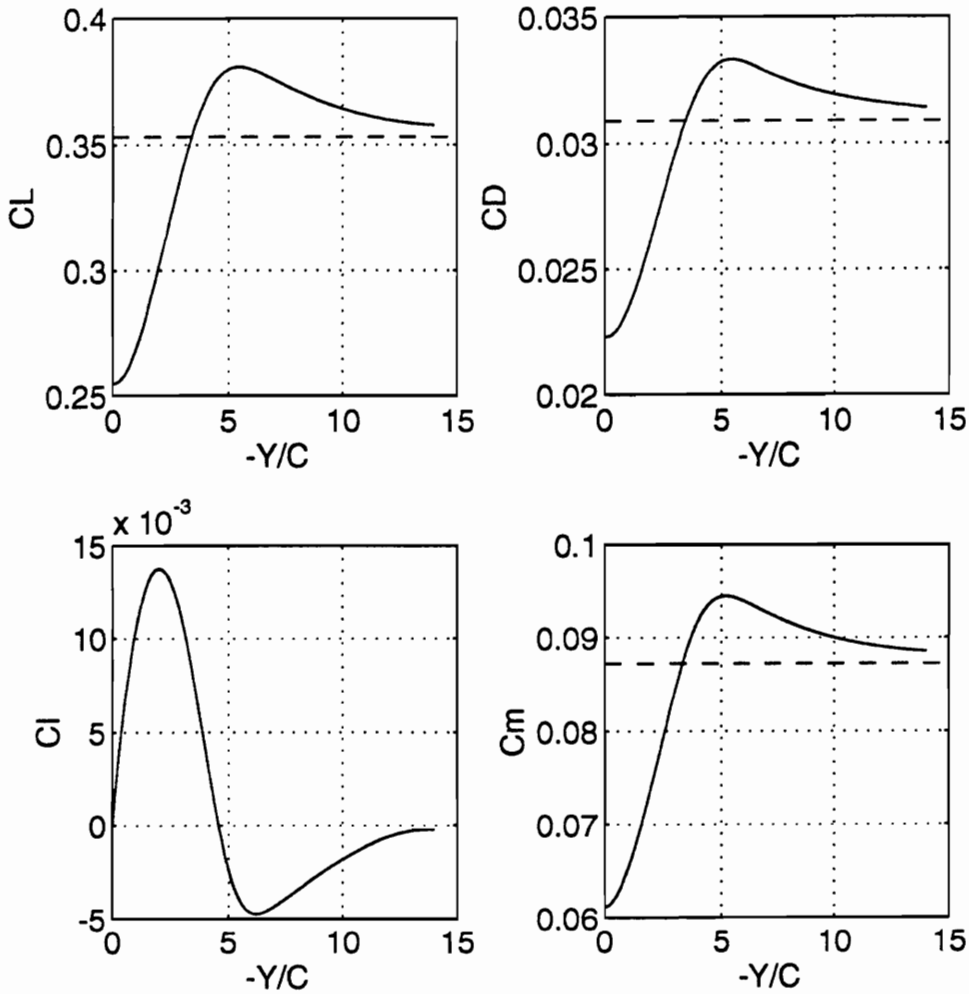

Figure 5.12: Lift, drag, roll, and pitch coefficients for the Cessna flying with 5 degrees angle of attack.
—— Cessna wing near the wake of the 757 for Z/C=2.
- - - Cessna wing by itself.

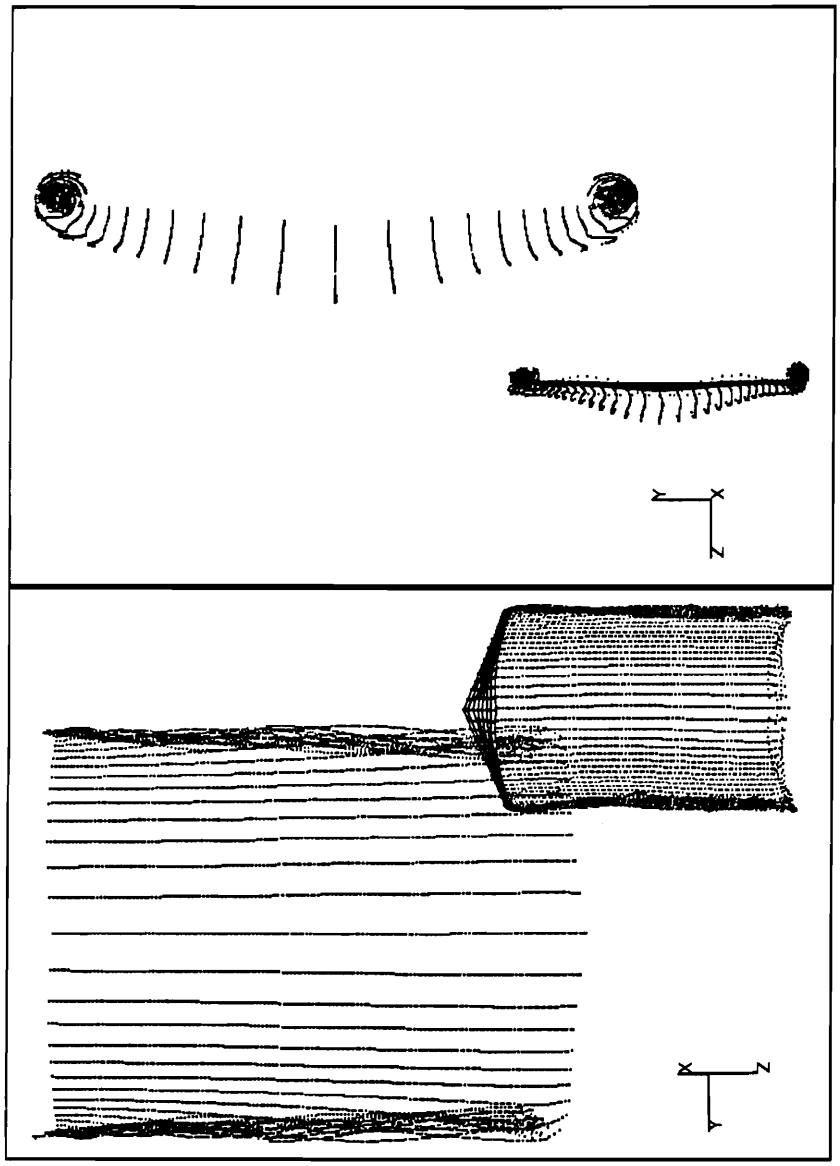

Figure 5.13: The calculated wake of the 757, the wing of the Cessna, and its calculated wake, where Y/C=-4 and Z/C=2.

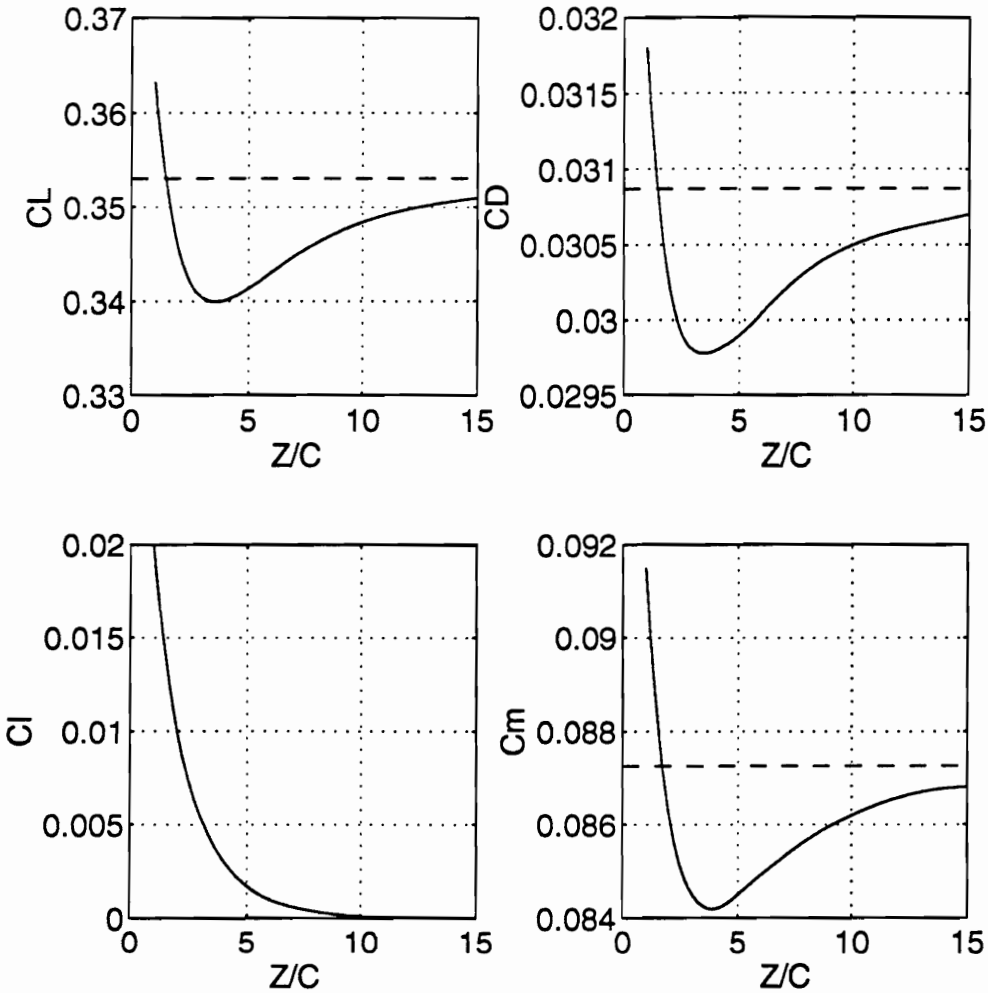

Figure 5.14: Lift, drag, roll, and pitch coefficients for the Cessna flying with 5 degrees angle of attack.

—— Cessna wing near the wake of the 757 for Y/C=-3.2.

- - - Cessna wing by itself.

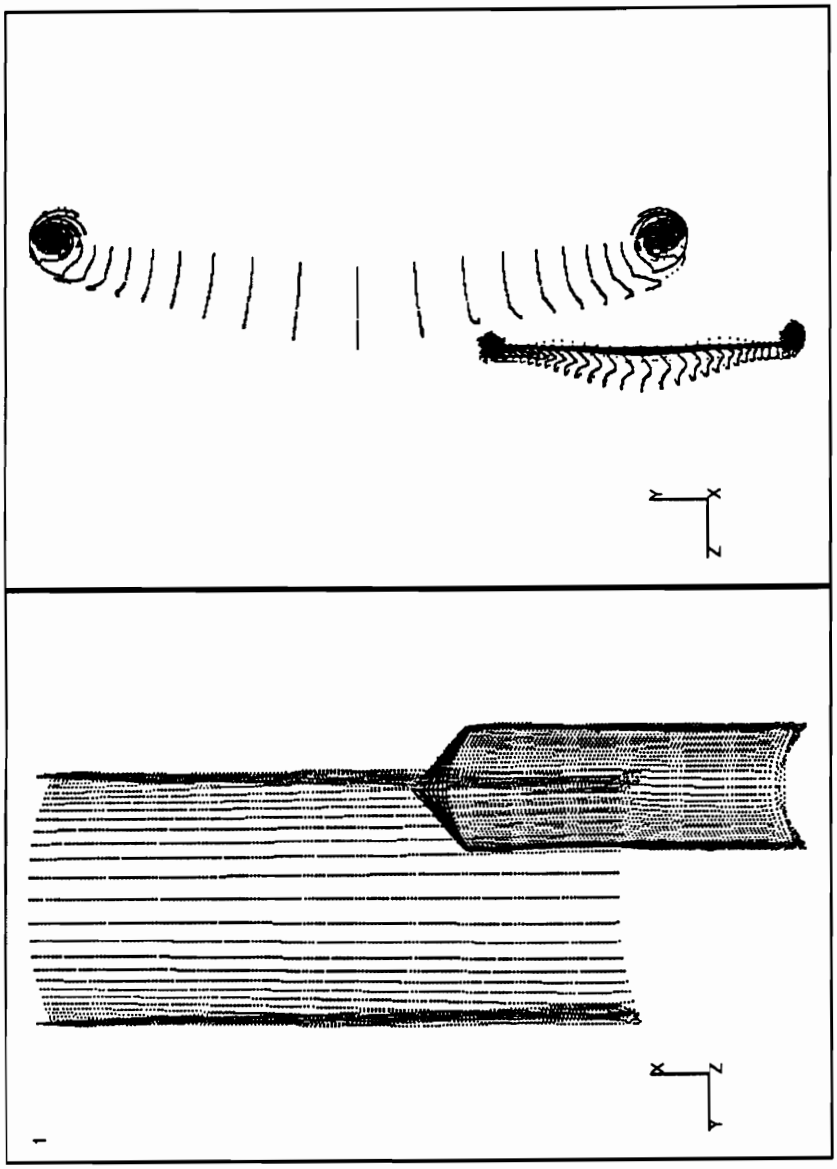

Figure 5.15: The calculated wake of the 757, the wing of the Cessna, and its wake, where Y/C=-3.2 and Z/C=1.

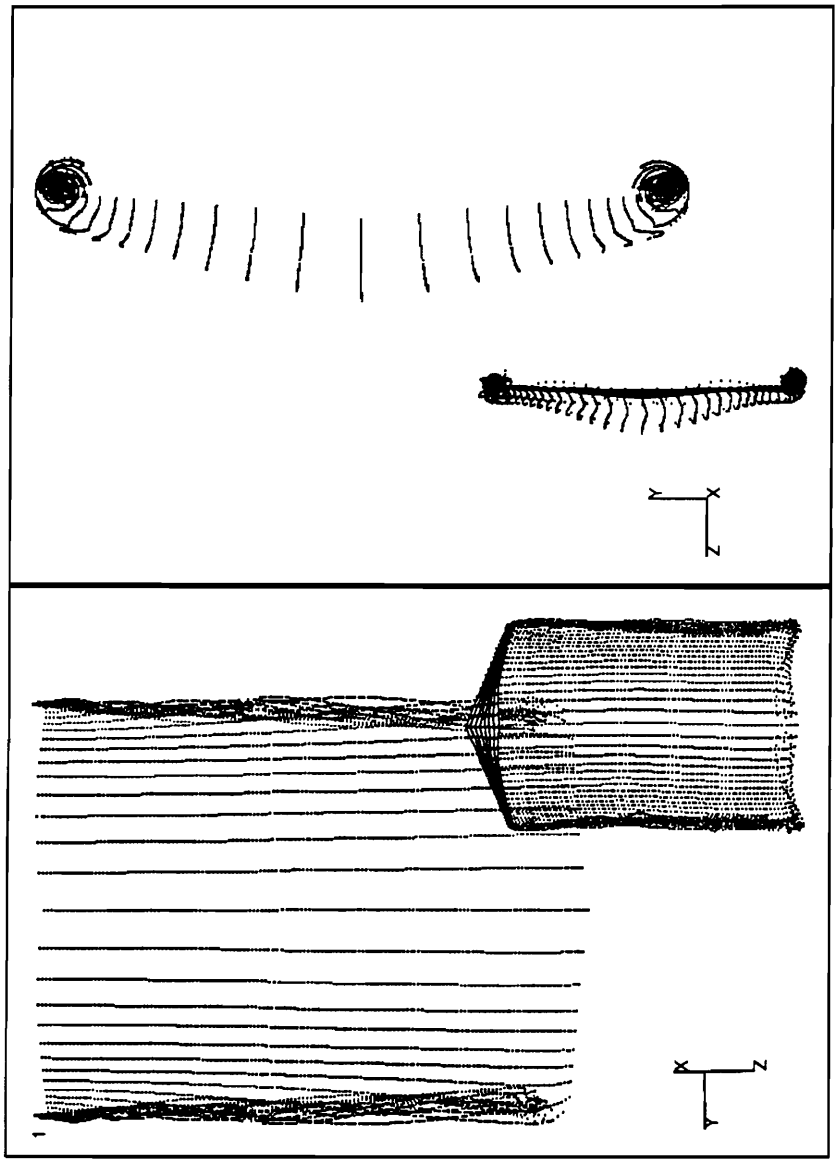

Figure 5.16: The calculated wake of the 757, the wing of the Cessna, and its wake, where Y/C=-3.2 and Z/C=2.

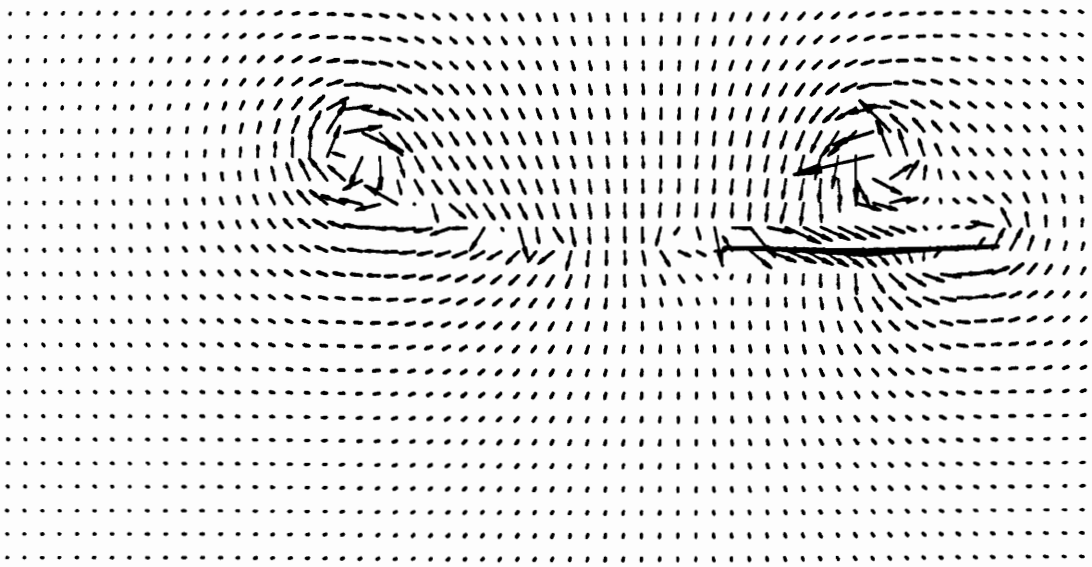

Figure 5.17: The wing of the Cessna and the velocity vectors in the Trefftz plane located four chord lengths behind the wing of the Cessna, where Y/C=-3.2 and Z/C=1.

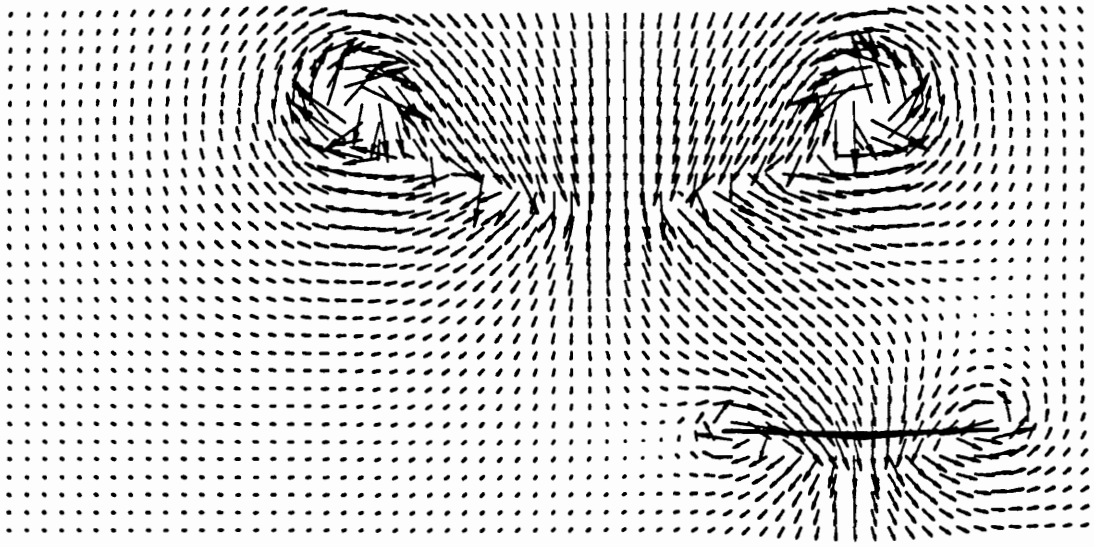

Figure 5.18: The wing of the Cessna and the velocity vectors in the Trefftz plane located four chord lengths behind the wing of the Cessna, where Y/C=-3.2 and Z/C=4.

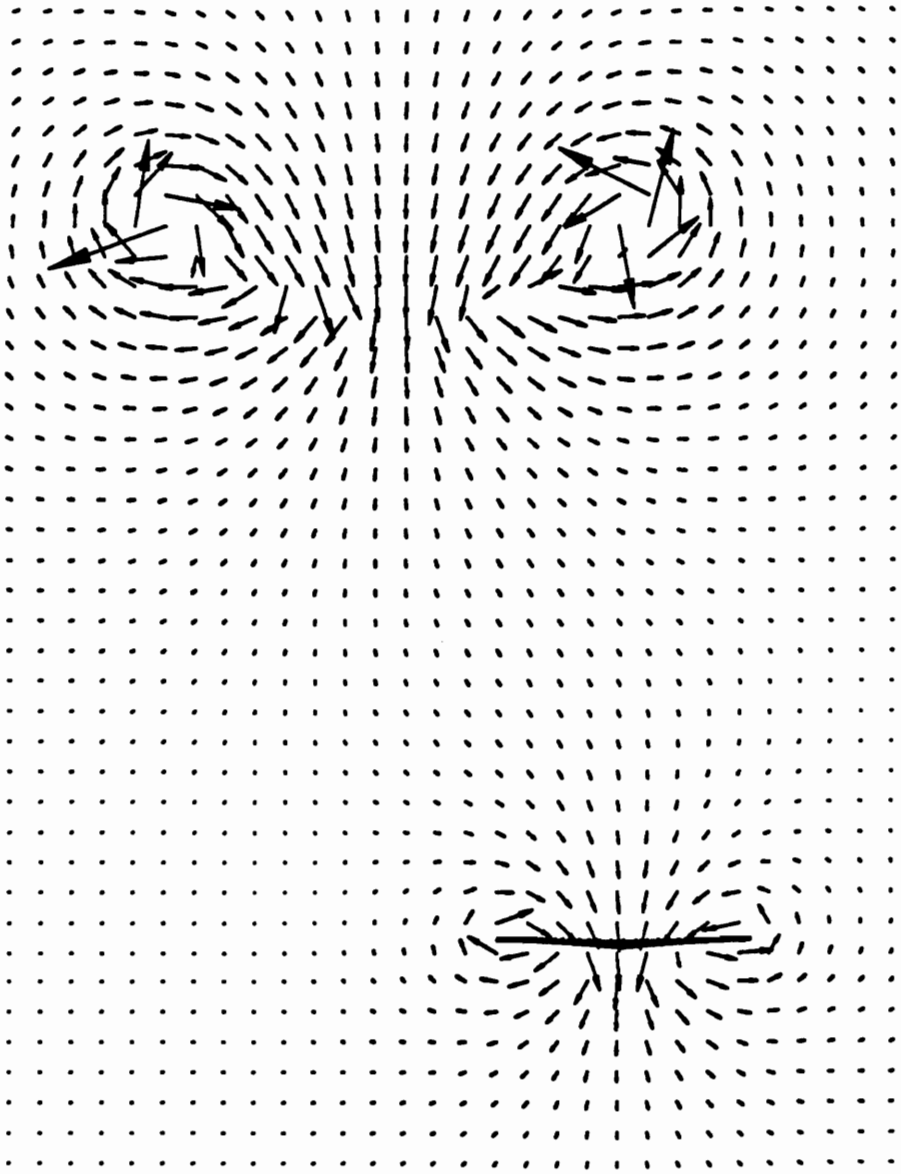

Figure 5.19: The wing of the Cessna and the velocity vectors in the Trefftz plane located four chord lengths behind the wing of the Cessna, where Y/C=-3.2 and Z/C=10.

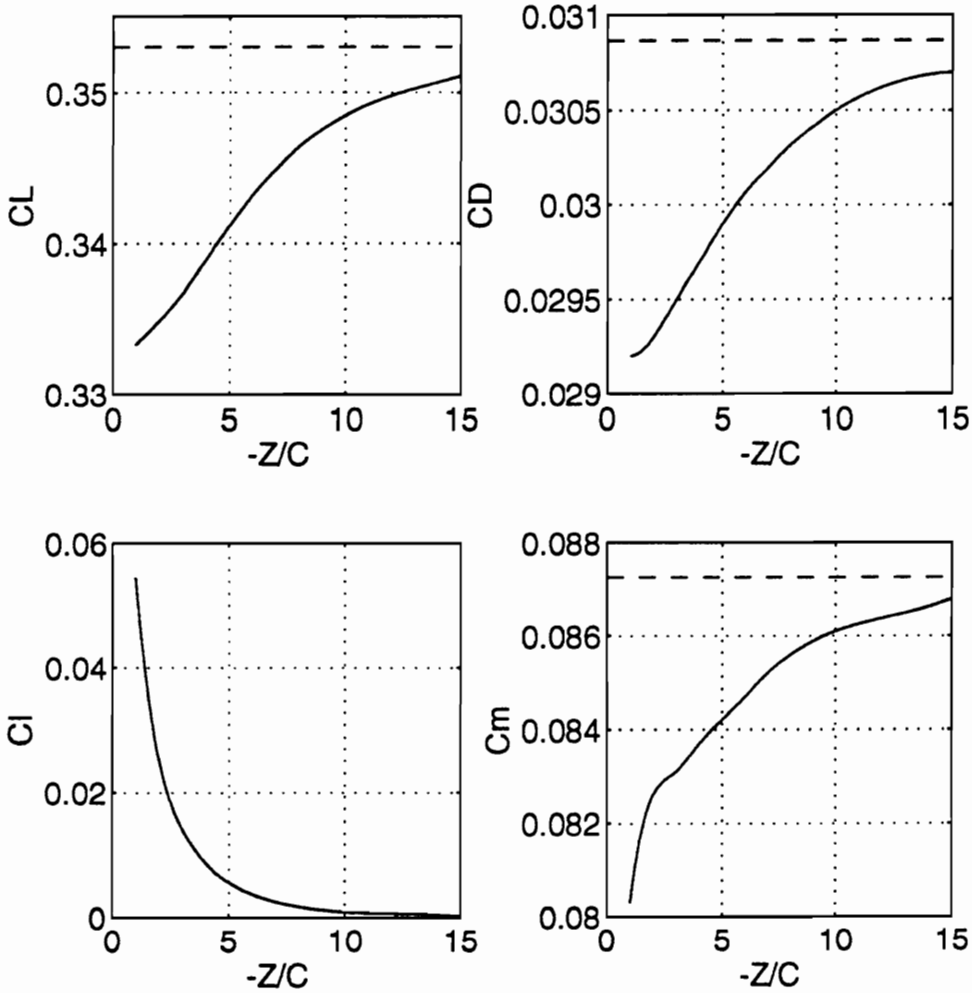

Figure 5.20: Lift, drag, roll, and pitch coefficients for the Cessna flying with 5 degrees angle of attack.
—— Wing of the Cessna near the wake of the 757 for Y/C=-3.2.
- - - Cessna wing by itself.

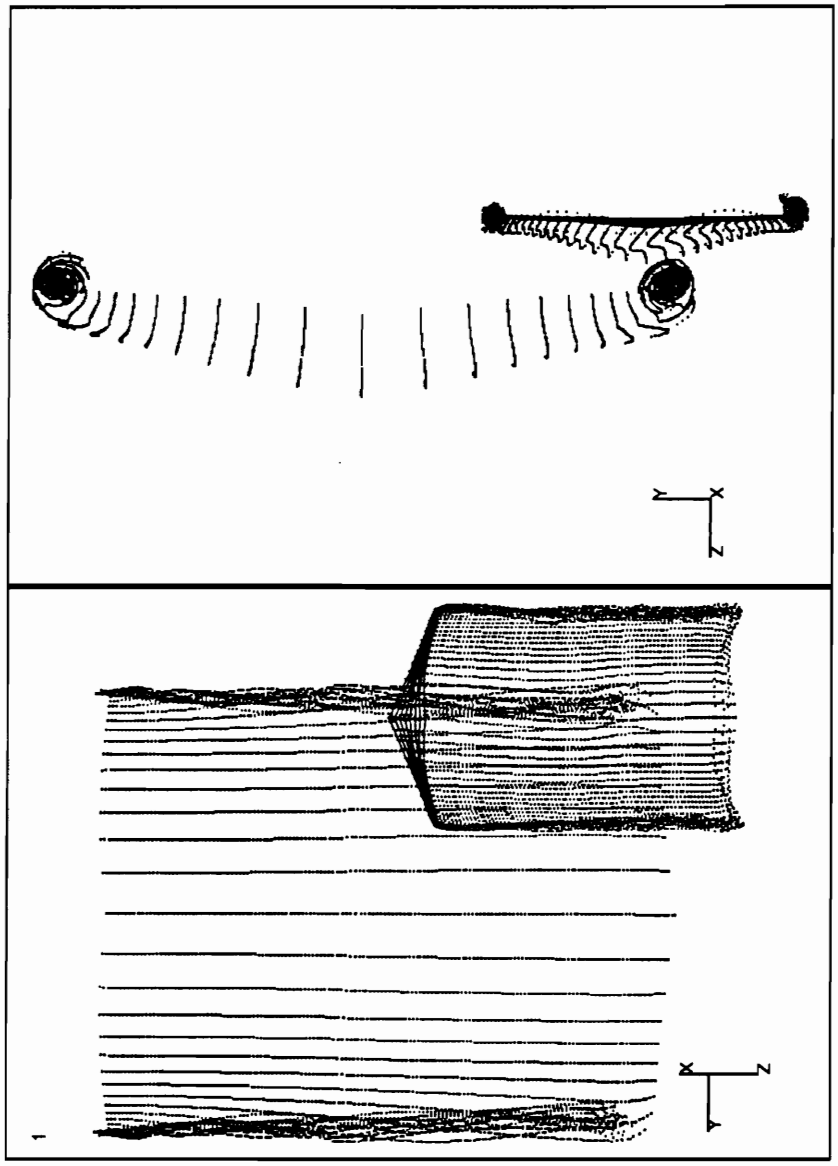

Figure 5.21: The calculated wake of the 757, the wing of the Cessna, its wake, where Y/C=-3.2 and Z/C=-1.

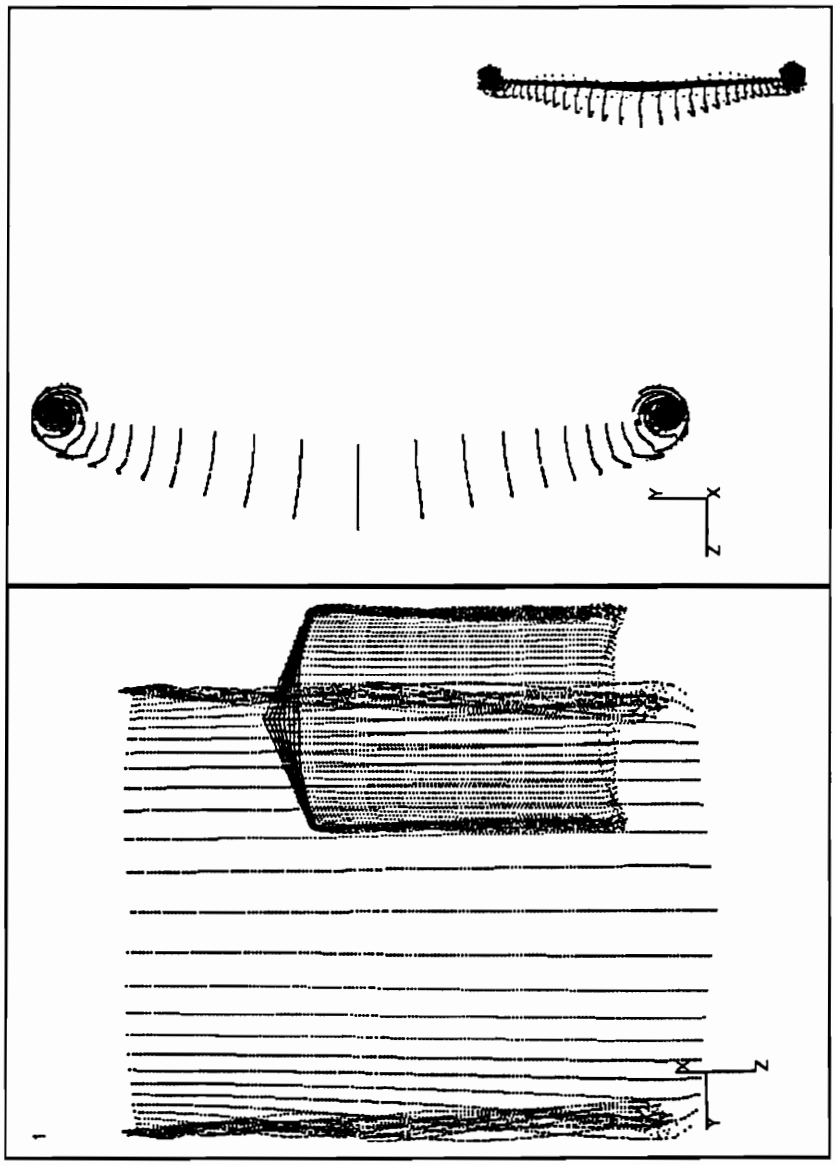

Figure 5.22: The calculated wake of the 757, the wing of the Cessna, and its wake, where Y/C=-3.2 and Z/C=-4.

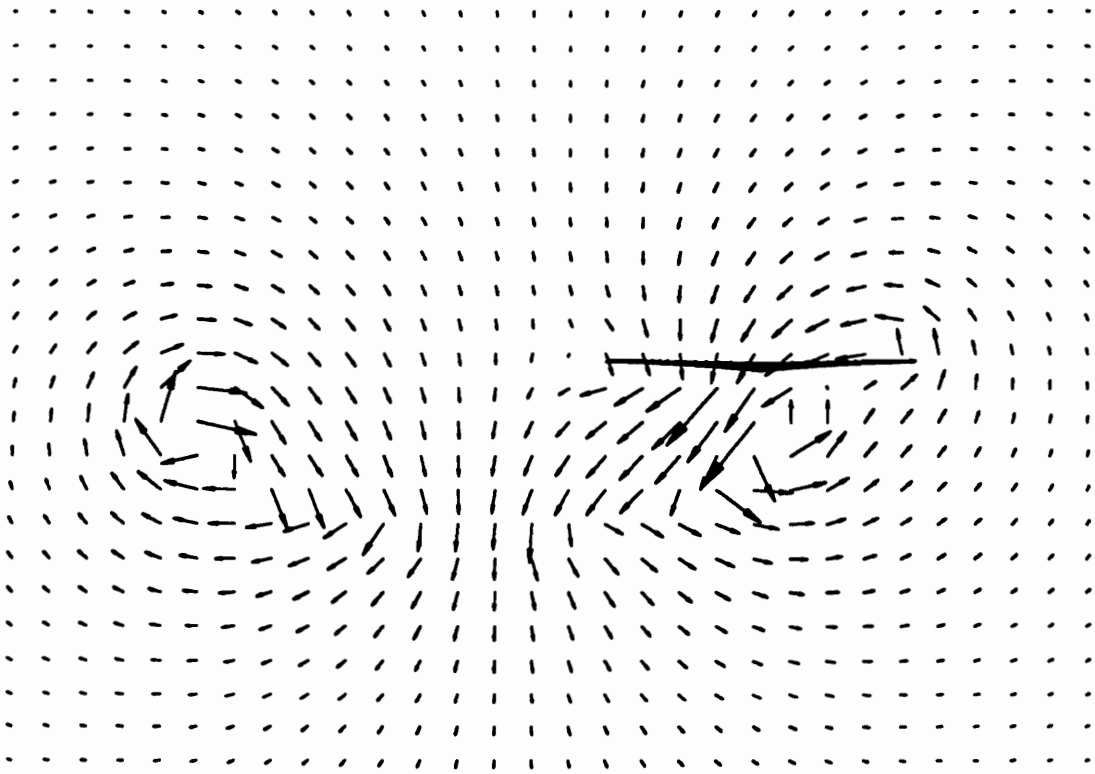

Figure 5.23: The wing of the Cessna and the velocity vectors in the Trefftz plane located four chord lengths behind the wing of the Cessna, where Y/C=-3.2 and Z/C=-1.

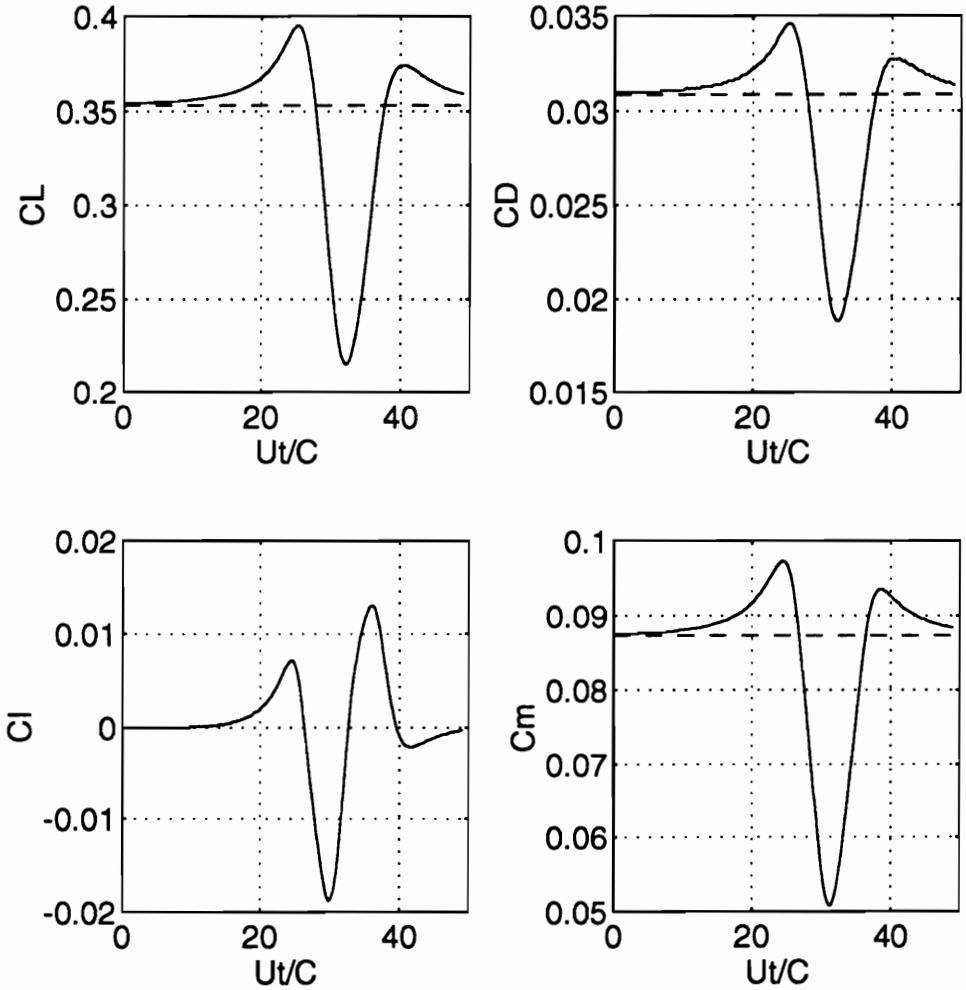

Figure 5.24: Lift, drag, roll, and pitch coefficient for the Cessna as it passes the wake of the 757. The angle between their paths is 45 degrees. The angle of attack of Cessna is 5 degrees and Z/C is 1.5.

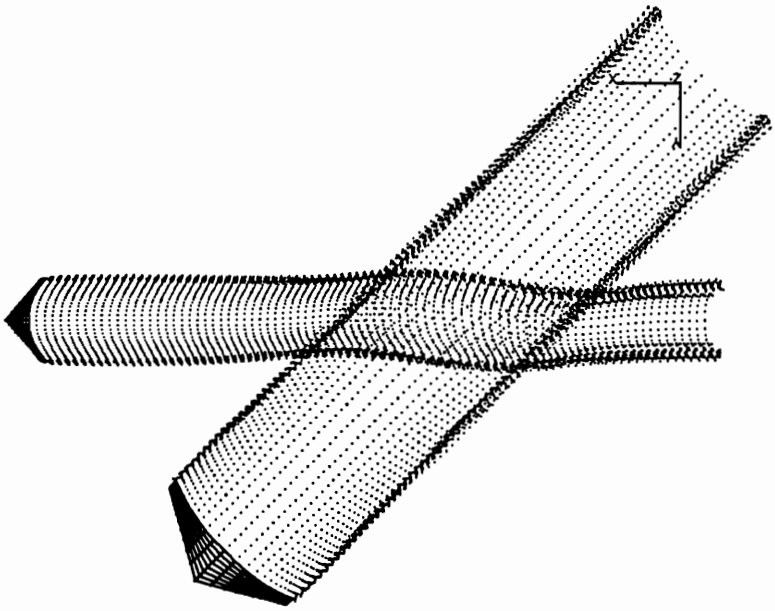

Figure 5.25: The wings and calculated wakes of the Cessna and the 757, where the angle between their paths is 45 degrees and Z/C is 1.5. The angles of attacks are 5 degrees for the Cessna and 7 degrees for the 757.

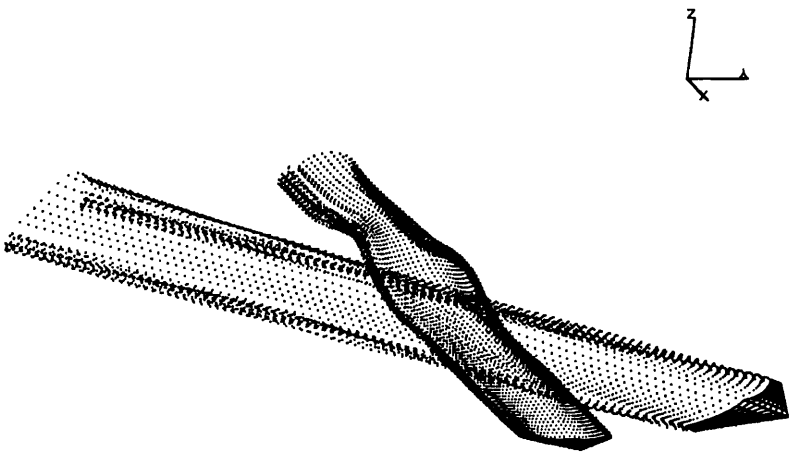

Figure 5.26: The wings and calculated wakes of the Cessna and the 757, where the angle between their paths is 45 degrees and Z/C is 1.5. The angles of attacks are 5 degrees for the Cessna and 7 degrees for the 757.

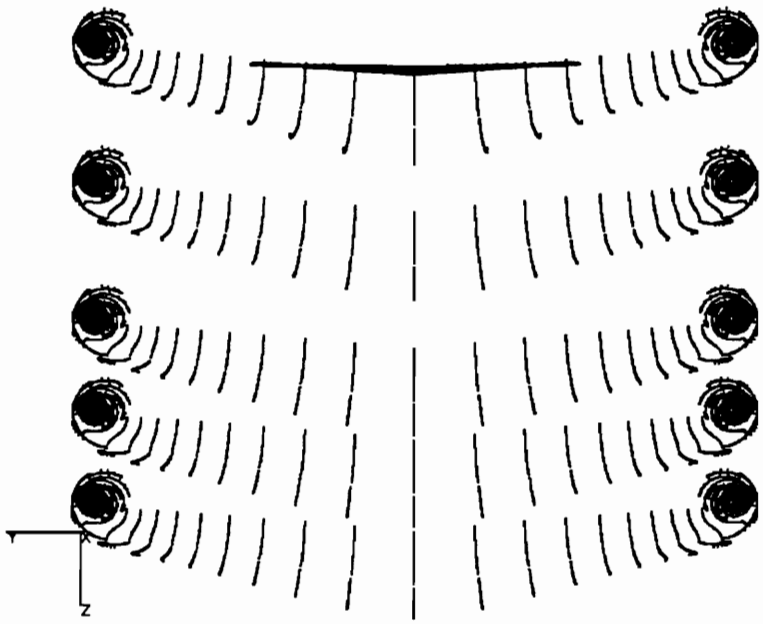

Figure 5.27: Computed wake for the 757 in different heights below the Cessna's wing. The Angles of attack are 7 degrees for the 757 and 5 degrees for the Cessna. The vertical distance measured from the 757 to the Cessna (Z/C) from top to bottom are 0, -1.5, -3, -4, and -5.

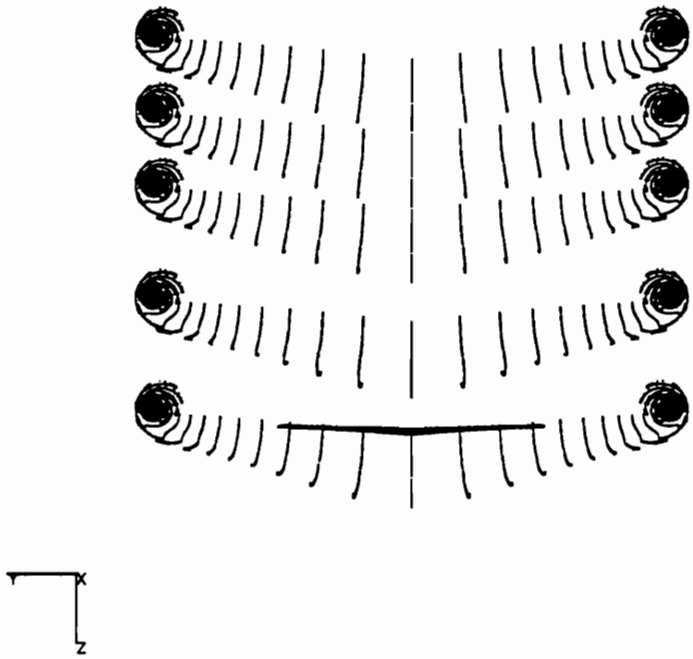

Figure 5.28: Computed wake for the 757 in different heights below the Cessna's wing. The Angles of attack are 7 degrees for the 757 and 5 degrees for the Cessna. The vertical distance measured from the 757 to the Cessna (Z/C) from top to bottom are 0, 1.5, 3, 4, and 5.

Chapter 6

CONCLUSION

6.1 Conclusion

The UVLM is capable of giving accurate lift and moment coefficients for a wing in and out of ground. The method can predict the aerodynamic load on thick nonlifting bodies. Furthermore, the UVLM can model wings in steady and unsteady flows. The method is sensitive to the time step used in the calculation, particularly for an unsteady flowfield.

Calculating the aerodynamic load on a wing is a necessary step in solving the aerodynamic equations simultaneously with the equations of motion. Therefore, the size of the model becomes important. The numerical results obtained from a lifting-surface approximation are in close agreement with the experimental data for a wing as thick as 18%. Therefore, a wing as thick as 18% can be replaced by a lifting surface lying on the camber surface of the actual airfoil.

The vortex-lattice method can predict the aerodynamic load on a thick-wing in oscillation. Predicted lift and moment coefficients are affected when the thickness of a wing is rather high (above 18%). The moment is more sensitive to the thickness than the lift. The results suggest that a thick wing profile would dissipate more energy during a cycle.

Since there is an increase in the ratio of lift to drag that occurs when a wing flies

near the ground, there is an interest in designing airplanes to operate near the ground. An airplane can fly near the surface of the ocean from continent to continent; hence, one application of such craft is transoceanic flight. The interest in transoceanic, ground effect aircraft raises the question of what effect the waves would have on their performance. As a first attempt to simulate a wing flying over a wavy surface, a small-aspect-ratio, slightly cambered wings oscillating in heave near and far from a flat surface is considered. The mean aerodynamic loads on a wing oscillating in heave at a nominal angle of attack are higher than the corresponding loads on a wing in steady flight at the same angle of attack. This result is true for wings operating both near and far from the ground. Therefore, it is concluded from this preliminary study that flying over a wavy surface would enhance the efficiency of a ground-effect craft and, hence, be rather beneficial.

The vorticity shed from the wing-tip is relatively strong and evolves into a region of concentrated vorticity known as the wing-tip vortex. The wing-tip vortices from a larger leading wing can influence the aerodynamic load on a trailing wing. The magnitude of this effect depends upon the distance between the two wings. When the mid-span of two wings are aligned, Y=0, the roll moment is zero. But as the mid-span of the smaller wing approaches the core of the trailing vortex of the larger wing, the roll moment increases. The value of roll moment is maximum when the mid-span of smaller wing has its closest distance with the core of the trailing vortex of the larger wing.

Bibliography

[1] Ando, S., Sakai, T., and Nitta, K., "Analysis of Motion of Airfoil Flying over Wavy-Wall Surface," Japan Soc. Aero and Space Science Vol. 35, No. 107, may 1992, pp. 27-38.

[2] Asfar, K. R., Mook, D. T., and Nayfeh, A. H., "Application of the Vortex-Lattice Technique to Arbitrary Bodies," Journal of Aircraft Vol. 16, No.7, 1979, pp. 420-424.

[3] Atta, E. H., Kandil, O. A., Mook, D. T., and Nayfeh, A. H., "Unsteady Aerodynamic Loads on Arbitrary Wings Including Wing-Tip and Leading-Edge separation," AIAA paper No. 77-156, LosAngeles, CA., January 1977.

[4] Atta, E. H., and Nayfeh, A.H., "Nonlinear Aerodynamics of Wing-Body combinations," AIAA paper 78-1206, Seattle, WA., July 1978.

[5] Belotserkovskii, S. M., "Study of the Unsteady Aerodynamics of Lifting Surfaces Using the Computer," Annual Review of Fluid Mechanics, Vol. 9, 1977, pp. 469-494.

[6] Belotserkovskii, S. M., 1965, "Thin Supporting Surface in a Subsonic Gas Flow," Moscow, Nauka 1965.

[7] Belotserkovskii, S. M., and Nisht, M. I., "Nonstationary Nonlinear Theory of a Thin Wing of Arbitrary Planform," Fluid Dynamics Vol. 9, No. 4, pp. 583-598, 1974.

[8] Bloy, A. W., and Trochalidias, V., "The Aerodynamic Interference Between Tanker and Receiver Aircraft During Air-to-Air Refuelling," Aeronautical Journal, Vol. 94, May 1990, pp. 165-171.

[9] Bloy, A. W., Trochalidias, V., and West, M. G., "The Aerodynamic Interference Between a Flapped Tanker Aircraft and a Receiver Aircraft During Air-to-Air Refuelling," Aeronautical Journal, Vol. 95, Oct. 1991, pp. 274-282.

[10] Bloy, A. W., West, M. G., Lea, K. A., and Jouma'a, M., "Lateral Aerodynamic Interference Between Tanker and Receiver Aircraft in Air-to-Air Refuelling," Journal of Aircraft, Vol. 30, No. 5, 1993, pp. 705-710.

[11] Chang, R. C., "An Experimental Investigation of Dynamic Ground Effect," Ph.D. Dissertation, Department of Aerospace Engineering, University of Kansas, Lawrence, KS., April, 1985.

[12] Chang, R. C., and Muirhead, V. U., "Investigation of Dynamic Ground Effect," NASA CP-2462, Proceedings of the 1985 NASA Ground Effects Workshop.

[13] Chen, Y. S., and Schweikhard, W. G., "Dynamic Ground Effects on a Two-Dimensional Flat Plate," Journal of Aircraft, Vol. 22, No.7, 1985, pp. 638-640.

[14] Dong, B., "Numerical Simulation of Two-Dimensional Lifting Flow," M.S. Thesis, Department of Engineering Science and Mechanics, Virginia Polytechnic Institute and State University, October, 1987.

[15] Elzebda, J. M., "Two-Degree-of-Freedom Subsonic Wing Rock and Nonlinear Aerodynamic Interference," Ph.D. Dissertation, Department of Engineering Science and Mechanics, Virginia Polytechnic Institute and State University, August, 1987.

[16] Elzebda, J. M., and Mook, D. T., and Nayfeh, A. H., 1994, "Numerical Simulation of Steady and Unsteady, Vorticity-Dominated Aerodynamic Interference," Journal of Aircraft, Vol. 31, No. 5, 1994, pp. 1031-1036.

[17] Faulkner, S., Hess, J. L. and Giesing, J. P., "Comparison of Experimental Pressure Distributions with Those Calculated by the Douglas Neuman Program," Douglas Aircraft Company, Rept. LB31831, Dec. 1964.

[18] Hoganson, E. H., "A Study of Aerodynamic Interference Effects During Aerial Refueling," M.S. Thesis, Air Force Institute of Technology, AD-A136895, Wright-Patterson AFB, OH, 1983.

[19] Iversen, J. D., and Bernstein, S., "Trailing Vortex Effects on Following Aircraft," Journal of Aircraft, Vol. 11, 1974 pp. 60-61.

[20] Kandil, O. A., "Prediction of the Steady Aerodynamic Loads on Lifting Surface Having Sharp-Edges Separation," Ph.D. Dissertation, Department of Engineering Science and Mechanics, Virginia Polytechnic Institute and State University, December, 1974.

[21] Kandil, O. A., Mook, D. T., and Nayfeh, A. H., "Nonlinear Prediction of Aerodynamic Loads on Lifting Surfaces," Journal of Aircraft, Vol. 13, No. 1, 1976, pp. 22-28.

[22] Karamcheti, K., "Principles of Ideal-Fluid Aerodynamics," Robert E. Krieger Publishing Company, Inc., Malabor, FL., 1980.

[23] Katz, J., and Maskew, B., "Unsteady Low-Speed Aerodynamic Model for Complete Aircraft Configurations," Journal of Aircraft, Vol. 25, No.4, 1988, pp. 302-310.

[24] Katz, J., and Weihs, D., "Wake Rollup and Kutta Condition for Airfoil Oscillating at High Frequency," AIAA Journal, Vol. 19, No. 12, Dec. 1981, pp. 1604-1606.

[25] Katz, J., "Calculation of the Aerodynamic Forces on Automotive Lifting Surfaces," Journal of Fluids Engineering, Vol. 107, Dec. 1985, pp. 438-443.

[26] Katz, J., and Weihs, D., "Behavior of Vortex Wakes from Oscillating Airfoils," Journal of Aircraft, Vol. 15, No. 12, Dec. 1978, pp. 861-863.

[27] Konstadinopoulos, P., Mook, D. T., and Nayfeh, A. H., "Numerical Method for General Unsteady Aerodynamics," AIAA Paper Number 81-1877, AIAA Atmospheric Flight Mechanics Conference, August 1981.

[28] Konstadinopoulos, P., Thrasher, D. F., Mook, D. T., Nayfeh, A. H., and Watson, L., "A Vortex-Lattice Method for General Unsteady Aerodynamics, "Journal of Aircraft, Vol. 22, No. 1, 1985, pp. 43-49.

[29] Konstadinopoulos, P., Mook, D. T., and Nayfeh, A. H., "Subsonic Wing Rock of Slender Delta Wing," Journal of Aircraft, March, 1985, Vol. 22.

[30] Licher, R. M., "Increases in Lift for Two and Three-Dimensional Wings Near the Ground," Douglas Aircraft, Santa Monica Division, Report No. SM-22615, Oct. 1956.

[31] Luton, J. A., and Mook, D. T., 1993, "Numerical Simulation of Flutter and its Suppression by Active Control," Vol. 31, No. 12, pp. 2312-2319.

[32] Maddox, S. A., "An Extension of a Vortex-Lattice Method to Include the Effects of Leading edge separation," M.S. Thesis, Department of Engineering Science and Mechanics, Virginia Polytechnic Institute and State University, 1973.

[33] McCroskey, W. J., McAlister, K. W., Carr, L. W., Pucci, S. L., Lambert, O., and Indergrand, R. F., "Dynamic Stall on Advanced Airfoil Sections," Journal of the American Helicopter Society, July 1981, pp. 40-50.

[34] Miley, S. J., "A Catalog of Low Reynolds Number Airfoil Data for Wind Turbine Application," Department of Aerospace Engineering, Texas A&M University, College Station TX., February, 1982.

[35] Mook, D. T. and Maddox, S. A., "Extension of a Vortex-Lattice Method to Include the Effects of Leading edge separation," Journal of Aircraft, Vol. 11, No. 2, 1974, pp. 127-128.

[36] Mook, D. T., and Dong, B., "Perspective: Numerical Simulations of Wakes and Blades-Vortex Interaction," Journal of Fluids Engineering, Vol. 116, 1994, pp. 5-21.

[37] Mracek, C. P., and Mook, D. T., "Aerodynamic Potential Flow Panel Method Coupled with Dynamics and Controls," AIAA Paper No. 91-2846, AIAA Atmospheric Flight Mechanics Conference, New Orleans, LA., August 1991.

[38] Nuhait, A. O., and Mook, D. T., "Numerical Simulation of Wings in Steady and Unsteady Ground Effects," Journal of Aircraft, Vol. 26, No. 12, 1989, pp. 1081-1089.

[39] Nuhait, A. O., and Zedan, M. F., "Numerical Simulation of Unsteady Flow Induced by a Flat Plate Moving Near Ground," Journal of Aircraft, Vol. 30, No. 5, 1993, pp. 611-617.

[40] Ogawa, A., "Vortex Flow," CRC Press 1993.

[41] Olwi, I., and Ghazi, M., "Effect of Wing Tip Vortices on a Trailing Aircraft," AIAA Journal, Vol. 30, No. 9, 1992, pp. 2186-2187.

[42] Plotkin, A., Kennell, C. G., "Thickness-Induced Lift on a Thin Airfoil in Ground Effect," AIAA Journal, Vol. 19, No. 11, 1981, pp. 1484-1486.

[43] Raghunathan, S., and Tan, C. P., "Performance of the Wells Turbine at Starting," Journal of Energy, Vol. 6, 1982, pp. 430-431.

[44] Raghunathan, S., and Tan, C. P., "The Aerodynamics of Wells Turbine," *Journal of Energy*, Vol. 7, 1983, pp. 226-230.

[45] Raghunathan, S., Harrison, J. R., and Hawkins, B. D., "Thick Airfoil at Low Reynolds Number and High Incidence," Journal of Aircraft, Vol. 25, No. 7, 1988, pp. 669-671.

[46] Richason, T. F., and Katz, J., "Unsteady Panel Method for Flows with Multiple Bodies Moving Along Various Paths," AIAA Journal, vol. 32, Jan. 1994, pp. 62-68.

[47] Steven, V. C., "The Ground Effect of a Power-Lift STOL Aircraft During Landing Approach," NASA CP-2462, Proceedings of the 1985 NASA Ground Effect Workshop.

[48] Thrasher, D. F., "Numerical Unsteady Aerodynamics with Application to Dynamic-Aerodynamic Interaction," M.S. Thesis, Department of Engineering Science and Mechanics, Virginia Polytechnic Institute and State University, 1979.

[49] Thrasher, D. F., Mook, D. T., Kandil, O., and Nayfeh, A. H., "Application of the Vortex-Lattice Concept to General, Unsteady Lifting-Surface Problems," AIAA Paper No., 77-1157, 1977.

[50] Tuck, E. O., "Hydrodynamic Problems of Ships in Restricted Waters," Annual Review of Fluid Mechanics, Vol. 10, 1978, pp. 33-44.

VITA

Reza Karkehabadi was born in Semnan, Iran on the 8th of January 1961. He completed his high school education at Kharazmi High School in Tehran. In 1978, he came to the U.S.A to further pursue his education. He received his B.S. from the University of the District of Columbia in Mechanical Engineering. He received his M.S. from Howard University. In the fall of 1989, he began his graduate study at Virginia Polytechnic Institute and State University for the degree of Ph.D. in Engineering Science and Mechanics.